

Infrared Spectroscopic Studies on pristine and doped Bismuth Ferrite Ceramics

By

Bijay Kumar Das

Enrolment No: PHYS 02 2015 04 008

Indira Gandhi Centre for Atomic Research, Kalpakkam

A thesis submitted to the

Board of Studies in Physical Sciences

*In partial fulfillment of requirements
for the Degree of*

DOCTOR OF PHILOSOPHY

of

HOMI BHABHA NATIONAL INSTITUTE

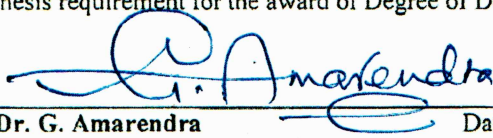



November, 2020

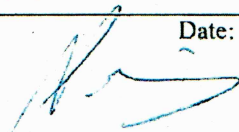
Homi Bhabha National Institute

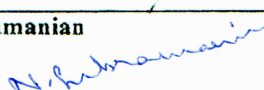
Recommendations of the Viva Voce Committee


As members of the Viva Voce Committee, we certify that we have read the dissertation prepared by Bijay Kumar Das entitled "Infrared Spectroscopic Studies on pristine and doped Bismuth Ferrite Ceramics" and recommend that it may be accepted as fulfilling the thesis requirement for the award of Degree of Doctor of Philosophy.


Chairman: Dr. G. Amarendra Date: April 7, 2021

Guide/ Convener: Dr. T. N. Sairam Date: 07/04/2021


External Examiner: Dr. Alain Polian Date: 7/4/2021



Member 1: Dr. N. Subramanian Date: 07/04/2021


Member 2: Dr. Arup Dasgupta Date: 07/04/2021


Final approval and acceptance of this thesis is contingent upon the candidate's submission of the final copies of the thesis to HBNI.

I hereby certify that, I have read this thesis prepared under my direction and recommend that it may be accepted as fulfilling the thesis requirement.

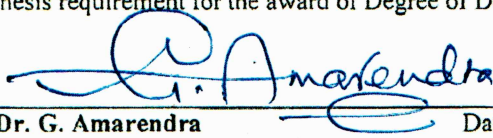
Date: 07/04/2021
Place: KALPAKKAM



Dr. T. N. Sairam
(Guide)

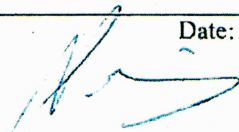
Homi Bhabha National Institute

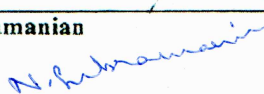
Recommendations of the Viva Voce Committee


As members of the Viva Voce Committee, we certify that we have read the dissertation prepared by Bijay Kumar Das entitled "Infrared Spectroscopic Studies on pristine and doped Bismuth Ferrite Ceramics" and recommend that it may be accepted as fulfilling the thesis requirement for the award of Degree of Doctor of Philosophy.


Chairman: Dr. G. Amarendra Date: April 7, 2021

Guide/ Convener: Dr. T. N. Sairam Date: 07/04/2021


External Examiner: Dr. Alain Polian Date: 7/4/2021



Member 1: Dr. N. Subramanian Date: 07/04/2021


Member 2: Dr. Arup Dasgupta Date: 07/04/2021


Final approval and acceptance of this thesis is contingent upon the candidate's submission of the final copies of the thesis to HBNI.

I hereby certify that, I have read this thesis prepared under my direction and recommend that it may be accepted as fulfilling the thesis requirement.

Date: 07/04/2021
Place: KALPAKKAM


Dr. T. N. Sairam
(Guide)

Statement by Author

This dissertation has been submitted in partial fulfillment of requirements for an advanced degree at Homi Bhabha National Institute (HBNI) and is deposited in the Library to be made available to borrowers under rules of the HBNI.

Brief quotations from this dissertation are allowable without special permission, provided that accurate acknowledgement of source is made. Requests for permission for extended quotation from or reproduction of this manuscript in whole or in part may be granted by the Competent Authority of HBNI when in his or her judgment the proposed use of the material is in the interests of scholarship. In all other instances, however, permission must be obtained from the author.

Bijay Ku. Das
Bijay Kumar Das

Declaration

I, hereby declare that the investigation presented in the thesis has been carried out by me. The work is original and has not been submitted earlier as a whole or in part for a degree / diploma at this or any other Institution / University.

Bijay Ku. Das
Bijay Kumar Das

List of Publications

a) Journal publication

1. Emergence of two-magnon modes below spin-reorientation transition and phonon-magnon coupling in bulk BiFeO₃: An infrared spectroscopic study, **B. K. Das**, B. Ramachandran, A. Dixit, M. S. R. Rao, R. Naik, A. T. Sathyanarayana, T. N. Sairam and G. Amarendra *J. Alloys Compd.* 2020 **832** 154754
2. Single-ion anisotropy driven splitting of spin wave resonances in BiFeO₃ at low temperature, **B. K. Das**, T. N. Sairam, B. Ramachandran and M. S. R Rao *J. Phys. Condens. Matter* 2020 **32** 405701
3. Chemical pressure induced near-complete suppression of spin-wave excitations in Bi_{0.9}A_{0.1}FeO_{2.95} (A = Ba, Ca), **B. K. Das**, T. N. Sairam, B. Ramachandran and M. S. R Rao *J. Phys. D: Appl. Phys* 2020 **53** 495302

b) Communicated/Under preparation

1. Low-temperature investigation of BiFeO₃ through EPR spectroscopy, **B. K. Das**, T. N. Sairam, B. Ramachandran and M. S. R Rao (Under preparation)
2. Investigation of ferroelectric and magnetic properties of pristine and doped BiFeO₃ ceramics through PFM and MFM studies **B. K. Das**, G. Mangamma T. N. Sairam, B. Ramachandran and M. S. R Rao (Under preparation)

c) Conferences

1. Studies of SrMnGe₂O₆ by Infrared Spectroscopy, **B. K. Das**, T. N. Sairam International Conference on Technologically Advanced Materials & Asian Meeting on Ferroelectricity, 07-11 Nov 2016, University of Delhi

2. Studies of Magnetite by infrared spectroscopy, **B. K. Das**, T. N. Sairam
International Conference On Laser Deposition, IIT Madras , 20-22 Nov 2017
3. Soft mode behavior of magnetite film across relaxor ferroelectric transition,
B. K. Das, T. N. Sairam, R. Krishnan and G. Amarendra International
Conference on Perspectives in Vibrational Spectroscopy (ICOPVS-2018),
BARC-MUMBAI, 25 -29th Nov 2018
4. Study of Spin wave excitations in $\text{Bi}_{(1-x)}\text{A}_x\text{FeO}_3$ (A=Ba, Ca) ceramics by
Infrared Spectroscopy, **B. K. Das**, T. N. Sairam, B. Ramachandran, M. S.
Ramachandra Rao and G. Amarendra International Conference on
Perspectives in Vibrational Spectroscopy (ICOPVS-2018), BARC-
MUMBAI, 25 -29th Nov 2018
5. Far-infrared Study of Magnetite Thin Film across the Verway Transition, **B.**
K. Das, T. N. Sairam, R. Krishnan and G. Amarendra International
conference on magnetic materials and applications (ICMAGMA-2018),
NISER, Bhubaneswar 9-13th Dec 2018
6. Suppression of spin wave excitations in BiFeO_3 through aliovalent
substitution, **B. K. Das**, B. Ramachandran, M.S.R. Rao, G. Amarendra and
T. N. Sairam National Conference on Light Matter Interaction at Nanoscale
(LMIN-2019), IGCAR, 15-17th July 2019

**This Thesis is
Dedicated to my Family
& Teachers**

Acknowledgements

In this page, I recall the people behind the scene and their contributions towards the journey of this dissertation. Without their constant support, reaching the goal in finishing this dissertation would not have been possible.

First and foremost, I am grateful to my supervisor, Dr. T. N. Sairam, for his valuable guidance, constant encouragement and support throughout the course of the present dissertation. Apart from this, he also helped me a lot for my all-round development.

I am also very grateful to the distinguished faculty in my doctoral committee, Dr. G. Amarendra, Dr. N. Subramanian and Dr. Arup Dasgupta for sharing their valuable time, providing valuable comments and evaluating my work at each stage.

I want to express my gratitude to Dr. A. K. Bhaduri and Dr. S.A.V. Satya Murty, present and former Director, IGCAR, for permitting me to pursue Ph. D. at IGCAR. I am highly thankful to Dr. Shaju K. Albert and Dr. G. Amarendra, present and former Group Director, MSG, for providing a pleasant atmosphere for my smooth research. I thank the present Dean, Student Affairs Dr. Vidhya Sundararajan, and former Dean, Student Affairs Dr. T. S. Lakshmi Narasimhan and Dr. M. Saibaba for the wonderful hospitality during my stay at JRF Enclave. I would like to thank Dr. R. Rajaraman, Dr. N. V. Chandra Shekar and Dr. B. V. R. Tata, present and former Dean, Physical Sciences, HBNI, IGCAR for their support and being friendly during all the procedure throughout the tenure.

It is my pleasure to express my gratitude to Dr. G. Mangamma for her support towards the dissertation, encouragement and care throughout the tenure. I want to express my sincere thanks to Dr. B. Ramachandran for his suggestions and constructive reviews that helped me to improve a lot.

I want to extend my sincere thanks to Prof. M. S. R. Rao, Dr. A. T. Sathyanarayana, Dr. A. Dixit, Dr. R. Naik, Dr. R. Krishnan, Dr. Madhusmita Panda, Dr. S. Amirthapandian,

and Mr. P. Magudapathy for the collaboration, discussions and immense help at various stages of my Ph.D. career. I would like to thank Dr. R. Govindaraj and all the MPS members for their timely help and support. I would like to acknowledge the Dept. of Atomic Energy, Govt. of India for research fellowship. I acknowledge Dr. K. Gireesan and members of the cryogenic facility for providing liquid helium and liquid nitrogen for low-temperature measurements. I am also thankful to all the reviewers and the examiner for their time and careful evaluation.

I would like to thank my seniors, batch mates, friends, juniors, Dr. S. Subramanian, Dr. Subrata Ghosh, Mr. Shashwat Kumar Swain, Dr. Madhusmita Sahoo, Dr. Soumee Chakraborty, Dr. Santanu Parida, Dr. Raktima Basu, Dr. Padmalochan Panda, Dr. Nilakantha Meher, Dr. Alaka Panda, Dr. Arpita Aparajita, Shiti, Sradhanjali, Surajit, Twisha, Thiru, Vinod, Jegan, Pavan, Mady, Suma, Sumana, Gopi, Dillip, Alok, Sitakanta, Prashant, Anil, Suvendu, Binaya, Ijee, Pragyna, Akshaya, Rajitha, Jakatha, Parvathy, Ravi, Lata, Abinash, Rama, Dinesh, Suresh, Falguni, Silu, Biju, Ashok, Arabinda and all the research scholars of IGCAR for their suggestions, encouragement, friendship and help during these years. I wish to extend my sincere gratitude to all my teachers, who had taught me.

Finally, I am thankful to my beloved Father Mr. Umakanta Das, Mother Mrs. Shakuntala Das, and my family members Rina, Kuni, Aswini, Papu, Lipi, Chintu, Mamun and Mampi for their constant support, encouragement and unconditional love. I express gratitude to my wife Rinku who has just entered my life. Thank you all for your love, patience and help to make it possible.

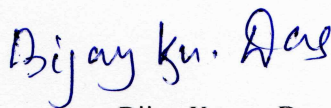

Bijay Kumar Das

Table of contents

List of Publications	v
Acknowledgements	ix
Abstract	xi
Table of contents	xiii
List of Figures	xvii
List of tables	xx
Symbols and acronyms used in the thesis	xxi

Chapter 1 Introduction 1

1.1. Multiferroicity	1
1.1.1. Ferroic ordering	1
1.2. Bismuth ferrite (BiFeO_3).....	3
1.2.1. Crystal structure.....	3
1.2.2. Ferroelectric ordering in BiFeO_3	5
1.2.3. Magnetic Structure of BiFeO_3	6
1.3. Phonons, magnons and electromagnons in Bismuth ferrite	10
1.4. Motivation.....	11
1.4.1. Magnetic property at low temperature and Phonon-magnon coupling effect in BiFeO_3	11
1.4.2. Influence of SIA and anharmonicity of spin cycloid on SWEs at low temperature	12
1.4.3. Doping effect on SWEs	13
1.5. Research objective and overview of the thesis	14

Chapter 2 Experimental techniques..... 19

2.1. Samples' history.....	19
2.1.1. Pristine BiFeO_3 sample.....	19
2.1.2. Doped BiFeO_3 ceramic samples	20
2.2. Fourier-transform infrared (FTIR) spectrometer	21
2.2.1. Basic principles and instrumentation of FTIR.....	21
2.2.2. Fourier-Transformation	23
2.2.3. Apodization function	24
2.2.4. Resolution.....	24
2.2.5. Bruker Vertex 80v FTIR spectrometer.....	24
2.3. Raman Spectroscopy.....	26
2.3.1. Instrumentation.....	26
2.4. SQUID-VSM magnetometer	28
2.5. EPR spectroscopy	28
2.5.1. EPR spectrometer	29

2.6. Atomic force microscopy (AFM)	29
2.7. Piezoelectric force microscopy (PFM)	30
2.8. MFM	30
Chapter 3 Investigations of phonon behavior across spin reorientation transitions in BiFeO₃	33
3.1. INTRODUCTION	33
3.2. Experimental methods	34
3.3. Results and discussions.....	36
3.3.1. Magnetic Studies	36
3.3.2. Infrared studies	40
3.4. Conclusions.....	49
Chapter 4 Investigation of spin-wave excitations in BiFeO₃ at low-temperature	51
4.1. Introduction.....	51
4.2. Experimental.....	52
4.3. Results and discussion	54
4.3.1. Infrared study	54
4.3.1.1. Low temperature changes in SW mode frequency	55
4.3.1.2. Low temperature changes in SW Mode Intensity	60
4.3.1.3. Intensity changes below 250K.....	61
4.3.2. EPR measurements.....	63
4.4. Conclusion	69
Chapter 5 Suppression of spin wave excitations in BiFeO₃ through aliovalent substitution.....	71
5.1. Introduction.....	71
5.2. Experimental.....	72
5.3. Results and discussions.....	74
5.3.1. Phonon Contribution	75
5.3.2. Magnon contribution	79
5.3.2.1. Infrared measurements.....	79
5.3.2.2. Raman measurements	82
5.4. Conclusion	85
Chapter 6 Ferroelectric and magnetic properties of pristine and doped BiFeO₃ through PFM and MFM measurements	87
6.1. Introduction.....	87
6.2. Experimental.....	88
6.3. Results and discussion	89

6.3.1. PFM studies on pristine BiFeO ₃ ceramic pellet.....	89
6.3.1.1. Piezoresponse force spectroscopy	92
6.3.1.2. Calculation of piezoelectric coefficient (d_{33}).....	93
6.3.2. PFM studies on 10% Ba doped BiFeO ₃ ceramic pellet	95
6.3.2.1. Piezoresponse force spectroscopy	97
6.3.3. PFM studies on 5 % Ba and 5 % Ca co-doped BiFeO ₃ ceramic pellet	98
6.3.3.1. Piezoresponse force spectroscopy	99
6.3.4. PFM studies on 10 % Ca-doped BiFeO ₃ ceramic pellet.....	100
6.3.4.1. Piezoresponse force spectroscopy	101
6.3.5. MFM studies.....	102
6.4. Conclusion	104
Chapter 7 Summary and future directions	105
7.1. Summary	105
7.1.1. Chapter 3	105
7.1.2. Chapter 4	106
7.1.3. Chapter 5	106
7.1.4. Chapter 6	107
7.2. Future directions	107
<i>References</i>	<i>109</i>

List of Figures

Figure 1.1	Field versus response curve (Hysteresis loop of ferroic ordering).	2
Figure 1.2	a) Pseudocubic and b) rhombohedral unit cell representation of BiFeO ₃ .	4
Figure 1.3	Hexagonal unit cell representation of BiFeO ₃ .	4
Figure 1.4	Super-exchange interaction between NN and NNN spins of Fe ion mediated via oxygen atoms.	7
Figure 1.5	The magnetic structure of a portion of BiFeO ₃ lattice is shown in hexagonal unit cell representation, where the spins of Fe are shown. The direction of spin cycloid is shown by the arrow pointed along $\langle 110 \rangle_{\text{hex}} \equiv \langle 101 \rangle_{\text{pc}}$.	8
Figure 1.6	Schematic of spin cycloid in BiFeO ₃ .	9
Figure 2.1	Schematic of FTIR spectrometer. The cosine functions (a) and (b) are the Fourier transform of their corresponding monochromatic light of frequency ν_1 and ν_2 , respectively. The beat pattern (c) of two monochromatic light sources of frequencies ν_1 and ν_2 . (d) Interferogram of a broad band light source.	22
Figure 2.2	Optical lay-out of Bruker Vertex 80v FTIR spectrometer.	25
Figure 2.3	A photograph of Bruker Vertex 80v FTIR spectrometer setup	25
Figure 2.4	Quantum Mechanical description of Raman spectroscopy.	26
Figure 2.5	Schematic of a Raman spectrometer.	27
Figure 2.6	Schematic of a SQUID-VSM magnetometer.	28
Figure 2.7	Schematic of an EPR spectrometer.	29
Figure 2.8	PFM cantilever deflection versus applied voltage.	30
Figure 3.1	Zero-field cooled and field cooled magnetization curves of BiFeO ₃ at a magnetic field of (a) 0.01 T, (b) 0.1 T and (c) 1 T. The insets in b) and c) represent the semi-log plot of zero field cooled and field cooled magnetization curves.	37
Figure 3.2	$H^{4/7}$ versus T_{irr} plot of BiFeO ₃ sample. The fitted straight line (red color) to the magnetic data points is the AT-line. The $M \sim H$ loops at 300 and 100 K are shown in the inset shown in the upper right corner of the figure. The temperature evolution of coercivity is shown in the inset at the lower left corner of the figure.	39
Figure 3.3	Reflectance spectra of BiFeO ₃ at a few selected temperatures.	40
Figure 3.4	Reflectance spectra of BiFeO ₃ at 300 and 100 K. Red solid lines are the spectral fits.	41
Figure 3.5	Temperature evolution of frequency and linewidth of E(TO1) mode. The red curve is the fit to cubic anharmonic model. The arrow at ~ 20 K points to the dielectric anomaly.	43

Figure 3.6	Mode frequency of (a) E(TO7) and (b) E(TO8) with respect to temperature. The solid curves show the anharmonic fit to the data.	44
Figure 3.7	Temperature evolution of (a) E(TO2), (b) A_1 (TO1), (c) E(TO4), (d) E(TO9) and (e) A_1 (TO4) mode frequencies.	45
Figure 3.8	Temperature evolution of frequencies of (a) A_1 (TO2), (b) E(TO3), (c) E(TO5), (d) A_1 (TO2) and (e) E(TO6) modes.	46
Figure 3.9	(a) Reflectance and (b) the corresponding extinction coefficient spectra of BiFeO_3 at a few selected temperatures.	47
Figure 3.10	Temperature evolution of the lineshape parameters of the new 111 cm^{-1} two-magnon mode.	48
Figure 4.1	(a) Reflectance and (b) the corresponding extinction coefficient spectra of BiFeO_3 at a few selected temperatures. The insets show the SWEs on expanded scale.	55
Figure 4.2	(a) Extinction coefficient spectra of BiFeO_3 at 290 K and (b) cyclon and extracyclon energy fits to the obtained mode frequencies of cyclons and extracyclons, respectively.	56
Figure 4.3	The extinction coefficient spectra of BiFeO_3 at a few selected temperatures.	57
Figure 4.4	SW mode frequencies as a function of temperature.	58
Figure 4.5	Normalized integrated intensity of (a) $\Phi_2^{(1,2)}$, (b) $\Phi_3^{(1,2)}$, (c) $\Phi_4^{(1,2)}$, (d) $\Psi_2^{(1,2)}$, (e) $\Psi_3^{(1,2)}$ and (f) $\Psi_4^{(1,2)}$ as a function of temperature.	59
Figure 4.6	EPR spectra of BiFeO_3 at a few selected temperatures.	63
Figure 4.7	Asymmetry parameter and peak area under the EPR signal in BiFeO_3 .	64
Figure 4.8	EPR spectra curve-fitted with two Gaussian components at (a) 300, (b) 200, (c) 160 and (d) 80 K.	65
Figure 4.9.	Low temperature plot of lineshape parameters of the paramagnetic component (The solid lines are guide-to-the-eye).	66
Figure 4.10.	Low temperature plot of the lineshape parameters of the ferromagnetic component (The solid lines are guide-to-the-eye).	66
Figure 4.11.	Temperature variation of $\Delta g/g$ corresponding to the ferromagnetic component.	68
Figure 5.1	Infrared reflectance measurements of pristine and doped BiFeO_3 samples. The box in the low-frequency region shows SWEs which have been shown on an expanded scale in the inset.	75
Figure 5.2	Reflectance spectra of (a) BFO, (b) BBFO, (c) BBCFO and (d) BCFO.	76
Figure 5.3	Plots of (a) percentage relative shift and (b) linewidth versus reduced unit cell volume.	79
Figure 5.4	k-spectra of (a) BFO, (b) BBFO, (c) BBCFO and (d) BCFO fitted with Gaussian line shapes.	80

Figure 5.5	A plot of spectral weight of the samples with reduced unit cell volume	81
Figure 5.6	Low-frequency Raman measurements.	83
Figure 5.7	Fitted low-frequency Raman spectra of (a) BFO, (b) BBFO, (c) BBCFO and (d) BCFO with Gaussian line shapes.	83
Figure 5.8	(a) Index plot of SWE mode frequencies obtained from infrared and Raman measurements for pristine sample, which are fitted with cyclon and extracyclon energies. (b) A plot of integrated intensity, I , of SWEs with reduced unit cell volume.	84
Figure 6.1	Topography, mag and phase images of BFO sample at a few selected dc voltages. The yellow and white dotted loops are the regions of magnetic domains which show noticeable changes with applied dc voltage.	90
Figure 6.2	Schematic of 71° , 109° and 180° domain switching in rhombohedral BiFeO_3 .	91
Figure 6.3	Phase and mag loops of pristine BFO sample.	93
Figure 6.4	Topography, mag and phase images of BBFO at a few selected dc voltages. The yellow and white dotted loops are the regions of magnetic domains which show noticeable changes with applied dc voltage.	96
Figure 6.5	Phase and mag loops of Ba-doped BFO sample.	97
Figure 6.6	Topography, mag and phase images of BBCFO at few selected dc voltages. Yellow colored loops point to the region of piezo-domains showing polarization switching between +5 V and -5 V.	98
Figure 6.7	Phase and mag loops of Ba-Ca co-doped BFO sample.	99
Figure 6.8	Topography, mag and phase images of BCFO at a few selected dc voltages. Yellow colored loops point to the region of piezo-domains showing polarization switching between +5 V and -5 V.	100
Figure 6.9	Phase and mag loops of Ca-doped BFO sample.	101
Figure 6.10	MFM image a commercial hard disk.	102
Figure 6.11	(a) MFM image and (b) the corresponding line profile of phase and height BFO sample at $y=35\text{ }\mu\text{m}$. (c) MFM image and (d) the corresponding line profile of phase and height BCFO sample at $y=32\text{ }\mu\text{m}$ (e) Expanded region of figure 6.11c showing bright and dark fringes.	103

List of tables

Table 1.1	Classification of ferroic orderings.	3
Table 2.1	Unit cell parameters of pristine and doped BiFeO ₃ ceramic samples	20
Table 3.1	The obtained mode parameters of bulk BiFeO ₃ using the four- parameter model as described in Equations (3.1) and (3.2).	42
Table 4.1	Normalized Spectral weight distribution of SW modes across the magnetic transition at 250 K.	61
Table 5.1	The estimated values of reduced unit cell volume ($\Delta V/V$), bond length (\AA), bond angle ($^\circ$), remnant magnetization (M_r) and coercivity (H_c) [97].	73
Table 5.2	The obtained values of reduced unit cell volume ($\Delta V/V$), phonon frequency (ω), and damping constant (γ) of the BiFeO ₃ -based samples.	77
Table 5.3	The SWE mode frequencies for pristine and doped BFO sample.	80
Table 6.1	Comparison of the reported d_{33} value of BiFeO ₃ with the present work	94

Chapter 7

Summary and future directions

In this thesis, vibrational, magnetic and ferroelectric properties of BiFeO_3 are extensively investigated at low temperature as well as with respect to doping. The low temperature phonon behavior suggests that the phonon-magnon coupling effect exists in BiFeO_3 , which is evident from the anomalous behavior of the phonon modes across spin reorientation transition. The improved magnetic property (weak ferromagnetic behavior) at low temperature and through Ca-doping is reflected as the near-complete suppression of spin-wave excitations (SWEs) in the infrared reflectance spectra. A complete removal of degeneracy of SWEs is observed for the first time in (i) pristine BiFeO_3 across the SRT at 250 K and (ii) at room temperature in Ca-doped samples, which is understood through increase in single ion anisotropy at low temperatures and in Ca-doped samples, respectively. On the other hand, the ferroelectric property reduces substantially through doping of Ca in BiFeO_3 lattice.

7.1. Summary

The major findings of the thesis are listed as follows:

7.1.1. Chapter 3

- The magnetic measurements on BiFeO_3 show improved magnetic property and two SRTs (150 and 257 K) at low temperature. The critical exponent derived from AT-line is found to be 1.75 which shows that BiFeO_3 behaves as a mean field system
- All the thirteen theoretically expected phonon modes of BiFeO_3 , allowed by the rhombohedral symmetry are observed in the infrared reflectivity measurements. The low energy E(TO1) mode shows anomalous behavior across the SRTs, which gives evidence of phonon-magnon coupling effect in multiferroic BiFeO_3 .

- A new two-magnon mode at 111 cm^{-1} is noticed to emerge below 160 K which is possibly due to modifications in the non-collinear spin structure brought about by spin reorientation transition. This mode is also sensitive to a dielectric anomaly seen at 25 K and is thus suggested to be an electromagnon which is a quasi-particle of the multiferroic material.

7.1.2. Chapter 4

- All the observed SW modes in the infrared spectra of the pristine BiFeO_3 ceramic samples have been successfully assigned to cyclon and extra-cyclon modes.
- A complete removal of degeneracy of these SW modes is seen at 250 K. The cause of the lifting of the degeneracy is due to an increase in SIA brought about by spin reorientation transition.
- The anomalies seen in the variation of normalized intensity of SWEs near 250 and 150 K are related to the spin reorientation transitions. The partial suppression of SW modes at low temperature is because of increase in SIA and anharmonicity of spin cycloid. This points to an improvement in magnetic and magnetoelectric property of BiFeO_3 at low temperature.
- EPR studies on pristine BiFeO_3 give clear evidence of SRTs as well as insight in to the magnetic and magnetoelectric properties of BiFeO_3 . The sharp increase in degree of spin canting below 130 K is well correlated with improved magnetic and magnetoelectric properties at low temperatures.

7.1.3. Chapter 5

- The thirteen infrared modes of BiFeO_3 are observed in all the doped samples as well. Here, doping induced chemical pressure plays a vital role in BiFeO_3 lattice which is evident from the correlated changes observed in the phonon behavior with respect to reduced unit cell volume.

- The observed SWE modes in the doped BiFeO₃ samples have been assigned with the corresponding cyclon and extracyclon modes. A complete removal of degeneracy of the SW modes is seen in Ca and Ba-Ca co-doped samples, which is due to increase in SIA brought about by Ca-doping.
- A near-complete suppression of the SWEs is noticed in the case of Ca and co-doped samples, which is because of the destruction of the spin cycloid effected through doping induced increase in both SIA and anharmonicity of the cycloid.
- The Ca and co-doped samples have shown better magnetic and magnetoelectric property compared to pristine and Ba-doped BiFeO₃.

7.1.4. Chapter 6

- PFM studies on BFO-based samples have been carried out to understand their ferroelectric behavior. Piezo-domains in the phase and mag images are observed in all the studied samples, which show piezoelectric behavior.
- Observation of symmetrical ferroelectric (mag and phase) loops confirm the ferroelectric property in all the studied samples. Loop saturation suggests that our samples have minimum leakage current.
- The d_{33} value of the pristine BiFeO₃ is deduced to be about 70-80 pm/V, which is close to the theoretical value. This suggests the high quality of the samples used in our studies.
- The d_{33} value of BBFO is found to be close to the d_{33} value of the pristine sample whereas Ca-doped samples are found to have the least d_{33} value of 15-20 pm/V.

7.2. Future directions

- The splitting of SWE modes in BiFeO₃ has been seen for the first time at low temperature in our studies. This has opened up an opportunity for an in-depth

theoretical understanding of this system. Further theoretical work in this direction, therefore, is highly desirable.

- Having seen SIA dependent splitting of SW modes at low temperature in BiFeO₃, it would be interesting to look for this effect in other similar magnetic oxides.
- The two-magnon mode observed at 112 cm⁻¹ below 150 K in pristine BiFeO₃ has been suggested to be an electromagnon from our present study. Further magnetic-field dependent IR studies can confirm this aspect.
- Our low temperature infrared study on pristine BiFeO₃ gives evidence of a dielectric anomaly at ~ 20 K that is attributed to relaxor ferroelectric behavior. Similar investigations in doped BFO samples to find out whether such relaxor ferroelectric behavior exists can be taken up. Additionally, the temperature evolution of SWE modes in the doped samples can also be followed to study the effect of doping on SIA in these systems.
- Apart from obtaining information about piezoelectric response, PFM technique has also been found to play an important role in exploring the magnetoelectric coupling strength in multiferroics. Such experiments on BFO-based samples will be much useful.
- Temperature dependent EPR studies on the doped BFO samples will be of use in understanding doping-induced spin dynamics in these systems.

Abstract

In this thesis, behavior of the vibrational and spin wave excitation spectra of bismuth ferrite, a room temperature multiferroic, is studied in detail both at low temperature and as a function of aliovalent doping using infrared spectroscopy.

Multiferroics are materials that exhibit simultaneous presence of two or more ferroic orders such as e.g., ferroelectricity, ferromagnetism, etc. Among all the known multiferroics, bismuth ferrite attracts special attention because of its room temperature multiferroicity. Because of this uniqueness, it is also one of the widely studied. It has a rhombohedrally distorted perovskite structure with $R3c$ space group. It exhibits G-type antiferromagnetism and a spiral spin arrangement. Apart from exhibiting multiferroicity, bismuth ferrite is also known to undergo spin-reorientation transitions (SRTs) at low temperature, although there exists no unique consensus on this in the literature.

While many infrared and Raman studies have been reported so far, there are not any studies whereby both the phonon and spin wave behavior at low temperature are investigated vis-à-vis the SRTs. In this respect, we have taken bismuth ferrite ceramic samples prepared by sol gel route and first established the SRTs using SQUID-VSM magnetic measurements. Two spin-reorientation transitions could be unequivocally identified, one at 257 K and another at 150 K. The detailed analysis of the magnetic data also proved that the system exhibits a mean-field type of behavior rather than spin-glass type, as suggested by some researchers. Room temperature infrared reflectance spectrum of the ceramic sample showed all the thirteen modes expected from group theoretic arguments for the rhombohedral symmetry of the $R3c$ space group of bismuth ferrite. In addition, the very far-IR part of the spectrum showed clear resonance like features attributed to the spin wave excitations (SWEs) occurring as a result of the interaction of the long wavelength radiation with the magnon modes. Low temperature infrared reflectance data collected over

the far and the mid-infrared range using a broadband vacuum FTIR spectrometer were analyzed by fitting four-parameter model. Almost all the phonon modes clearly showed anomalous behavior across the SRTs in their mode frequency variation. Interestingly, two new magnon modes emerge below 150 K (one at 106 and another at 111 cm^{-1}).

This new observation became the basis for a detailed study of the SWEs in BiFeO_3 at low temperature. The SWEs observed in BiFeO_3 at room temperature are all doubly degenerate according to the current theoretical understanding. In our study, we found the surprising result of the SWEs undergoing a splitting near the SRT at 250 K. Such a behavior in this sample has not been reported to date. In addition, we have shown that the SWEs get partially suppressed due to increase in single ion anisotropy as well as anharmonicity in the spin cycloid in this material.

One of the aims of this thesis is to achieve suppression of the spin-cycloid in BiFeO_3 at room temperature to pave way for enhanced magnetic properties by aliovalent doping. To this end, we have made infrared reflectance and low frequency Raman measurements on Ba, Ca and Ba-Ca co-doped samples to monitor the behavior of the SWE spectrum. Interestingly, we found that Ca-doped BiFeO_3 sample showed almost a complete suppression of the SWEs.

To gain further understanding of the observed behavior of the doped samples, we have looked at these samples through piezoresponse force microscopy (PFM) and Magnetic force microscopy (MFM). Using the phase and mag images from the PFM data, it is found that Ba-doped sample retains ferroelectricity, while the Ca-doped sample shows weakened ferroelectric properties. In contrast, MFM studies revealed enhanced magnetism for the Ca-doped sample as compared to the pristine sample. These results corroborate the conclusions from our IR studies.

Chapter 1

Introduction

This chapter gives a brief introduction to multiferroicity & multiferroic material BiFeO_3 followed by motivation & overview of the thesis. In this thesis, we have addressed fundamental aspects of multiferroic material BiFeO_3 i.e., to understand improved magnetic and magnetoelectric property at low temperature as well as via doping at room temperature through infrared spectroscopic technique, which are in accordance with the results obtained from magnetic measurements, Raman scattering studies, electron paramagnetic resonance experiments, and Piezo and magnetic force microscopy investigations.

1.1. Multiferroicity

Multiferroicity [1-16] is the intrinsic property of any material that exhibits coexistence of more than one type of ferroic order such as ferroelectric, ferromagnetic and ferroelastic, and their cross-coupling. For instance, in the case of magnetoelectric multiferroic, there is a simultaneous existence of electric and magnetic ordering as well as a cross coupling between these two orders. Thus electric polarization in the material can be tuned via applying a magnetic field and vice versa [1-3, 9-12]. As a result, these materials act as potential candidates for practical applications such as designing multiple states of memory devices, etc. [11]. Therefore magnetoelectric multiferroic materials have gained enormous attention based on their intrinsic and functional property in recent years. As ferroic ordering is central to multiferroicity, some of the ferroic properties are briefly introduced in the next section.

1.1.1. Ferroic ordering

The importance of ferroic ordering comes from the presence of its spontaneous polarization (response) and its switchable property with respect to an applied field. This property is characterized by field versus response curve, which is known as the hysteresis

loop of the ferroic ordering, as shown in Figure 1.1. If a ferroic material is never polarized or completely depolarized, then it will follow the dashed line (see Figure 1.1) as the field is increased. Here, the value of polarization (ξ) is initially zero, then starts rising with the application of an increasing applied field (F) and finally saturates for high values of F . This behavior of the response curve is because of the fact that the randomly oriented ferroic domains start aligning with increasing F and get fully aligned for high values of F giving rise to saturation in polarization. Even F is reduced back to zero, polarization continues to have a finite value, which is known as retentivity, as shown in the Figure 1.1. This ξ_r is referred to as the level of residual or remnant polarization in the material. At this point, even though the polarizing field is zero, still some of the ferroic domains remain aligned with respect to field, while others lose their alignment.

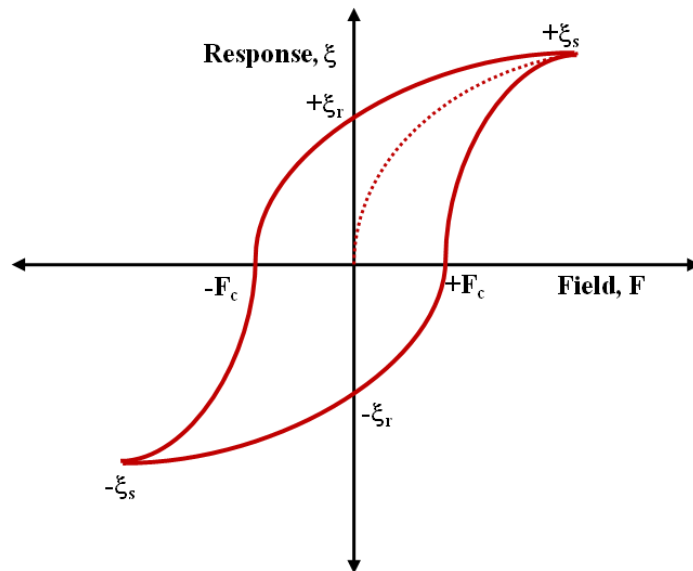


Figure 1.1 Field versus response curve (Hysteresis loop of ferroic ordering).

If F is increased in the reverse direction, value of ξ decreases and reaches zero as shown in the Figure 1.1. This is because of the fact that the reverse field starts flipping the ferroic domain in opposite direction. Here, the field required to remove the residual polarization completely is called coercive field (F_c). Further increase in the field in the

reverse direction starts polarizing the material in the opposite direction and finally results in saturation for high values of reverse field. If, now, the reverse field is reduced to zero, the material continues to possess residual polarization ($-\xi_r$) in the opposite direction. This $-\xi_r$ can be nullified by applying $+F_c$. Notably, the curve will never return to origin as coercive field is needed to depolarize the material. Thus, the polarization versus field curve forms a characteristic loop called ‘hysteresis loop’ of the ferroic ordering.

Different types of ferroic ordering are ferroelectric, ferromagnetic and ferroelastic ordering. The polarizing field and its corresponding response for each type of ferroic order are listed in Table 1.1. As both electric and magnetic orderings are present at room temperature in BiFeO₃, it is an important material from the perspective of applications.

Table 1.1 Classification of ferroic orderings

Ferroic ordering	Polarizing field	Response
Ferroelectric	Electric field	Electric polarization
Ferromagnetic	Magnetic field	Magnetization
Ferroelastic	Stress	Strain

1.2. Bismuth ferrite (BiFeO₃)

In the field of multiferroics, bismuth ferrite BiFeO₃, in particular, has gained special attention due to its room temperature multiferroicity and functional properties that find direct applications in spintronics [17, 18], multiple state memory devices [19], photocatalytic activity [20], the photovoltaic effect [21], microelectronics [18] and so on.

1.2.1. Crystal structure

At room temperature, BiFeO₃ adopts rhombohedrally distorted perovskite [22, 23] structure with R3c space group. Its unit cell contains two formula units. Figures 1.2a and 1.2b show both the pseudo cubic and rhombohedral unit cell representation of BiFeO₃. Moreover, the rhombohedral unit cell is usually visualized in the hexagonal unit cell representation (see Figure 1.3), which has three fold rotation symmetries along the c-axis and contains six formula units of BiFeO₃.

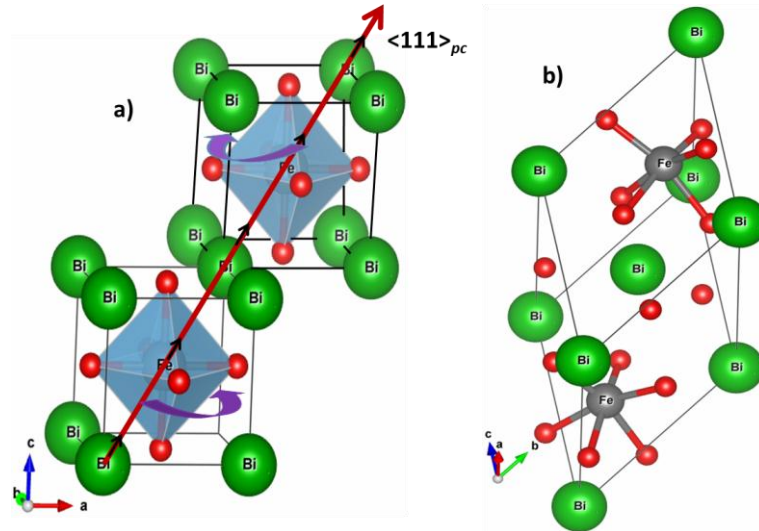


Figure 1.2 a) Pseudocubic and b) rhombohedral unit cell representation of BiFeO_3 .

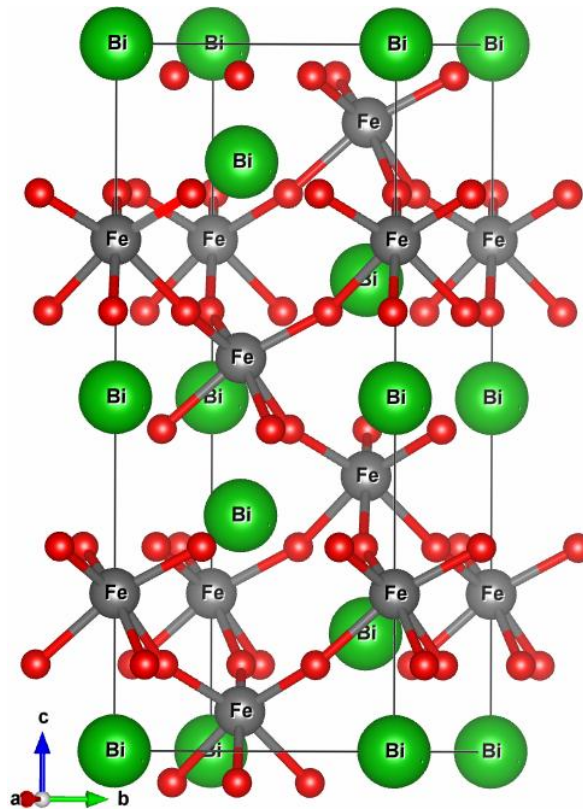


Figure 1.3 Hexagonal unit cell representation of BiFeO_3 .

The rhombohedral crystal structure can be derived from the ideal cubic perovskite structure (ABO_6). In the pseudo cubic unit cell representation of BiFeO_3 (see Figures 1.2a and 2b), the trivalent bismuth ion sits at the corner of the unit cell, whereas FeO_6 octahedra is located at the center of the cube. Here, the polar atomic displacements (shown as short

black arrows) caused by inter electronic repulsion on the Bi³⁺ along the $\langle 111 \rangle_{pc}$ direction and anti-phase tilting of the adjacent FeO₆-octahedra lead to a rhombohedral crystal structure (see Figure 1.3). This tilting, which is mostly seen in the case of perovskite structures [24-27], is because of the different ionic radii of Bi³⁺ ($R_{Bi^{3+}}^0 = 1.03 \text{ \AA} \text{ (VI)}$) and Fe³⁺ ($R_{Fe^{3+}}^0 = 0.55 \text{ \AA} \text{ (VI)}$), and is characterized by Goldschmidt tolerance factor,

$$t = \frac{R_{Bi^{3+}} + R_{O^{2-}}}{\sqrt{2}(R_{Fe^{3+}} + R_{O^{2-}})} = 0.9543. \text{ Importantly, the polar atomic displacement is responsible for}$$

the ferroelectric property of BiFeO₃. This is also observed in other similar perovskite materials [28].

1.2.2. Ferroelectric ordering in BiFeO₃

BiFeO₃ has ferroelectric ordering with a Curie temperature of 1100 K. The paraelectric phase, which has an orthorhombic crystal structure with Pbn space group, is deduced from the ideal perovskite cubic structure with out-of-phase tilting of FeO₆ octahedra along $\langle 110 \rangle_{pc}$ and in-phase tilting along $\langle 001 \rangle_{pc}$ without breaking the inversion symmetry [29]. Below the Curie temperature, there is out-of-phase tilting of FeO₆ octahedra and atomic translation of the cations along $\langle 111 \rangle_{pc}$ with breaking of the inversion symmetry resulting in the rhombohedral ferroelectric phase. Here, the cationic displacements correspond to ferroelectric distortion, whereas the FeO₆-octahedral tilting is called as antiferrodistortive rotation. In fact, this ferroelectric distortion is due to the stereochemical activity of the 6s lone pair of electrons over Bi³⁺ ion resulting in an asymmetric wave function of 6p orbitals. This leads to an asymmetric bonding between Bi and O thereby stabilizing the structure by off centering of Bi ion against the oxygen-sublattice. Further, the electrostatic repulsion between cations Bi and Fe causes a cooperative displacement of Fe ions, giving rise to a finite electric polarization in the rhombohedral phase of BiFeO₃ [30].

Moreover, the antiferrodistortive rotation may also arise because of the asymmetric bonding between Bi and O, which gets accommodated by rotation of the rigid FeO₆ octahedral units [31].

1.2.3. Magnetic Structure of BiFeO₃

BiFeO₃ has G-type antiferromagnetic spin arrangement with Neel temperature T_N= 647 K. This antiferromagnetic spin structure arises from a superexchange (SE) interaction between the neighboring spins of Fe ions mediated via oxygen atoms. Let us consider the interaction between nearest-neighbor (NN) and next-nearest-neighbor (NNN) spins of Fe ion as shown in the Figure 1.4. The Hamiltonian corresponding to superexchange interaction in BiFeO₃ is described in the equation below.

$$H_{SE} = J \sum_{\vec{r}, \vec{\alpha}} (\vec{S}_{\vec{r}} \cdot \vec{S}_{\vec{r} + \vec{\alpha}}) + J' \sum_{\vec{r}, \vec{\beta}} (\vec{S}_{\vec{r}} \cdot \vec{S}_{\vec{r} + \vec{\beta}}) \quad 1.1$$

Where $\vec{S}_{\vec{r}}$ is the spin of Fe at displacement vector \vec{r} , $\vec{S}_{\vec{r} + \vec{\alpha}}$ and $\vec{S}_{\vec{r} + \vec{\beta}}$ are the spins of NN and NNN of spin $\vec{S}_{\vec{r}}$ with displacement vectors $\vec{\alpha}$ and $\vec{\beta}$, and J and J' are the interaction parameter of NN spins and NNN spins of Fe, respectively. Here, the NN spins interact via one oxygen atom, whereas NNN spins interact through two oxygen atoms. Although the SE interaction in both NN and NNN spins favor antiparallel alignment of spins, the spin structure of BiFeO₃ stabilizes into G-type antiferromagnetic spins arrangement. This is because of the fact that the superexchange interaction is much stronger in case of NN spins as compared to NNN spins (the interaction parameter of NN spins ($J=4.38$ meV) is reported to be 10 times that of its NNN spins ($J'=0.15$ meV)) [29].

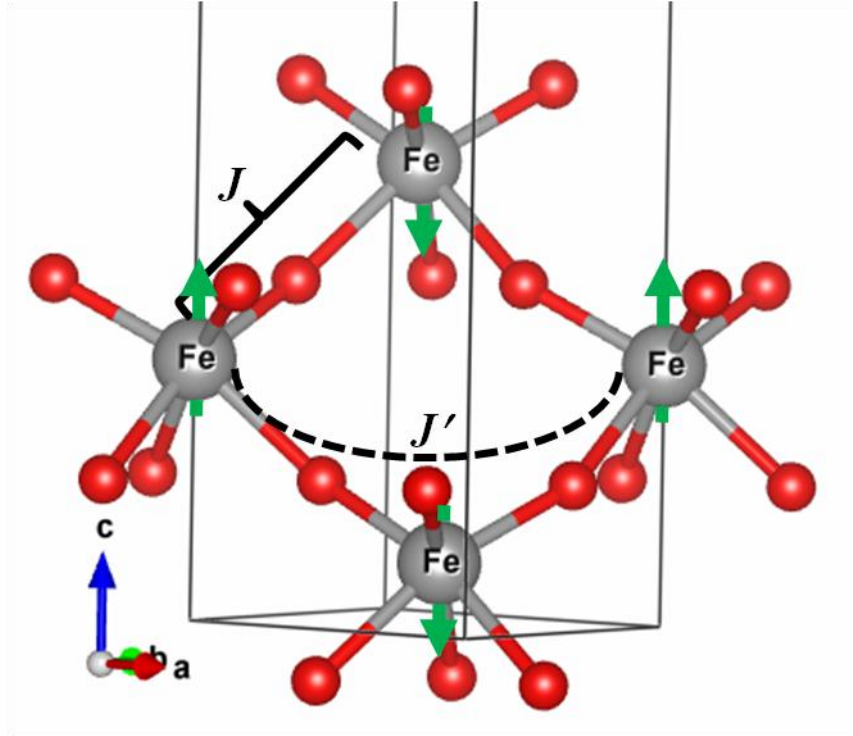


Figure 1.4 Super-exchange interaction between NN and NNN spins of Fe ion mediated via oxygen atoms.

Further, let us consider **Dzyaloshinskii-Moriya (DM)** [32] interaction, which arises because of the antisymmetric exchange interaction between neighbouring spins. If the spin-orbit coupling is considered as a perturbation to the superexchange interaction, the second order energy correction is of the form of antisymmetric exchange interaction. Thus, the microscopic origin of DM interaction is related spin-orbit coupling. In fact, the DM interaction can only exist in a material if the midpoint of neighbouring spins is not a point of inversion. This criterion is indeed satisfied in BiFeO₃, where the ferroelectric distortion causes the oxygen atom in the Fe-O-Fe bond to be displaced. The Hamiltonian for DM interaction is given as follows:

$$H_{DM} = - \sum_{\vec{r}, \vec{\delta}} \vec{D}_{\vec{\delta}} \cdot \left(\vec{S}_{\vec{r}} \times \vec{S}_{\vec{r} + \vec{\delta}} \right) \quad 1.2$$

where $\vec{D}_{\vec{\delta}}$ corresponds to DM vector at displacement vector $\vec{\delta}$. It can be noticed from

Equation 1.2 that the DM interaction gets minimized when the neighboring spins are

perpendicular to each other. Therefore, DM interaction favors perpendicular spin alignment whereas SE interaction favors antiparallel spin alignment. This competition between DM and superexchange interactions leads to a canted spin structure (see Figure 5) [33]. This canted spin structure gives rise to weak magnetic behavior in the material [34]. But in case of BiFeO_3 , these canted spin structure forms an array in a regular fashion over a distance of 62 nm along the $\langle 10\bar{1} \rangle_{pc}$ direction, which is known as spin cycloid (see Figure 6). The average magnetic moment over the spin cycloid is found to be zero as each spin has its mirror image in the cycloidal spin arrangement (see Figure 6). Therefore, the macroscopic magnetization of BiFeO_3 gets hampered by cycloidal spin arrangement.

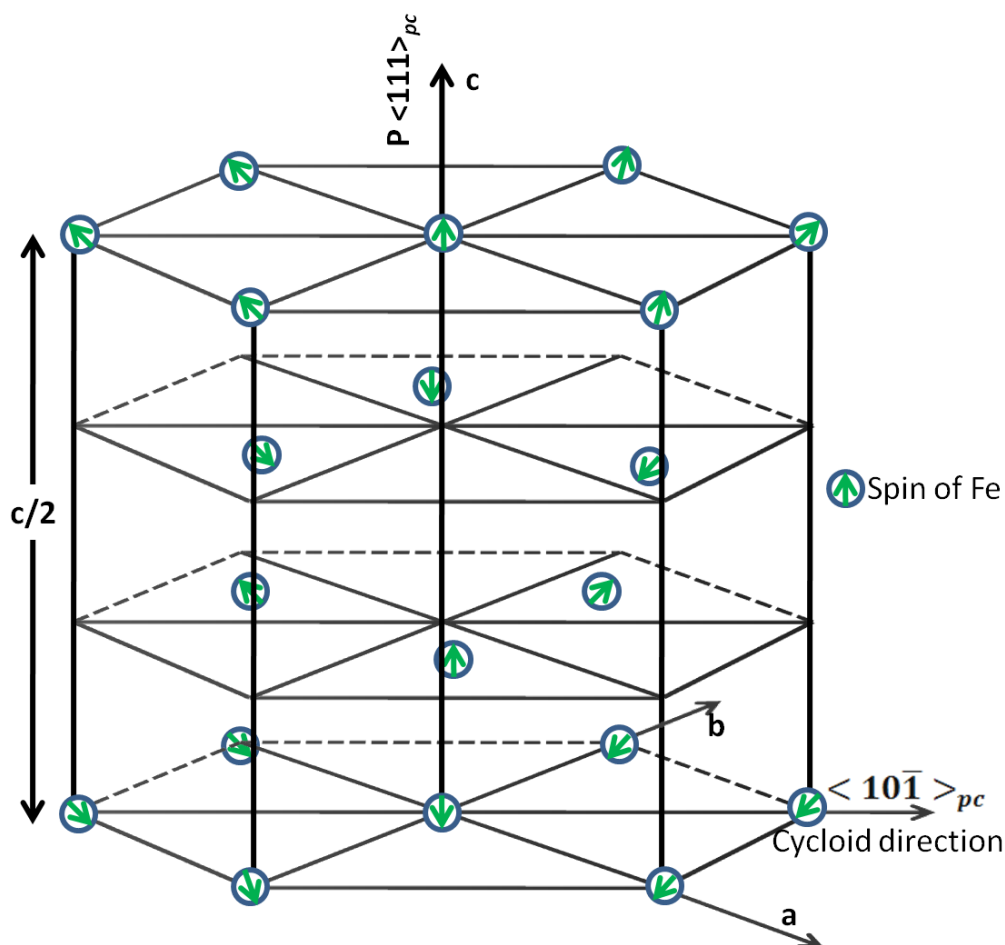


Figure 1.5 The magnetic structure of a portion of BiFeO_3 lattice is shown in hexagonal unit cell representation, where the spins of Fe are shown. The direction of spin cycloid is shown by the arrow pointed along $\langle 110 \rangle_{hex} \equiv \langle 10\bar{1} \rangle_{pc}$.

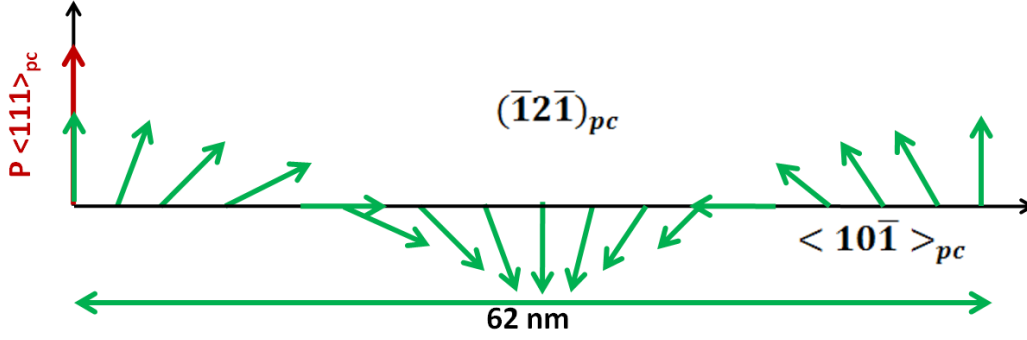


Figure 1.6 Schematic of spin cycloid in BiFeO₃.

Moreover, **single ion anisotropy** (SIA), which is related to the interaction between orbital magnetic moment and crystal field, plays a fundamental role in the cycloidal spin arrangement of BiFeO₃. In fact, large SIA is likely to suppress the spin cycloid, whereas small SIA brings anharmonicity in the modulation of the spin cycloid. The SIA Hamiltonian is given by,

$$H_{SIA} = -\kappa \sum_{\vec{r}, \vec{\delta}} (\vec{S}_{\vec{r}} \cdot \hat{c}) \quad 1.3$$

where κ , called the SIA coefficient, determines easy plane ($\kappa < 0$) or easy axis of anisotropy ($\kappa > 0$). In BiFeO₃, SIA mainly comes from the anisotropic deformation resulting from the ferroelectric distortion. The final form of SIA depends on the relative amplitudes of antiferrodistortive rotation and ferroelectric distortion, which are related to easy plane and easy axis anisotropies, respectively [35]. It is reported that BiFeO₃ has easy axis type anisotropy [36-42].

Furthermore, the spin cycloid in BiFeO₃ no longer remains harmonic as SIA is introduced by antiferrodistortive rotation and ferroelectric distortion. The anharmonicity in the modulation of the spin cycloid has been measured through NMR and Mossbauer spectroscopy [36-42]. It has been observed from these studies that a large anharmonicity is present in the spin cycloid. However, this anharmonicity of spin cycloid could not be detected through neutron diffraction measurements [39, 40, 43, 44]. Also, it is reported that

the SIA can be altered through applying electric field. Moreover, SIA increases with decreasing temperature [45] and hence there is an increasing trend in the anharmonicity in the spin cycloid with decreasing of temperature [36-42].

Therefore, many efforts like THz studies [46, 47] and neutron inelastic neutron scattering studies [48, 49] etc, have been made to probe the low energy excitation to understand the low energy spin dynamics.

1.3. Phonons, magnons and electromagnons in Bismuth ferrite

Phonons are collective lattice excitations of a solid, whose symmetries can be predicted via group theoretical calculation. As the rhombohedral unit cell with R3c space group contains 2 formula units of BiFeO₃ i.e. 10 atoms, the number of allowed vibrations is 30 (3 acoustical and 27 optical modes). The irreducible representation for optical modes of BiFeO₃ is given by $\Gamma_{\text{opt}} = 4A_1 + 9E + 5A_2$, where A_1 , A_2 and E are symmetry of the modes. Here, A_2 modes are optically inactive, whereas the optical active modes, $4A_1$ and $9E$, are both infrared and Raman active. These modes have been observed through several Raman and infrared spectroscopic studies [50-53].

Magnons are collective spin excitations, can be investigated to understand the underlying interactions among the spins and to get complete information on the magnetic structure. These magnon modes with polar activity are known as electromagnons, and are a special type of elementary excitations unique to multiferroic materials [54, 55].

The spin cycloid of BiFeO₃ produces zone center magnon modes, which are known as spin wave excitations (SWEs). These SWEs are categorized into two types: cyclon (Φ) and extracyclon (Ψ) modes. The cyclons are in-plane modes of spin cycloid whereas extracyclons are out-of-plane modes to the cycloid. The energies of Φ - and Ψ -modes are given by $E_c = m\varepsilon_c$ and $E_{ec} = \sqrt{m^2 + 1}\varepsilon_c$, where m is an integer. When a long wavelength electromagnetic radiation is made incident on the sample, it has been shown by de Sousa

and Moore [56] that the antiferromagnetic magnon mode gets effectively coupled at a multiple of the wave vector generating these two types of Φ - and Ψ -modes. However, introduction of SIA in the system, which also incorporates anharmonicity into the spin cycloid, greatly influences the spin wave excitation spectrum and selection rule [49, 56]. In fact the higher harmonics in the spin cycloid generated via SIA leads to splitting of each Φ_n -mode which are labeled as $\Phi_n^{(1)}$ and $\Phi_n^{(2)}$ as well as Ψ_n -mode which are labeled as $\Psi_n^{(1)}$ and $\Psi_n^{(2)}$ [57]. These SWEs mode frequencies are correctly predicted by Fishman et al. which have been observed in millimeter and far-infrared [58], Raman [55] and terahertz [46, 54] spectroscopic techniques although each of these technique has different selection rules [59]. In particular, Fishman et al showed that magnetic field splits the SWEs. He noticed that the Ψ_0 and $\Phi_1^{(1)}$ have same frequencies without magnetic field and become distinct on applying a magnetic field [57]. Conversely, SIA increases with decreasing temperature [45] and hence there is an increasing trend in the anharmonicity in the spin cycloid with lowering the temperature [36-42]. Thus it is necessary to carry out an extensive infrared low temperature investigation of SWEs to understand the underlying interactions and multiferroic property at low temperature [29].

1.4. Motivation

1.4.1. Magnetic property at low temperature and Phonon-magnon coupling effect in BiFeO₃

BiFeO₃ is reported to undergo several magnetic transitions at low temperatures. In recent studies [60-64], a phonon-magnon coupling effect at low temperatures is noticed in pristine and Ca-based BiFeO₃ samples through dielectric, magnetic and thermal conductivity measurements. In these studies, the transitions related to electric and magnetic order are observed at a temperature of 38, 150, 178, 223 and 250 K. Particularly, all these transitions are clearly seen in our earlier report on pristine BiFeO₃, which are observed through magnetocaloric measurement [60]. Moreover, it has been noticed [60, 65-73], that

the magnetic property of BiFeO₃ undergoes a remarkable change. Interestingly, Singh *et al.* [15] found in their magnetic study on BiFeO₃, a characteristic temperature (called, freezing temperature), which depends on the applied magnetic field in accordance with a power law behavior: $T_f(H) \propto H^\delta$ ($\delta = 2/3$). Thus, it shows the presence of de Almeida-Thouless (AT) line in BiFeO₃.

BiFeO₃ is also known to undergo several magnetic transitions at low temperature [60]. Rovillain *et al* [72] from their Raman study, detected two anomalies near 130 and 210 K due to the reorientation of spins. On the other hand, several other Raman scattering measurements have tried to explore the presence phonon-magnon coupling in BiFeO₃-based materials [50, 51, 55, 70, 72, 74-77]. It is also found that the magnons as well as the low energy phonons are sensitive to spin ordering at low temperature [73]. However, not many studies exist to see whether the phonon-magnon coupling is related to the spin reorientation transitions (SRTs). Optical spectroscopy is a very sensitive technique to study multiferroic material. It probes electric and magnetic order parameters as well as their coupled effect, giving rise to a quasiparticle in multiferroic materials named as electromagnon. Especially, infrared spectroscopy is an excellent technique to probe the behavior of magnons and phonons in BiFeO₃ [78-83]. However, till now, to the best of our knowledge, an extensive infrared spectroscopic study to understand the behavior of phonons, magnons and possibly electromagnons in BiFeO₃-based materials across the spin-reorientation transitions (SRTs) has not been carried out.

1.4.2. Influence of SIA and anharmonicity of spin cycloid on SWEs at low temperature

The antiferromagnetic order in BiFeO₃ is associated with a non-collinear spin structure arranged as a cycloid along $\langle 10\bar{1} \rangle_{pc}$ direction with a wavelength of 62 nm [84, 85]. Further, this cycloidal spin structure generates two types of optical magnetic modes known as spin wave excitations (SWEs) [55, 56]. The modes within the cycloid-plane are

known as cyclon modes while the out-of-plane components are known as extra-cyclons. These SWE modes are strongly influenced by anharmonicity of the spin cycloid as well as single-ion anisotropy (SIA) [49, 56, 57]. Below 290 K, the strengths of both these interactions show an increasing trend [36-42]. While a few studies have explored the SWEs at low temperature [56, 81, 86, 87], so far no effort has been made to study and understand the behavior of the high-frequency SWEs with respect to the SRTs.

1.4.3. Doping effect on SWEs

Technological application of BiFeO₃, in reality, is restricted by its cycloidal spin structure, which hampers the macroscopic magnetic property and linear magnetoelectric effect [88]. Thus, these properties need to be enhanced, which can be achieved through many ways. For instance, the methods to suppress the spin cycloid are by the application of hydro-static pressure [89], induced chemical pressure via doping [90, 91], high magnetic fields (~18 T) [88], and strain generated in thin-film form [92] and nanocrystals [93]. Enhanced magnetic property in case of nanoparticles has also been observed through surface-magnetization contributed via uncompensated surface spins [68], oxygen vacancy [93] and incomplete-cycloid due to particle size less than 62 nm [94]. In order to achieve improved magnetic and magnetoelectric properties, we have followed doping at Bi site in BiFeO₃ lattice with aliovalent Ba and/or Ca and tried to understand the resultant effects through studies using infrared spectroscopy, PFM and MFM techniques.

The aim of the present thesis is to investigate the above mentioned issues in pure and doped BiFeO₃ using FTIR reflectance spectroscopy in the Far- and the Mid-IR range. FTIR spectroscopy is a very sensitive probe for studying the lattice and magnetic excitations as well as the local structure in a solid. In addition, it can give information about electromagnons, if any, in BiFeO₃. While the phonon spectrum of BiFeO₃ covers the Far and the Mid-IR regions, the SWEs occur in the low energy range of the Far-IR spectrum.

This thesis explores the behavior of the SWEs and the phonons in BiFeO₃ ceramics as a function of temperature and composition. The changes observed in both the phonon and the magnon spectra are analyzed vis-à-vis the magnetic transitions occurring at low temperature. Towards this end, the following system comprising of pristine BiFeO₃ and Bi_{0.90}A_{0.10}FeO₃ (A= Ba, Ca) and Bi_{0.90}Ba_{0.05}Ca_{0.05}FeO₃ was chosen for the study.

In this thesis, low temperature investigation of the magnetic property and the behavior of infrared phonons of ceramic BiFeO₃ give evidence of magnon-phonon coupling effect. Besides, a two-magnon mode starts emerging below 150 K due to modification of non-collinear spin structure brought about by the reorientation of spin across the SRT. Moreover, the low temperature study of SWEs of ceramic BiFeO₃ finds a complete lifting of degeneracy of the SWEs at 250 K, which is because of increase in SIA generated through the reorientation of spin across the SRT. Additionally, a low temperature suppression of SWEs that manifests in the improvement of magnetic and magnetoelectric property of this compound is also investigated. Furthermore, the study of the behavior of phonons and SWEs in Bi_{0.9}A_{0.1}FeO_{2.95} (A = Ba, Ca) reveals the effect of doping-induced chemical pressure. In fact, Ca-doping completely results in a near-complete suppression of the SWEs.

1.5. Research objective and overview of the thesis

The objectives of this research work are: (i) To investigate the magnetic property of pristine bismuth ferrite at low temperature and to correlate it with the low temperature behavior of infrared phonons and SWEs in this compound and in the process get evidence for phonon-magnon coupling and electromagnons. (ii) To study doping-induced enhancement of magnetic property through suppression of SWEs in Bi_{0.9}A_{0.1}FeO_{2.95} (A = Ba, Ca) samples using IR spectroscopy as well as PFM and MFM techniques.

Chapter 1 includes a brief overview of multiferroicity and its potential applications, ferroelectric and ferromagnetic properties of BiFeO_3 , phonons, magnons, electromagnons and magnon-phonon coupling. A comprehensive discussion of the magnetic structure, SWEs and the vibrational properties of BiFeO_3 is also presented based on the existing literature. The chapter ends with scope of the work presented and the investigations carried out for the present thesis.

Chapter 2 presents the details of synthesis procedures of pristine and doped BiFeO_3 samples and the experimental techniques used for the investigation of their structure, vibraional and magnetic properties. Infrared and Raman spectroscopic techniques are described in detail. Data analysis procedures for curve-fitting of vibrational spectra are also discussed. A brief discussion on vibrating sample magnetometry (VSM), X-ray diffraction, Electron Paramagnetic Resonance (EPR) and atomic force and peizo force microscopy (AFM and PFM) is provided.

In **Chapter 3**, a comprehensive study of phonons of BiFeO_3 through temperature-dependent infrared reflectivity measurements is carried out and correlated with the magnetic measurements made on the same sample using VSM-SQUID [95]. From the magnetic measurements, two spin-reorientation transitions (SRTs) at 257 and 150 K are noticed. In the infrared measurements, all the 13 modes allowed by the rhombohedral crystal structure with $R3c$ space group are observed and assigned with their symmetries. The polar mode $E(\text{TO1})$ is found to show anomalous behavior in frequency across SRTs pointing to the evidence of magnon-phonon coupling. Interestingly, birth of two new magnon modes at 106 and 112 cm^{-1} are observed below 150 K. The emergence of the two-magnon mode below 150 K is attributed to modifications in the non-collinear magnetic structure.

Chapter 4 involves a detail investigation of spin wave excitations of BiFeO_3 at low temperature through far-infrared reflectivity measurements. The emergence of new magnon

modes at 106 and 112 cm^{-1} modes below 150 K prompted us to take a detailed look at the low temperature behavior of spin wave excitations in pristine BiFeO_3 through infrared reflectivity measurements [95]. All the observed SW modes could be assigned based on the scheme of Fishman et al [57]. A total lifting of degeneracy of all the SWEs is noticed at 250 K which is concomitant with an increase in SIA below this spin reorientation transition. Correlated changes in the frequencies and the strength of SWEs with the SRTs at low temperature are observed. A decrease observed in the intensity of the SWEs below 250 K is attributed to the suppression of SWEs. This is understood through a combined increase in SIA and anharmonicity of the spin cycloid which destroys the cycloid leading to suppression of SWEs. This study gives evidence of the improvement of magnetic and magnetoelectric interactions at low temperatures. In a complementary manner, our EPR studies on BiFeO_3 give clear evidence of SRTs as well as insight into the magnetic properties of BiFeO_3 . The sharp increase in degree of spin canting below 130 K is well correlated with improved magnetic and magnetoelectric properties at low temperature. It is also noticed from the EPR studies that the spin-phonon interaction increases at low temperatures.

Chapter 5 deals with the Study of phonons and spin wave excitations in $\text{Bi}_{0.9}\text{A}_{0.1}\text{FeO}_{2.95}$ ($\text{A} = \text{Ba}, \text{Ca}$). The cycloidal spin structure in BiFeO_3 basically hinders the macroscopic magnetization and the linear magnetoelectric effect in this material. To improve the magnetic and ME properties, therefore, it is important to suppress the cycloidal spin structure. One way of achieving this is through chemical substitution. To this end, the behavior of phonons and magnons in $\text{Bi}_{0.9}\text{A}_{0.1}\text{FeO}_{2.95}$ ($\text{A} = \text{Ba}, \text{Ca}$) is investigated through infrared reflectivity measurement [96]. All the allowed 13 modes are observed in case of all the samples. The phonon modes show systematic hardening with increase of Ca-content in the doped samples in agreement with the reduction of unit cell volume as found from the Rietveld refinement results. This observation suggests that doping effectively induces

chemical pressure into the lattice. On the other hand, there is an increase in the number of SW modes in the case of the doped samples due to the lifting of degeneracy, which we could assign following the scheme of Fishman et al [57]. It is further noticed that, a complete removal of the degeneracy of the SW modes is taking place for Ca-doped and co-doped samples while the Ba-doped sample shows only partial lifting of the degeneracy. From this it is understood that Ca- and co-doping with both Ca and Ba at the same site in BiFeO₃ leads to significant increase in SIA and thus complete removal of degeneracy of the SWEs. Moreover, the spectral area in the magnonic part of the IR spectra is found to substantially decrease in the case of both the Ca-doped and the co-doped samples in correlation with the suppression of SWEs possibly brought about by doping induced increase in SIA and anharmonicity of cycloid. This study has revealed that the local structure and the magnetic interactions in BiFeO₃ could be effectively modified with induced chemical pressure by Ca doping at Bi-sites of BiFeO₃. The doping induced changes consequently lead to an improvement in the magnetic and magnetoelectric properties of BiFeO₃.

Chapter 6 involves Piezoelectric and magnetic force microscopy studies on pristine and doped BiFeO₃ samples. This chapter augments the findings of the previous chapter in terms of getting an understanding of the ferroelectric and magnetic nature of the pure and doped BiFeO₃ through PFM and MFM studies. From the PFM studies, distributions of piezo domains could be observed for all the samples studied. Subsequently, piezo force spectroscopy was carried out on each of the samples using a dc bias from +10 to -10 V, from which phase and Mag loops were distinctly observed for all the samples. We find that d_{33} values extracted from these measurements decreases noticeably from the pristine BiFeO₃ case to the Ca-doped case. Concomitantly, the MFM studies on these samples show enhanced magnetism for the Ca-doped BiFeO₃ as compared to the pristine sample. These

results are in support of the suppression of the SWE modes as observed from the infrared data and hence a consequent enhancement in the magnetic property in Ca-doped BiFeO₃.

Chapter 7 includes the summary of major findings of this thesis, and the future scope and direction of this work.

Chapter 2

Experimental techniques

In this chapter, a brief introduction to history of the samples used and the experimental techniques employed for the thesis works have been covered.

2.1. Samples' history

2.1.1. Pristine BiFeO₃ sample

BiFeO₃ ceramic samples were synthesized through modified sol-gel route [60, 97]. At first citric acid (C₆H₈O₇), which was taken in a molar ratio of 1:1 with metal nitrates (iron nitrate and bismuth nitrate), was dissolved in a solvent of 100 ml distilled water and ethanol. Iron nitrate and bismuth nitrate with a molar ratio of 1:1.05 were dissolved in the above solution and thoroughly mixed following which, 5 ml of nitric acid (HNO₃) and 5 ml of hydrogen peroxide (H₂O₂) were added to the solution with constant stirring. Then the whole solution was refluxed for 2 hours at 90 °C to form a gel, which was dried at 300 °C for 1 hour to get bismuth ferrite precursor in powder form. The obtained powder is calcined at 600 °C for one hour and then sintered at 850 °C to get the desired phase pure sample as confirmed from X-ray diffraction (XRD) measurements. A Rietveld refinement of the XRD patterns of the sample was carried out with rhombohedral unit in R3c space group by using General Structure Analysis System (GSAS) software. The refined unit cell parameters and cell volume were found to be $a=b=5.581(2)\text{\AA}$, $c=13.879(5)\text{\AA}$ and $V=374.379\text{\AA}^3$, respectively. The density of the sintered BiFeO₃ pellet was calculated to be about 90 % of its theoretical density of 8.34 gm/cm³. The structural properties of the sample were studied using various techniques including x-ray diffraction and x-ray photoelectron spectroscopy [60, 98]. The dielectric and magnetic characteristics of the sample were also measured and analyzed [60-64, 97, 98].

2.1.2. Doped BiFeO₃ ceramic samples

Polycrystalline samples of BiFeO₃ (BFO), Bi_{0.9}Ba_{0.1}FeO_{2.95} (BBFO), Bi_{0.9}Ba_{0.05}Ca_{0.05}FeO_{2.95} (BBCFO) and Bi_{0.9}Ca_{0.1}FeO_{2.95} (BCFO) were synthesized by the modified sol-gel route as described in section 2.1.1. The powder samples thus obtained were pelletized and sintered at 1123 K for 6 h. The Rietveld refinement of the XRD patterns of all the doped samples was carried out using GSAS software for rhombohedral unit cell in R3c space group [97]. These structural refinements revealed a decrease in the unit cell volume of all the doped samples with the unit cell volume of the Ca-doped samples being the least among all the doped samples (Table 2.1). The composition of the samples were determined from the analysis of energy dispersive X-ray spectra [97]. In the case of BBFO and BCFO, there is a structural transition from rhombohedral to orthorhombic crystal structure for dopant concentration, $x \geq 0.1$ based on the literature as discussed by Ramachandran *et al.* [22]. Therefore, samples with 10% dopant concentration have been chosen for the work described in this thesis with a view to retain the rhombohedral phase as in pristine BiFeO₃ and still be able to study the effect of the dopants.

Table 2.1 Unit cell parameters of pristine and doped BiFeO₃ ceramic samples

Sample name	Composition	a (Å)	c (Å)	Volume (Å ³)
BFO	BiFeO ₃	5.581	13.879	374.379
BBFO	Bi _{0.9} Ba _{0.1} FeO _{2.95}	5.569	13.769	369.803
BBCFO	Bi _{0.9} Ba _{0.05} Ca _{0.05} FeO _{2.95}	5.574	13.697	369.781
BCFO	Bi _{0.9} Ca _{0.1} FeO _{2.95}	5.570	13.643	366.599

Ba-doping improves ferroelectric property due to better densification of the Ba-doped samples, as Ba²⁺-ion has larger ionic radius than Bi³⁺-ion [97]. It is found that BBCFO has better magnetodielectric behavior than BBFO and BCFO samples [97]. It should be noted here that all the investigated samples were sintered under same heat treatment conditions and for the same duration [97].

In this thesis, these pristine and doped BiFeO₃ ceramic samples were considered for our studies using spectroscopic and microscopic techniques. The optical (phonon and magnon modes) and magnetic properties of these samples were extensively investigated at low temperatures using techniques like Fourier-transform infrared spectroscopy (FTIR), Raman scattering, superconducting quantum interference vibrating sample magnetometry (SQUID- VSM) and electron paramagnetic resonance (EPR) spectroscopy. Further, the ferroelectric and magnetic domains of the studied samples have been acquired through piezoresponse and magnetic force microscopy (PFM and MFM).

2.2. Fourier-transform infrared (FTIR) spectrometer

Infrared (IR) spectroscopy deals with the study of interaction between infrared light with sample which is based on the absorption of characteristic frequencies by the sample. In spectroscopy, a dispersive element is generally used to separate the frequencies and frequency sensitive detectors are needed to detect each frequency. As the infrared photon flux in a lab source is low, further use of dispersive elements to separate the frequencies even lowers the throughput at detectors. Therefore, in the field of IR spectroscopy, FTIR spectrometer gains popularity where a mathematical method (Fourier transform technique) is used to separate the frequencies instead of any dispersive elements like grating or prism. The advantages of using FTIR over IR spectrometer are high throughput, simultaneous measurement of all the frequencies (multiplex advantage), mechanical simplicity (very few moving parts), and internal calibration with He-Ne laser.

2.2.1. Basic principles and instrumentation of FTIR

The main components of FTIR spectrometer are infrared source, Michelson interferometer, and infrared detector (Figure 1). The Michelson interferometer is known as the heart of the FTIR instrument. It essentially consists of a beamsplitter, fixed and movable mirrors. If a collimated beam of monochromatic light of frequency ν ($=1/\lambda$) is made to fall

on an ideal beamsplitter, 50% of the incident radiation will be reflected to one of the mirrors while 50% will be transmitted to the other mirror. The two beams which get reflected from the fixed and movable mirrors, return to the beamsplitter where they recombine and interfere. Finally, this light interacts with the sample after which it is measured by the detector.

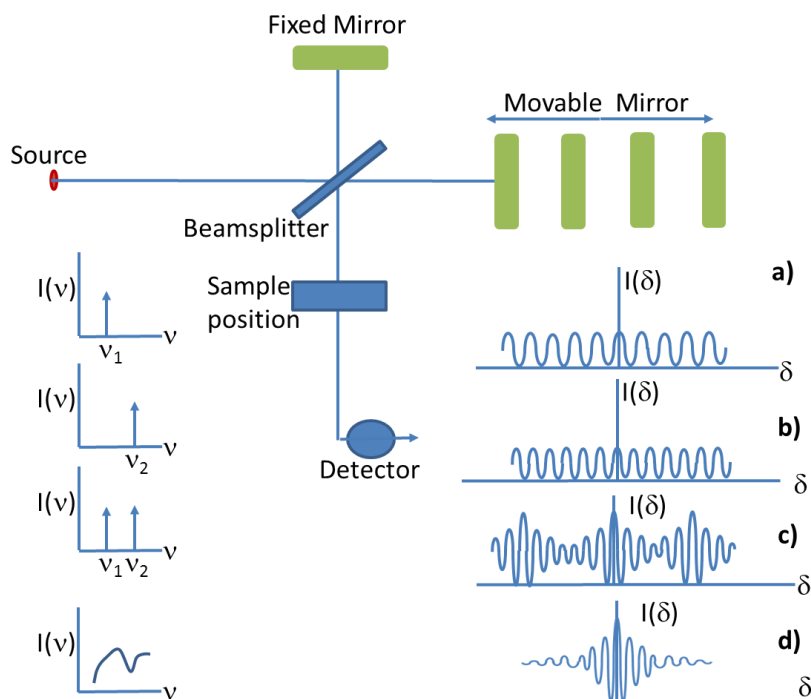


Figure 2.1 Schematic of FTIR spectrometer. The cosine functions (a) and (b) are the Fourier transform of their corresponding monochromatic light of frequency ν_1 and ν_2 , respectively. The beat pattern (c) of two monochromatic light sources of frequencies ν_1 and ν_2 . (d) Interferogram of a broad band light source.

The detector detects the intensity of light as a function of path difference, δ (also known as retardation), introduced by the movable mirror, and the resulting pattern is known as interferogram ($I(\delta)$). Let us consider the case of a monochromatic light source of wavelength λ . For zero or even multiples of $\lambda/2$ path difference, the intensity measured by the detector will be maximum due to constructive interference. Whereas for odd multiple of $\lambda/2$ path difference, the intensity at detector will be zero due to destructive interference. Therefore the interferogram $I(\delta)$ of a monochromatic light of frequency ν ($=1/\lambda$) is a cosine

function of path difference with periodicity λ , which is equal to its wavelength. As another example, for a source emitting two frequencies, the cosine functions with periodicities λ_1 and λ_2 corresponding to the frequencies ν_1 and ν_2 are superposed to form a beat pattern, as shown in Figure 1c. Extending this argument, the $I(\delta)$ of a continuum source is a superposition of cosine functions corresponding to all the frequencies coming from the source (Figure 1d). It shows maximum intensity, called centreburst, at zero path difference (ZPD) and then dies down on both sides. This is because of the fact that the constructive interference for all the frequencies can only take place at ZPD. If, now, an absorber is kept at the position marked 'sample' in Figure 2.1, those frequencies that match the characteristic vibrational frequencies of the sample get absorbed by the sample. The interferogram reaching the detector then contains information regarding all the missing frequencies. Finally, the interferogram is Fourier transformed to obtain a spectrum which contains all the information of the characteristic absorption features of the sample.

2.2.2. Fourier-Transformation

The interferogram, $I(\delta)$, and the spectral intensity, $I(\nu)$, are related by the Fourier-transformation (FT) given by:

$$I(\delta) = \int_0^{\infty} I(\nu) \cos(2\pi\nu\delta) d\nu \quad 1.1$$

$$I(\nu) = \int_{-\infty}^{\infty} I(\delta) \cos(2\pi\nu\delta) d\delta \quad 1.2$$

Equation 1.1 represents the interferogram which is the continuous summation over all the frequencies from 0 to ∞ , whereas equation 1.2 gives us the spectral intensity, which is the inverse FT of interferogram measured at path difference from $-\infty$ to ∞ . Therefore, $I(\nu)$

and $I(\delta)$ are inter convertible by the mathematical method of Fourier Transform [99]. Here it can be noticed that the path difference and wavenumber form conjugate pairs.

2.2.3. Apodization function

The mathematical process of Fourier transformation assumes infinite boundaries (path difference of $\pm \infty$). In reality, the movable mirror of the Michelson interferometer travels a finite distance and hence can only create finite path difference. Because of this box-car type of truncation, the spectrum obtained from the FT of the interferogram of finite boundary is a sinc function with a finite width along with positive and negative side lobes [99]. Therefore, the interferogram of finite boundary needs to be convoluted with a suitable mathematical function (apodization function) to remove the side lobes. A number of apodization functions are available for use, which are triangular, four point and so on.

2.2.4. Resolution

The resolution for an FTIR instrument is given by the inverse of the maximum path difference introduced by the movable mirror. For instance, a path difference of 10 cm will result in a resolution of 0.1 cm^{-1} .

2.2.5. Bruker Vertex 80v FTIR spectrometer

The FTIR spectrometer employed in this research work is Bruker Vertex 80v spectrometer whose main optical layout is as shown in Figure 2.2. It has a working range of $10\text{-}50000 \text{ cm}^{-1}$, different sets of sources, beamsplitters and detectors to cover this very far-IR to UV spectral range and a maximum resolution of 0.02 cm^{-1} . It operates in vacuum thereby mitigating any interference from atmosphere. It has an integrated OPUS control and evaluation software using which transmission and reflectance spectra have been acquired and analyzed. Some of the accessories used in this work other than the built-in options are W-type reflectance unit, liquid He cooled bolometer and Hg source. More details of the various parts and the operation of the spectrometer are available in the Bruker Vertex 80v manual [100].

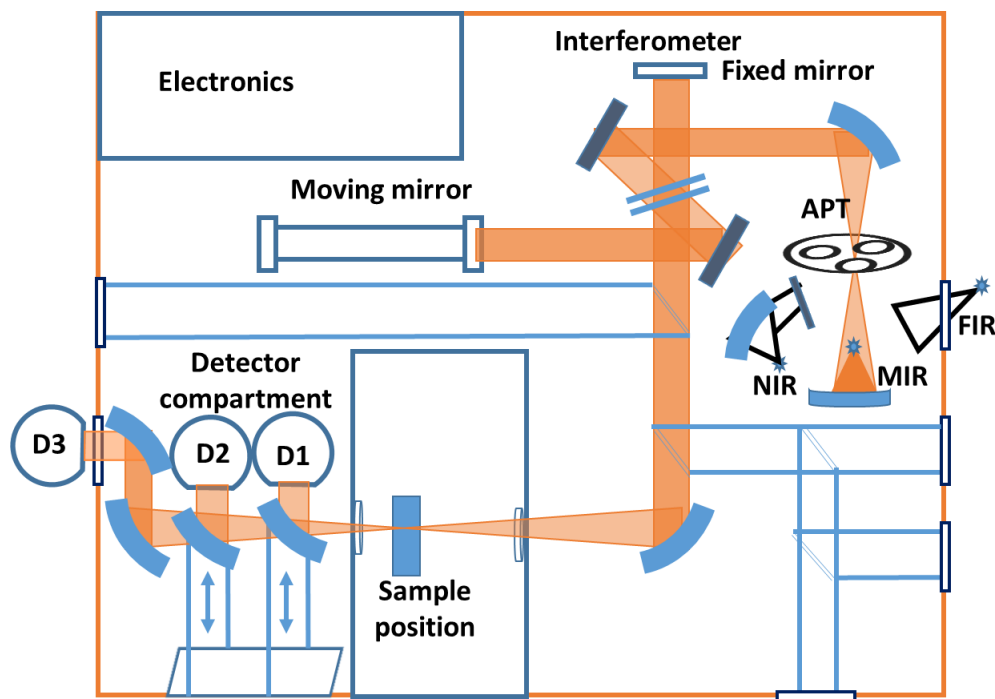


Figure 2.2 Optical lay-out of Bruker Vertex 80v FTIR spectrometer.

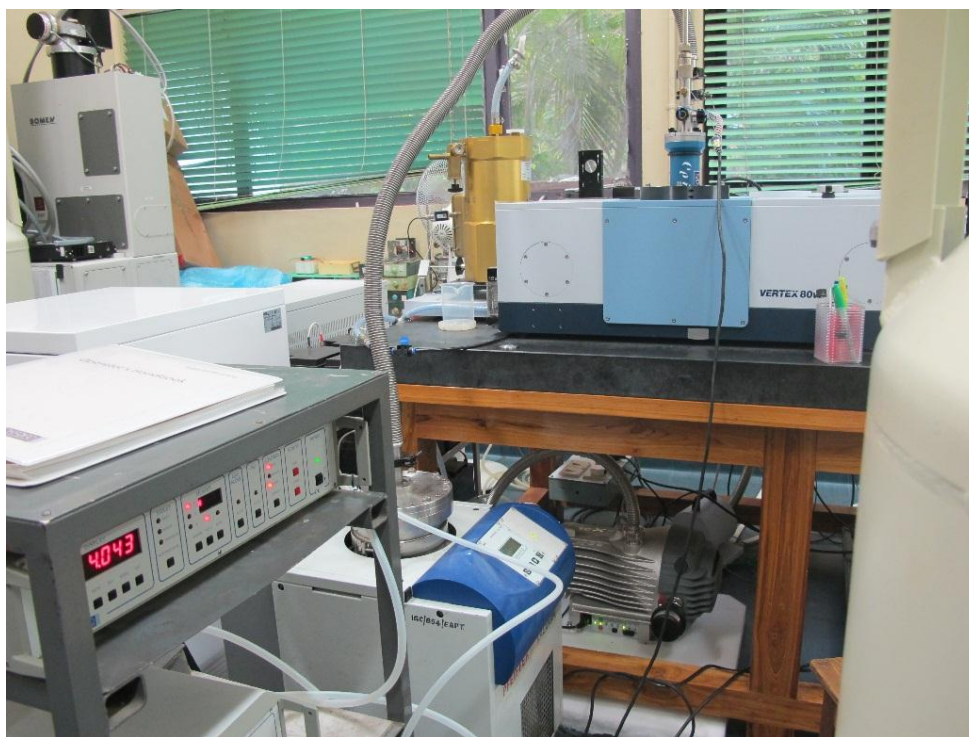


Figure 2.3 A photograph of Bruker Vertex 80v FTIR spectrometer setup

For low temperature experiments (500 - 4.2 K) a continuous flow Optistat CF-V Cryostat (Oxford instruments, UK) mounted with appropriate windows was interfaced with the sample chamber. The temperature stability was better than ± 1 K. A photograph of the facility is shown in Figure 2.3.

2.3. Raman Spectroscopy

Raman spectroscopy is based on inelastic scattering of a monochromatic light by the sample. When light of frequency ν_0 is made to incident on a solid, most of it is scattered at the same frequency (elastic scattering), while a small fraction gets scattered inelastically with frequencies $\nu_0 \pm \nu_m$, where ν_m are the characteristic vibrational frequencies of the solid. The quantum mechanical description of Raman scattering is shown in Figure 2.4. where the sample goes from ground state to a virtual state when an incident radiation of frequency ν_0 is made to fall on that and returns to the ground state by emitting radiation of the same frequency as the incident frequency (Rayleigh scattering) or of a lower frequency by returning to a vibrational excited state (Stokes scattering). On the other hand, the sample may also go from an excited state to a virtual state by interacting with the laser light and then return to the ground state by emitting a light of higher frequency (antistokes scattering).

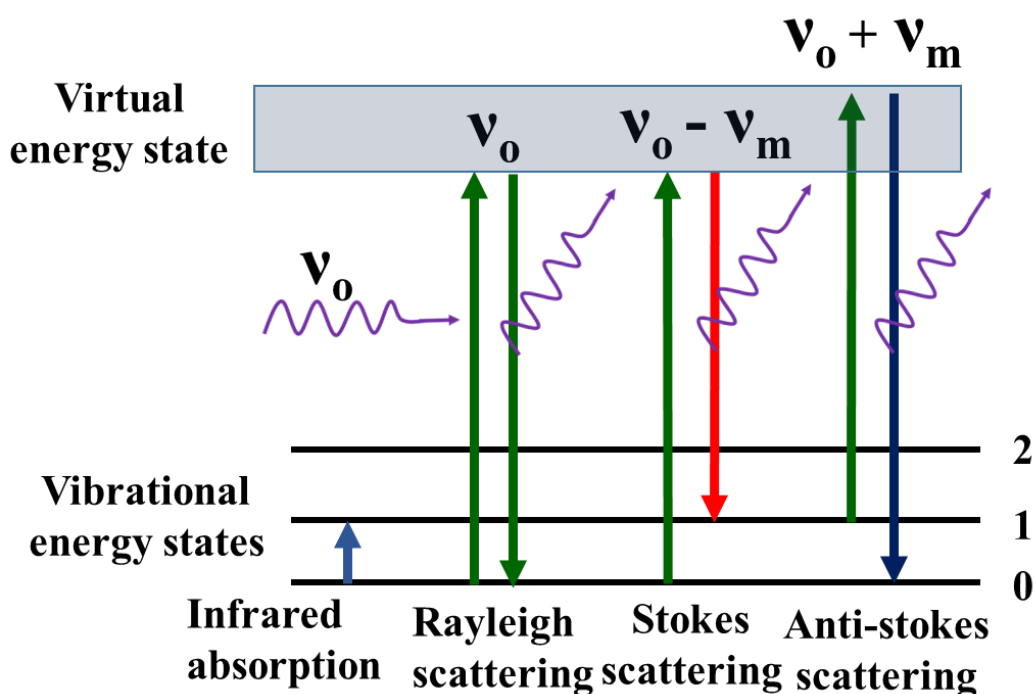


Figure 2.4 Quantum Mechanical description of Raman spectroscopy.

2.3.1. Instrumentation

The important components of Raman spectrometer are laser sources, optical filters, grating and detectors (Figure 2.5). The laser beam passes through a holographic filter, which makes

the beam as pure plane wave, and then reaches to sample surface with the help of combination of lenses, mirrors and beamsplitter. The back scattered laser light passes through optical filters, which filters out the predominant Rayleigh scattering (99.999 %), and allows Raman (stokes and antistokes lines) scattered signals. Finally the Raman signals is measured by charge coupled device (CCD) detectors. The name of a few optical filters are notch filters, tunable filters, laser stop apertures, double and triple spectrometric systems. There are a number of laser sources with wavelength 532, 514, 488 and 1064 nm used for Raman measurement. The main reason for switching of laser source is to avoid any undesirable fluorescence produced by the sample (usually in the visible range) and at the same time to maintain optimal intensity of the Raman scattered light as scattered intensity is inversely proportional to the fourth power of the incident wavelength $\left(I \propto \frac{1}{\lambda^4}\right)$.

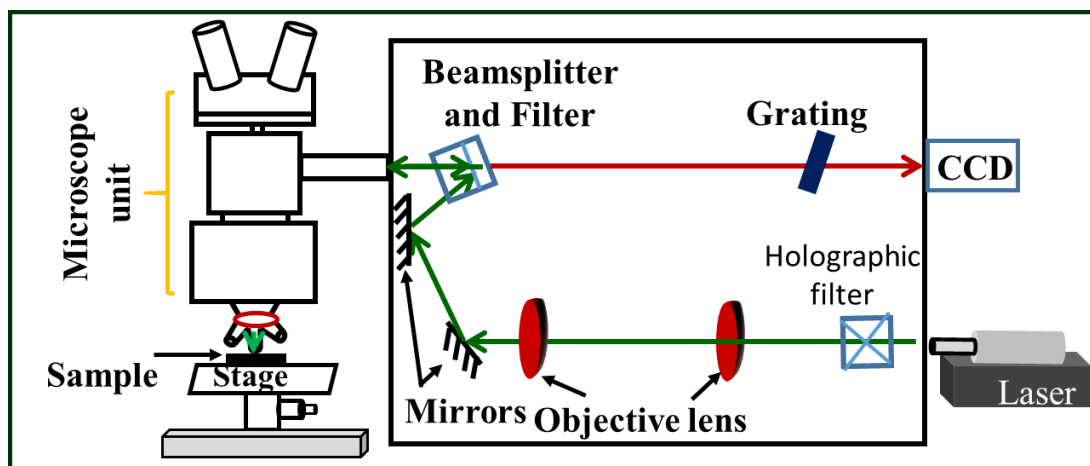


Figure 2.5 Schematic of a Raman spectrometer.

2.4. SQUID-VSM magnetometer

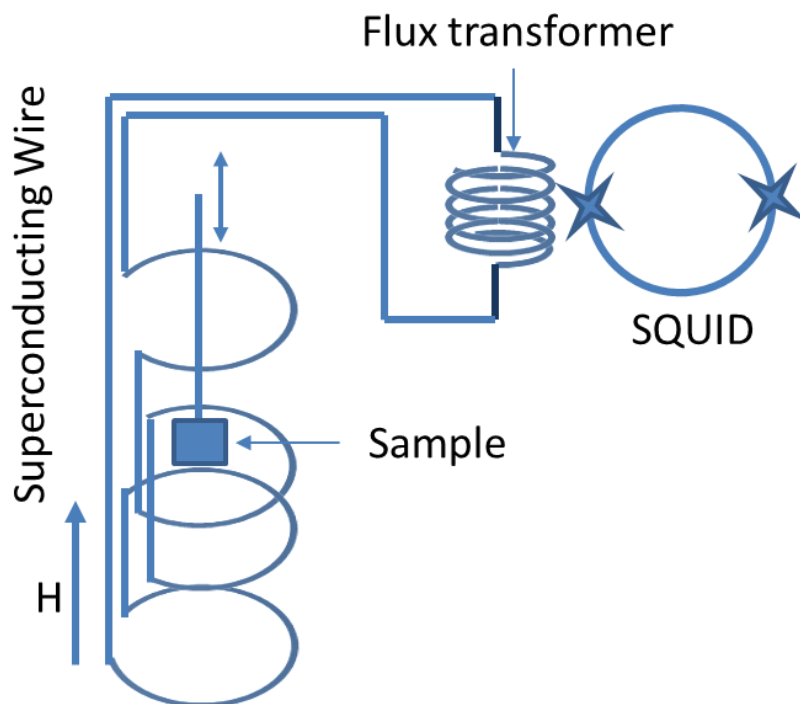


Figure 2.6 Schematic of a SQUID-VSM magnetometer.

Superconducting quantum interference device based vibrating sample magnetometer (SQUID-VSM) is a magnetometer, which is used to measure magnetic property over an extended range of magnetic field (H) or temperature (T). Here the combination of VSM and SQUID allows us to carry out high sensitive measurements at very high speed (10^{-8} emu averaging over 10 s). Figure 2.6 displays the schematic of VSM-SQUID magnetometer. In SQUID-VSM magnetometer, the sample vibrates at center of the pickup coils, which are placed under external magnetic field. The pickup coils are coupled inductively with the SQUID element, which converts change in flux through the sample movement in to voltage. The voltage is detected through lock-in amplifier.

2.5. EPR spectroscopy

EPR spectroscopy deals with the study of resonance absorption of microwave power by the spins of unpaired electrons in the presence of an externally applied static magnetic field. In EPR spectroscopy, the spins of unpaired electrons get excited, which is analogous to nuclear magnetic resonance, where nuclear spins get excited.

2.5.1. EPR spectrometer

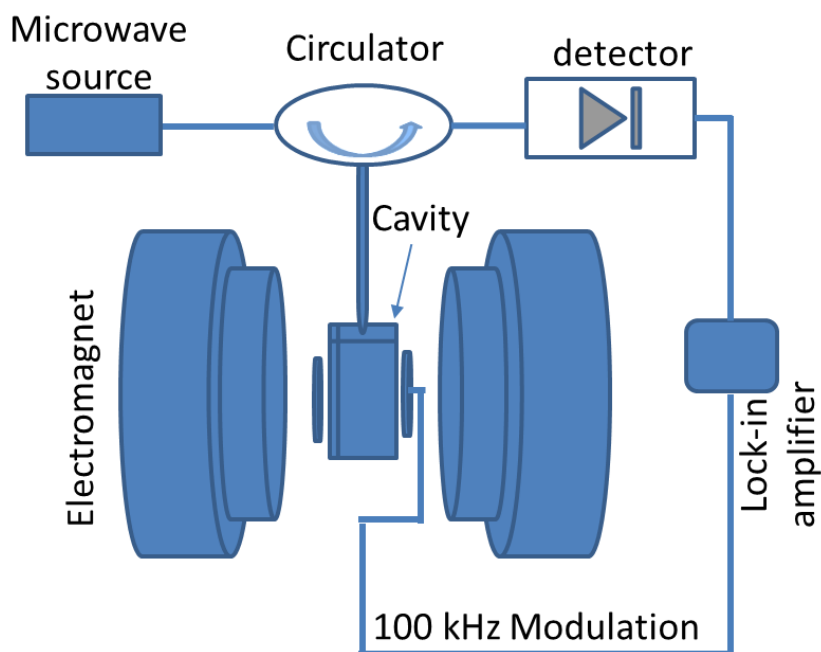


Figure 2.7 Schematic of an EPR spectrometer.

Figure 2.7 shows the schematic of field sweep EPR magnetometer, which requires important components like microwave source, static magnetic field, resonant cavity and a detector. The microwave radiation from the source is directed towards a sample kept in the resonant cavity. The microwave cavity is located at the center of static magnetic field generated by an electromagnet. The strength of the magnetic field can be linearly increased by slowly increasing current in the electromagnet. The reflected signal from the sample placed in the resonant cavity is recorded by the detector as a function of the sweeping magnetic field. EPR spectroscopy of solids provides a wealth of information on local symmetry, fine and hyperfine structure, spin dynamics, etc.

2.6. Atomic force microscopy (AFM)

Atomic force microscopy (AFM) is an imaging technique, which acquires images of sample surface through scanning with a cantilever. While scanning the sample surface generates a deflection force on the cantilever, which is measured by a laser light reflected off of the cantilever into a quadrant photodiode. The primary modes of operation during the

scanning of sample surface are contact or tapping mode. In contact mode of operation, the cantilever tip is in contact with the sample surface. Therefore height imaging (topography) is acquired through surface scanning. While in tapping mode, the cantilever is excited to oscillate near the resonant frequency of the cantilever. In this mode, topography and phase image can be acquired.

2.7. Piezoelectric force microscopy (PFM)

Piezoelectric force microscopy (PFM) is an advanced operational mode of scanning probe microscopy, where a conductive tip is used to scan the sample surface. It gives information regarding piezoelectric property of the material. It measures nanoscale topography of the surface and mechanical response of the material with respect to applied voltage. It is based on the converse piezoelectric effect, which is the internal mechanical strain generated via applied electric field. The schematic diagram of PFM is shown in Figure 2.8. When a small ac voltage is applied, the sample will have periodically relative expansion and contraction. The deformation of the sample generated via the applied voltage is of the order of nanometer to picometer, and is measured by the deflection in the cantilever.

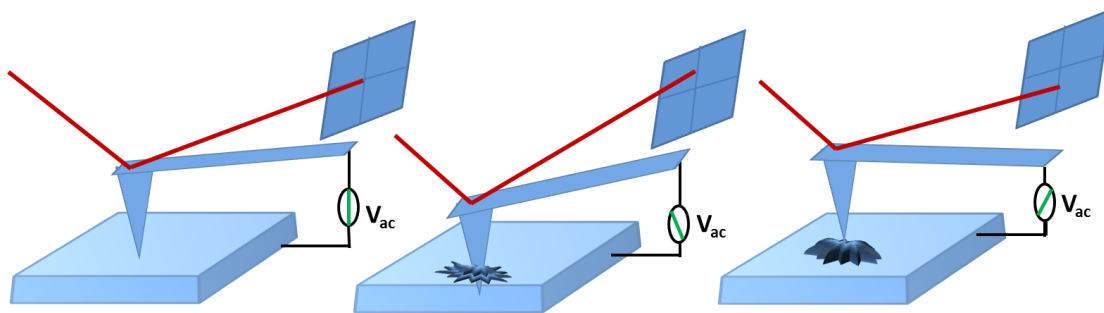


Figure 2.8 PFM cantilever deflection versus applied voltage.

2.8. MFM

Magnetic force microscopy (MFM) is another advanced operational mode of scanning probe microscopy, which is used to study the magnetic property of the sample. A sharp magnetized tip is used as a probe in MFM, which is usually made with magnetic coating over the silicon tip. It detects the magnetic interactions between tip and sample,

which are used to image the spatial distribution of magnetic fields and thus reconstruct the magnetic structure of the sample. During the measurement, the MFM tip is well lifted off from the sample surface in such a way that the magnetic forces (long range) and the atomic forces (short range) between the tip and sample surface can be distinguished from each other. MFM operates in tapping mode, where the resonance frequency of the tip is in the range of 10-100 kHz. MFM maps the phase and the resonant frequency during the scanning of sample surface at a constant height. A repulsive magnetic force between the tip and sample surface shifts the resonance frequency to higher value and there is an increase in the phase shift resulting in brighter contrast, while an attractive magnetic force shifts the resonance curve to lower frequency and there is a decrease in the phase shift resulting in dark contrast. MFM operates either in single pass or dual pass mode. In single pass mode, the tip scans the sample surface at a constant height. While in dual pass mode, the sample surface is scanned twice. In the first pass, the tip is in contact mode to elucidate topography, whereas in the second pass the tip is kept at a constant height and follows the contours of the topography line to map the phase.

Chapter 3

Investigations of phonon behavior across spin reorientation transitions in BiFeO₃

This chapter deals with a comprehensive study of phonons through infrared reflectivity measurements across the spin-reorientation transitions to explore magnon-phonon coupling effect in BiFeO₃.

3.1. INTRODUCTION

The multiferroic bismuth ferrite undergoes several magnetic transitions at low temperatures due to the coupled effect between the spin, lattice and/or charge degrees of freedom [50, 51, 55, 60, 61, 70-77, 87, 101-105]. To understand the magnon-phonon coupling effects in multiferroic BiFeO₃, several Raman scattering measurements have been performed [50, 51, 55, 61, 70, 72, 74-77, 87, 101-105]. In particular, the Raman scattering study on single crystals of BiFeO₃ by Rovillain et al [72] suggested that there are two magnetic transitions at 210 and 130 K brought about by spin reorientation. Besides, the low-frequency phonon, magnons are found to be sensitive to spin-reorientation transitions [73].

In a couple of recent studies on the BiFeO₃ ceramic [60-64], the phonon-magnon coupling effect at low temperatures was noticed in pristine and Ca-based BiFeO₃ samples through dielectric, magnetic and thermal conductivity measurements. In these studies, the transitions were observed at 38, 150, 178, 223 and 250 K. In particular, all these transitions were clearly seen in the magnetocaloric data on pristine BiFeO₃ [60]. Optical spectroscopy is a very sensitive technique to study multiferroic material. It probes electric and magnetic order parameters as well as their coupled effect which gives rise to a new type of quasiparticles called as electromagnons in multiferroics. Hence, infrared spectroscopy is an excellent technique to probe the behavior of magnons and phonons in BiFeO₃ [78-83]. However, till now, to the best of our knowledge, an extensive infrared spectroscopic study

on phonons, magnons and electromagnons of BiFeO₃-based materials has not been carried out across the spin-reorientation transitions (SRTs) to specifically address the issues of magnon-phonon coupling effects.

Thus we have carried out a comprehensive infrared reflectivity measurement on pristine BiFeO₃ ceramic samples at low temperatures to probe the phonon modes across the SRTs and to understand spin-lattice or magnon-phonon interaction. In the low-temperature magnetic measurements, we have noticed two magnetic transitions at 257 and 150 K, which are ascribed as the spin-reorientation related transitions in BiFeO₃. Notably, the low-frequency E(TO1) mode, which is reported earlier as a polar phonon mode of BiFeO₃, is found to be sensitive to the SRTs. Hence, these results give evidence of the presence of phonon-magnon coupling in BiFeO₃.

3.2. Experimental methods

Bismuth ferrite was prepared through the sol-gel route, which was characterized through powder X-ray diffraction (XRD) measurements and the Rietveld refinement of the obtained XRD pattern confirms the single-phasic nature of the sample [60, 97]. For our study, the powder sample was pelletized into disc form having a diameter of 10 mm and thickness equal to 2 mm. The pellet was sintered at 1123 K for 6 hours and the density of the sintered pellet was found to be ~ 90 % of its theoretical density. A small chunk of the sintered pellet weighing about 12 mg was used in our magnetization measurements using Evercool MPMS3 SQUID vibrating sample magnetometer (Quantum Design, USA). The zero-field cooled (ZFC) and field-cooled (FC) magnetization data of BiFeO₃ at magnetic fields of 0.05, 0.1, 0.5, 1, 2, 4, 7 and 10 kOe were collected in the temperature range from 2 to 300 K.

For the IR reflectance measurements, the sintered BiFeO₃ pellet was polished to a mirror finish and then thoroughly cleaned with acetone. Residual stress, if any, on the

surface of the polished side incorporated during the process of polishing, was removed through a heat treatment at 673 K for 3 hours. The IR reflectance experiments were performed in a near normal geometry incidence on the polished surface of the pellet mounted in a reflection setup in Bruker Vertex 80v vacuum spectrometer. The source-beamsplitter-detector combination used for far-infrared (FIR) experiments were: water-cooled mercury source, 6 μm Mylar beamsplitter and liquid-helium cooled silicon bolometer operating at a temperature of 4.2 K. The resolution of the spectra was kept at 0.5 cm^{-1} . The low temperature measurements were carried out in a continuous flow cryostat (Optistat-CFV cryostat, Oxford instruments, UK) from 290 K to 5 K with a temperature stability of better than $\pm 1\text{K}$. Gold coated mirror was used as the standard reference. The $R(\omega)$ spectra of the BiFeO_3 pellet measured at low-temperatures from 290 to 5 K were fitted with the help of REFFIT software [78-81, 106] using the four-parameter model of the complex dielectric function given by the relation:

$$\varepsilon^*(\omega) = \varepsilon_\infty \prod_{k=1}^N \frac{\omega_{LOk}^2 - \omega^2 + i\omega\gamma_{LOk}}{\omega_{TOk}^2 - \omega^2 + i\omega\gamma_{TOk}} \quad (3.1)$$

where, ω_{TOk} and ω_{LOk} , and γ_{TOk} and γ_{LOk} are the frequency and damping factors of the k^{th} transverse and longitudinal optical phonons (TO and LO), respectively. The symbol ε_∞ represents the high-frequency permittivity. Here, the reflectivity, $R(\omega)$ is related to the complex permittivity, $\varepsilon^*(\omega)$, as in the following relation:

$$R(\omega) = \left| \frac{\sqrt{\varepsilon^*(\omega)} - 1}{\sqrt{\varepsilon^*(\omega)} + 1} \right|^2 \quad (3.2)$$

3.3. Results and discussions

3.3.1. Magnetic Studies

In the low-temperature magnetic studies, the zero-field cooled (ZFC) and field cooled (FC) magnetization, $M(T)$ curves of ceramic BiFeO_3 in the temperature range from 300 to 2 K at an applied magnetic field of 0.01, 0.1, and 1 T are shown in Figures 3.1a, 3.1b and 3.1c respectively. At an applied magnetic field of 0.01 T (Figure 3.1a), the magnetization value both in ZFC and FC measurement processes starts increasing upon cooling below room-temperature. This is because of the local clustering of magnetic moments [73, 107] with decreasing temperature. It is noticed that the ZFC and FC $M(T)$ curves start bifurcating at a temperature called ‘irreversible temperature’ (T_{irr}) of ~ 257 K. Earlier, this type of transition in BiFeO_3 had been addressed as a spin-glass-type transition [60, 73]. However, our samples do not show frequency-dependent susceptibility across the transition in case of both as prepared and annealed samples [61], which rules out any spin-glass-type behavior. Therefore, this transition is ascribed as a spin reorientation transition where spins start reorienting in the easy plane of magnetization [111] [60, 69, 73]. In addition, we observe that the magnetization value shoots up below 10 K due to the setting in of weak ferromagnetic ordering at very low temperatures as a result of spin freezing process [60, 97].

At an applied magnetic field of 0.1 T, on the other hand, the magnetization values in ZFC and FC data are found to decrease with lowering of the temperature (see Figure 3.1b) and show splitting at $T_{\text{irr}} \sim 240$ K (inset of Figure 3.1b). In this case also, a sharp increase in the magnetization value is noticed below 10 K due to the onset of weak ferromagnetic nature [60, 97, 98]. However, at an applied magnetic field of 1 T, the ZFC and FC $M(T)$ curves tend to almost merge with each other (see Figure 3.1c). On closer inspection, the $M(T)$ value shows a gradual decrease, with decreasing temperature, down to $T_{\text{irr}}=190$ K

and then increases slowly. Here again, weak ferromagnetic behavior is noticed below 10 K due to the spin freezing process.

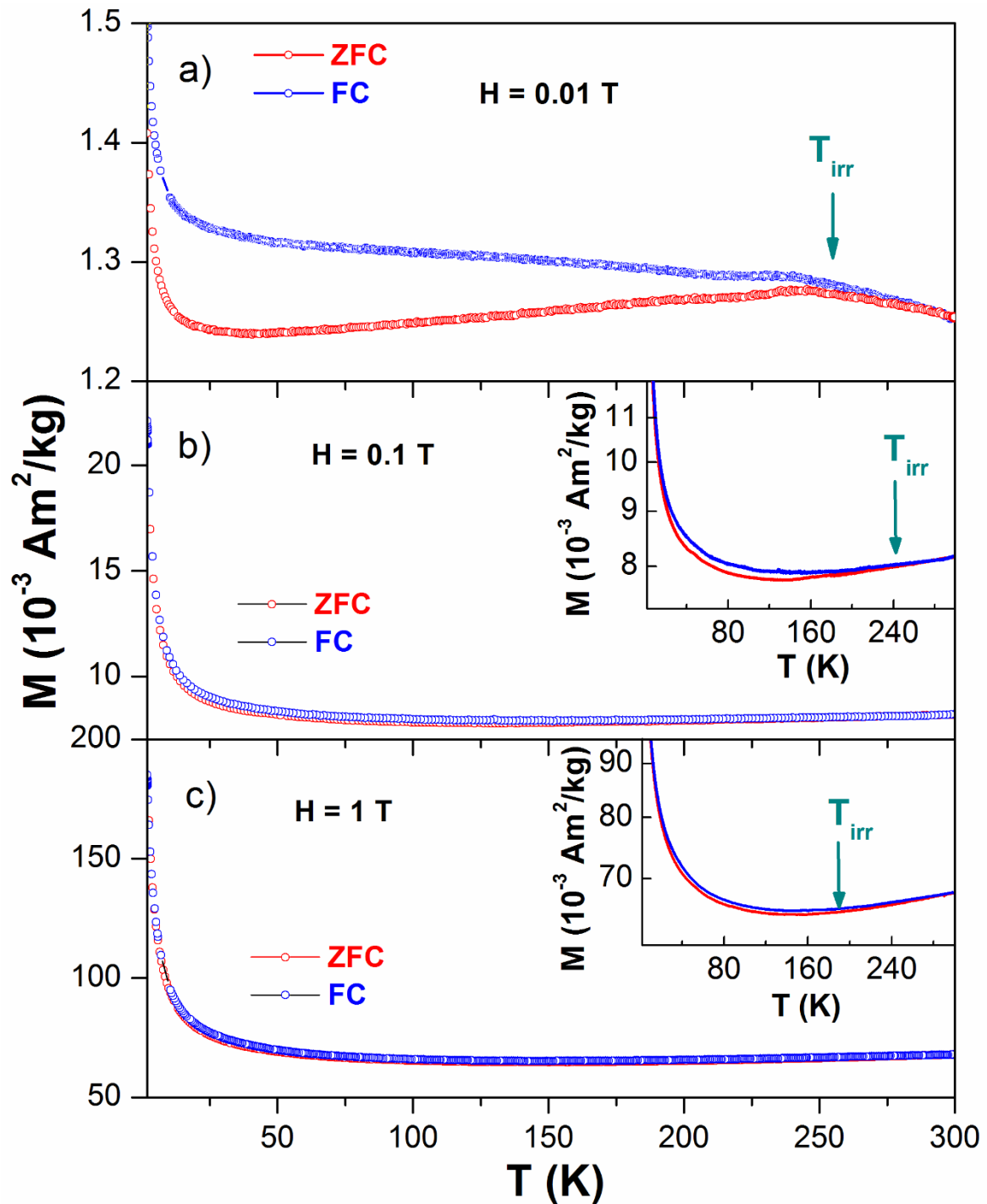


Figure 3.1 Zero-field cooled and field cooled magnetization curves of BiFeO_3 at a magnetic field of (a) 0.01 T, (b) 0.1 T and (c) 1 T. The insets in (b) and (c) represent the semi-log plot of zero field cooled and field cooled magnetization curves.

It is noticed that the value of the irreversible temperature decreases remarkably with increasing magnetic fields. The availability of adequate magnetic energy at a higher applied magnetic fields helps to overcome the energy barrier between the possible equilibrium orientation of spins and the magnetic energy, and thus reduces the irreversible temperature [73]. Further, a power-law fit to the variation of the applied magnetic field as a function of irreversible temperature ($T_{\text{irr}} \sim H^\delta$, δ is the exponent of H) is shown in Figure 3.2. Here, the irreversible temperature $T_{\text{irr}}(H)$ is seen to have a $H^{4/7}$ dependence, which confirms the presence of the Almeida–Thouless *line* (AT-line) in BiFeO₃ ceramics. From the temperature-intercept of the AT-line, the transition temperature for spins' reorientation is found to be at 257 K. Moreover, the critical exponent ($zv=1/\delta$) is found to be 1.75 which is closer to 2. This gives evidence that our system is a mean field system. These findings are similar to the earlier reports on the presence of AT-line in epitaxial BiFeO₃, but these epitaxial systems have spin-glass-type behavior with $zv = 1.5$ and a transition at 140 K [73]. So the bulk form of the BiFeO₃ sample behaves more like a mean field system ($zv = 2$) rather than showing a spin-glass-type behavior ($zv = 1$) as in thin films and hence long range ordering of spins takes place as a result of spin-reorientation in the easy magnetization plane below 250 K in the bulk form of the sample. Therefore, the low-temperature magnetic structure of BiFeO₃ is suggested as a state of coexistence of both long range ordering due to spin reorientation and antiferromagnetic ordering.

We have further probed the spin reorientation transition of BiFeO₃ through the investigation of temperature evolution of the magnetic hysteresis ($M(H)$) loop. The $M(H)$ curves at representative temperatures of 300 and 100 K are shown in the right inset of Figure 3.2. Here, a well-defined M-H loop of the studied sample is seen at 100 K, which points to a weak ferromagnetic behavior, whereas the sample is found to have antiferromagnetic behavior at 300 K. Notably, the obtained coercive field of the studied sample is about ~

0.1033 and 0.0024 T at 100 and 300 K respectively. In the left inset of Figure 3.2 is shown the low-temperature evolution of coercivity (H_c). It is noticed that the value of H_c slowly increases up to the spin-reorientation transition at 150 K, while decreasing the temperature from 300 K [60]. This magnetic behavior is induced at low temperature due to coupled 3d spin of Fe^{3+} ion with antisymmetric super-exchange interaction (Dzyaloshinskii-Moriya interaction). Below 150 K, a sudden increase in the coercivity is seen [60]. Such an enhancement in the magnetic property of BiFeO_3 below 150 K is a result of increase in SIA at low-temperatures [45] through destruction of the spin cycloid. Notably, the H_c value at 2 K is found to be 0.2433 T, which is higher than the value of H_c in single crystal BiFeO_3 [108]. The observed behavior in the magnetic property of our sample is in accordance with that seen in BiFeO_3 -based samples [108-110].

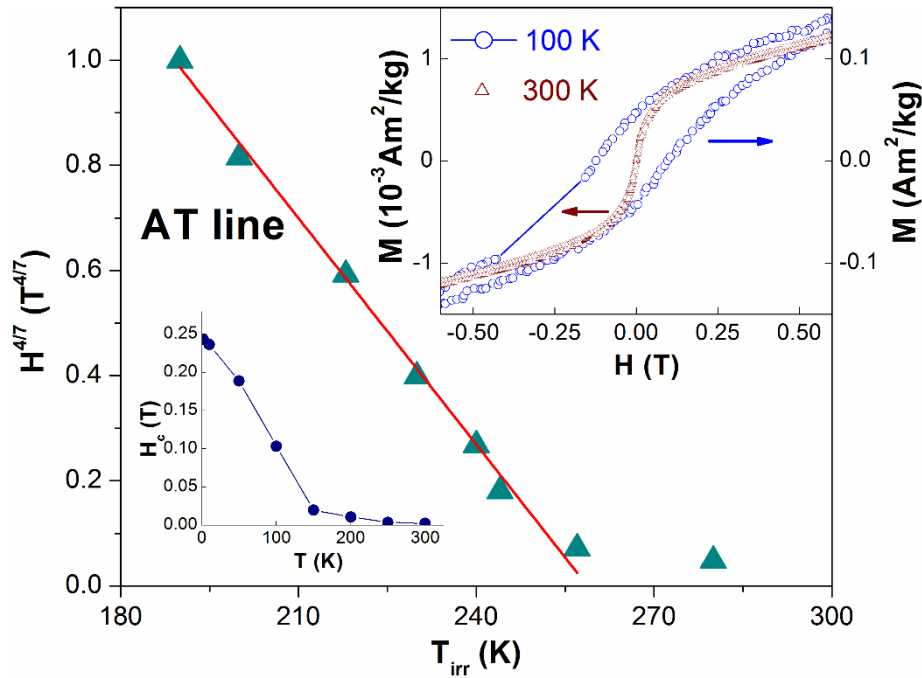


Figure 3.2 $H^{4/7}$ versus T_{irr} plot of BiFeO_3 sample. The fitted straight line (red color) to the magnetic data points is the AT-line. The $M \sim H$ loops at 300 and 100 K are shown in the inset shown in the upper right corner of the figure. The temperature evolution of coercivity is shown in the inset at the lower left corner of the figure.

In summary, two magnetic transitions of BiFeO_3 have been observed: one at 257 K and another at 150 K (see Figures 3.1 and 3.2). More importantly, the temperatures at which

these magnetic transitions occur are found to be closer to the reported SRTs of BiFeO₃ in the literature [60, 70-72]. Further assessment of these findings will be carried out in the next section based on the low-temperature investigation of phonons across the SRTs from infrared reflectivity measurements.

3.3.2. Infrared studies

Infrared reflectance spectra of the pristine BiFeO₃ pellet were recorded at low temperatures to probe the phonon behavior across the SRTs. Representative reflectance spectra at a few selected temperatures from 290 to 5 K in the frequency range 50 to 650 cm⁻¹ are shown in Figure 3.3. Substantial changes in these temperature-dependent spectra are seen due to a strong evolution of phonons with temperature. In addition progressive damping of phonons with increasing temperature leads to broadening and overlapping of the modes. In spite of this, all the 13 phonon modes (4A₁ and 9E), allowed by the rhombohedral crystal symmetry in the R3c space group, are clearly apparent at room temperature, which indicates the high-quality of our sample.

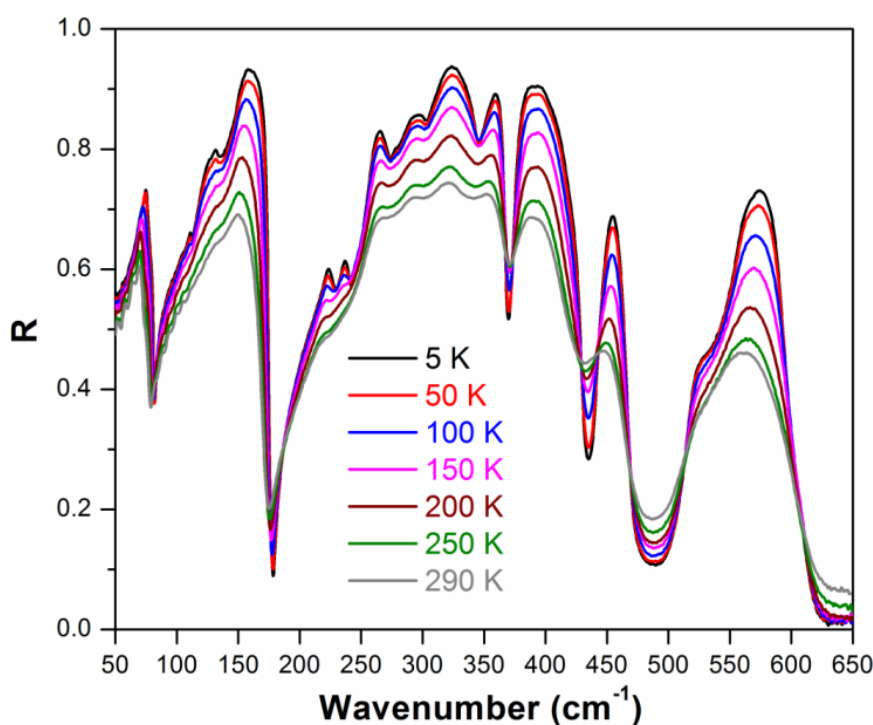


Figure 3.3 Reflectance spectra of BiFeO₃ at a few selected temperatures.

As already mentioned in section 3.2, these reflectance spectra were fitted to the four-parameter model (eq. 3.2) to extract the mode parameters. The obtained mode frequencies from the fitting of the room temperature spectrum match very well with the frequencies reported for a single crystal sample by Lobo et al. The observed 13 modes obtained from the fit are found to be at 547, 520, 442, 372, 356, 319, 285, 262, 229, 228, 148, 127 and 72 cm^{-1} . These modes are assigned with their symmetries as $A_1(\text{TO4})$, $E(\text{TO9})$, $E(\text{TO8})$, $E(\text{TO7})$, $E(\text{TO6})$, $A_1(\text{TO3})$, $E(\text{TO5})$, $E(\text{TO4})$, $E(\text{TO3})$, $A_1(\text{TO2})$, $A_1(\text{TO1})$, $E(\text{TO2})$ and $E(\text{TO1})$, respectively [52]. Figure 3.4 shows 290 and 10 K reflectance spectra of BiFeO_3 along with their fits, with all the 13 modes shown, marked with their respective symmetries. Most importantly, the observed mode parameters for the LO and TO modes at 290 and 10 K are consistent with those reported in the literature (see Table 3.1) [52, 53].

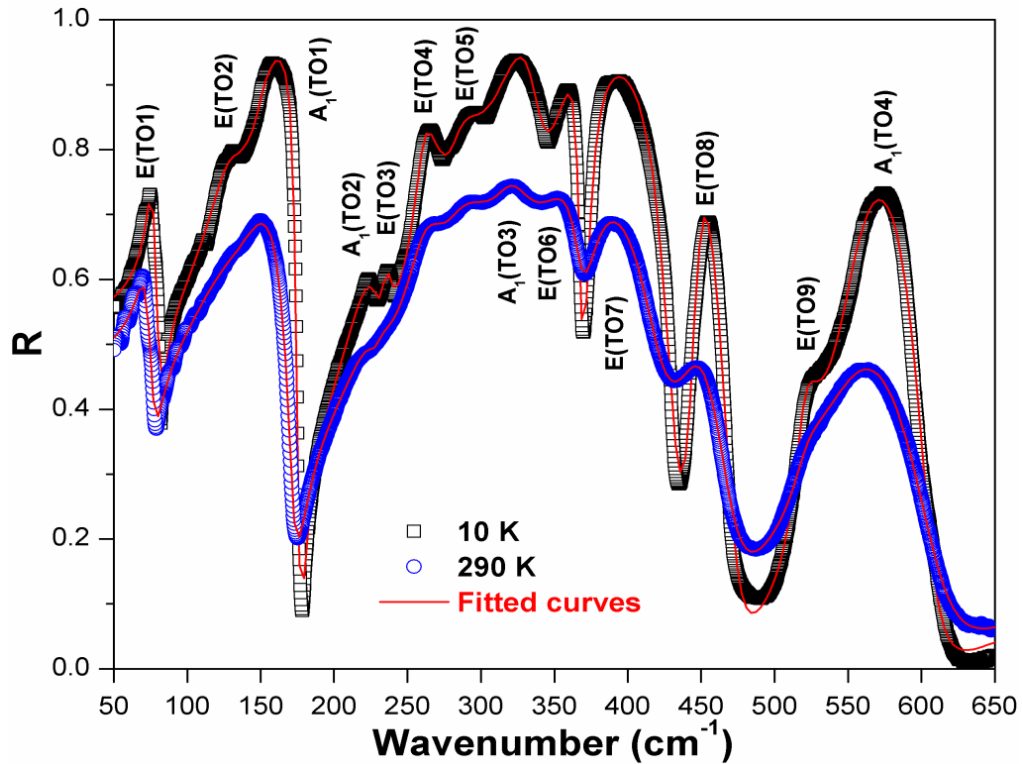


Figure 3.4 Reflectance spectra of BiFeO_3 at 300 and 100 K. Red solid lines are the spectral fits.

Table 3.1 The obtained mode parameters of bulk BiFeO_3 using the four-parameter model as described in Equations (3.1) and (3.2).

S. No	Symmetry	Mode parameters at 290 K				Mode parameters at 10 K			
		ω_{TO} (cm^{-1})	γ_{TO} (cm^{-1})	ω_{LO} (cm^{-1})	γ_{LO} (cm^{-1})	ω_{TO} (cm^{-1})	γ_{TO} (cm^{-1})	ω_{LO} (cm^{-1})	γ_{LO} (cm^{-1})
1	E	72.0	9.6	76.6	8.7	75.0	5.2	80.8	5.4
2	E	126.6	50.5	129.0	94.1	127.0	17.3	141.3	64.6
3	A_1	147.9	29.6	171.6	11.0	148.7	17.9	175.2	3.0
4	A_1	228.0	25.6	228.3	10.9	223.9	20.6	234.4	7.7
5	E	228.8	12.8	233.0	33.6	235.2	5.4	235.9	28.8
6	E	262.4	20.0	273.7	45.6	260.7	7.4	279.2	31.0
7	E	284.9	29.3	285.5	99.6	283.3	18.0	285.5	99.6
8	A_1	318.7	29.4	324.5	35.1	316.1	43.5	339.1	26.0
9	E	355.7	70.2	367.4	16.3	349.9	35.4	367.9	5.7
10	E	371.9	24.4	420.7	41.7	373.2	9.8	429.1	19.2
11	E	442.3	39.0	465.3	33.6	445.0	10.6	464.3	15.9
12	E	520.3	23.1	520.3	29.4	519.3	12.1	520.1	29.4
13	A_1	546.8	60.9	599.6	48.6	548.7	33.2	592.8	16.5

Further, the phonon modes of BiFeO_3 can be broadly categorized into three groups in the frequency ranges of 400-650, 200-400, and 100-200 cm^{-1} based on a comparison of vibrational aspects of other related perovskite-type materials such as LaTiO_3 and BaTiO_3 , etc. [82, 111-113]. These three groups are due to FeO_6 octahedral stretching and bending modes and external modes related to the movement of FeO_6 octahedra against Bi-sublattice, respectively [82]. Besides, the low-frequency phonon modes that are in the vicinity of the magnon modes will be expected to be influenced if the sample exhibits any spin-lattice (magnon-phonon) interaction. In particular, the $E(\text{TO1})$ mode is a polar or ferroelectric mode for rhombohedral BiFeO_3 [72, 83]. This mode is suggested to be sensitive to magnetic ordering [72]. Therefore, the evolution of this mode is followed at low temperature. The temperature evolution of the frequency of this mode is fitted with a cubic anharmonicity model (see Figure 3.5). It is noticed that the temperature evolution of the mode frequency follows a regular anharmonic behavior below 160 K and then starts deviating above SRT. Thus a deviation of frequency from the anharmonic fit is clearly seen above SRT at 150 K. In addition, we observe an anomaly at ~ 250 K in the temperature evolution of the mode

frequency, which is close to the SRT at 257 K seen in our magnetic studies. Also plotted in Figure 3.5 is the linewidth variation with temperature which is seen to exhibit a change in slope near the SRTs. In addition to this, an anomalous behavior in the linewidth is seen at ~ 20 K (shown by an arrow in Figure 3.5), which is close to a dielectric anomaly reported earlier on our samples [61, 64]. Thus, it can be said that this mode is sensitive to SRTs on account of the presence of spin-phonon or magnon-phonon interaction. The fact that this is a polar mode and that it is seen to be sensitive to the SRTs, gives evidence of the existence of magnetoelectric coupling in BiFeO_3 .

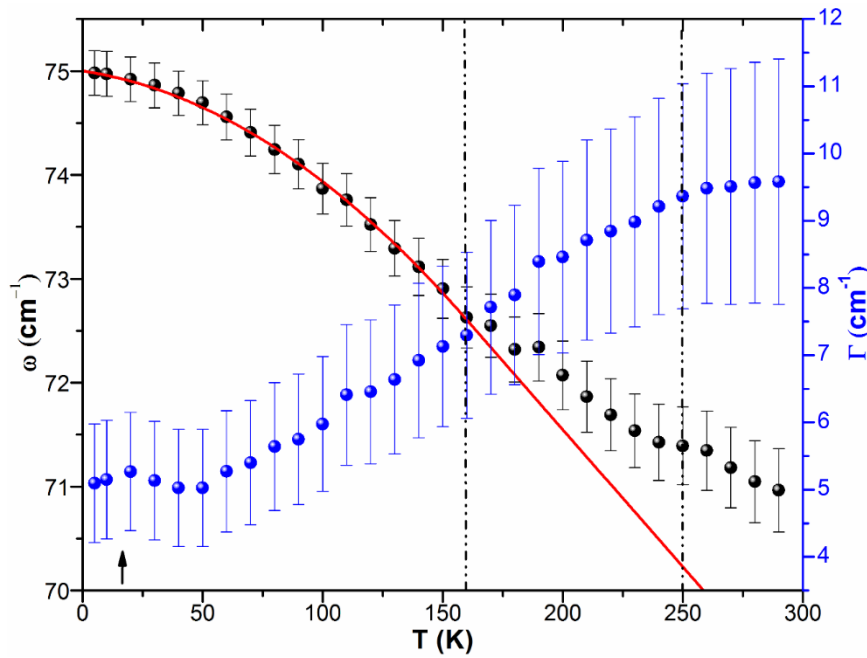


Figure 3.5 Temperature evolution of frequency and linewidth of $E(\text{TO1})$ mode. The red curve is the fit to cubic anharmonic model. The arrow at ~ 20 K points to the dielectric anomaly.

In what follows, we shall discuss the low temperature behavior of the remaining phonon modes with special focus on their behavior near SRTs. To make things easier to comprehend, these modes are considered in separate groups, with each group displaying similar low temperature behavior. Accordingly, $E(\text{TO7})$ and $E(\text{TO8})$ form group I, $E(\text{TO2})$, $A_1(\text{TO1})$, $E(\text{TO4})$, $E(\text{TO9})$ and $A_1(\text{TO4})$ form group II, and $A_1(\text{TO2})$, $E(\text{TO3})$, $E(\text{TO5})$, $A_1(\text{TO3})$ and $E(\text{TO6})$ form group III.

In Figure 3.6, mode frequency variations of E(TO7) and E(TO8) with temperature are shown. These mode frequencies show a gradual increase with lowering of temperature and their temperature evolutions have been fitted a cubic anharmonic model. From this, these two modes are found to have regular anharmonic behavior with decreasing temperature except for a small anomaly at ~ 20 K in the case of E(TO8) mode which may be probably due to the dielectric anomaly observed at this temperature.

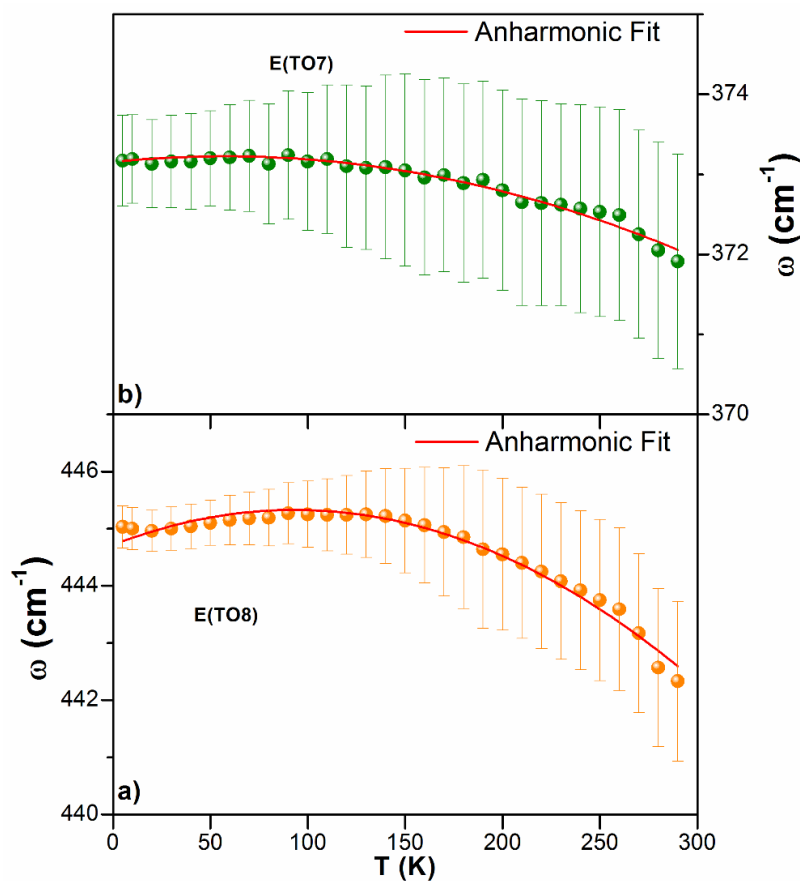


Figure 3.6 Mode frequency of (a) E(TO7) and (b) E(TO8) with respect to temperature. The solid curves show the anharmonic fit to the data.

In Figure 3.7, vibrational frequencies of phonon modes listed in group II are plotted as a function of temperature. All these modes show almost similar behavior, where the mode frequencies are found to gradually decrease with decreasing temperature until 210 K, followed by an increasing trend up to 5 K. Here, the observed trend in frequency until 210 K is possibly due to rhombohedral elastic distortion with decreasing temperature [83, 114]

followed by the regular hardening of phonons at low temperature up to 5 K. Furthermore, an anomalous behavior is clearly seen at 210 K which is shown by the dotted line in Figure 3.7. This anomalous behavior is ascribed to the magneto-elastic effect observed at that temperature [60, 115].

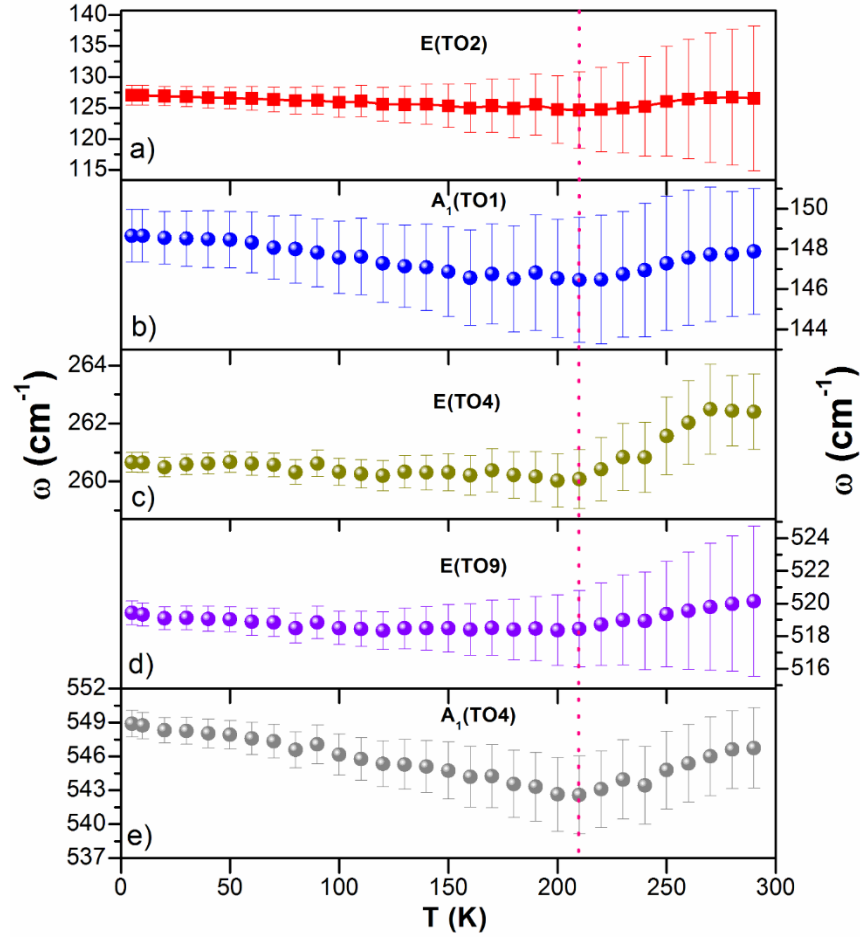


Figure 3.7 Temperature evolution of (a) $E(TO2)$, (b) $A_1(TO1)$, (c) $E(TO4)$, (d) $E(TO9)$ and (e) $A_1(TO4)$ mode frequencies.

Next, group III phonon modes are followed with decreasing temperature and Figure 3.8 displays the temperature evolution of their vibrational frequencies. The $E(TO6)$ mode shows a decreasing trend in frequency with lowering of the temperature all the way down to 5 K (Figure 3.8a), whereas, $E(TO3)$ and $E(TO5)$ show concomitant temperature evolution with opposite shifts in frequency at any given temperature. In a similar manner, the temperature evolution of $A_1(TO2)$ mode frequency is related to that of $A_1(TO3)$ mode frequency. This behavior is almost similar to the concomitant temperature evolution of long

Fe-O versus short Fe-O bond lengths observed by Palewicz et al (Figure 6 in reference [114]). Also, the observed hump at around 80 K (shown by the dotted line in Figure 3.8) exactly matches with the hump seen in the temperature evolution of both short and long Fe-O bond distances [114]. Therefore temperature evolution of these modes is mainly governed by local structural changes occurring at low temperature. Further, the anomalies observed at 20 and 210 K could be ascribed to the dielectric anomaly [61, 64] and the magneto-elastic effect [60, 115], respectively.

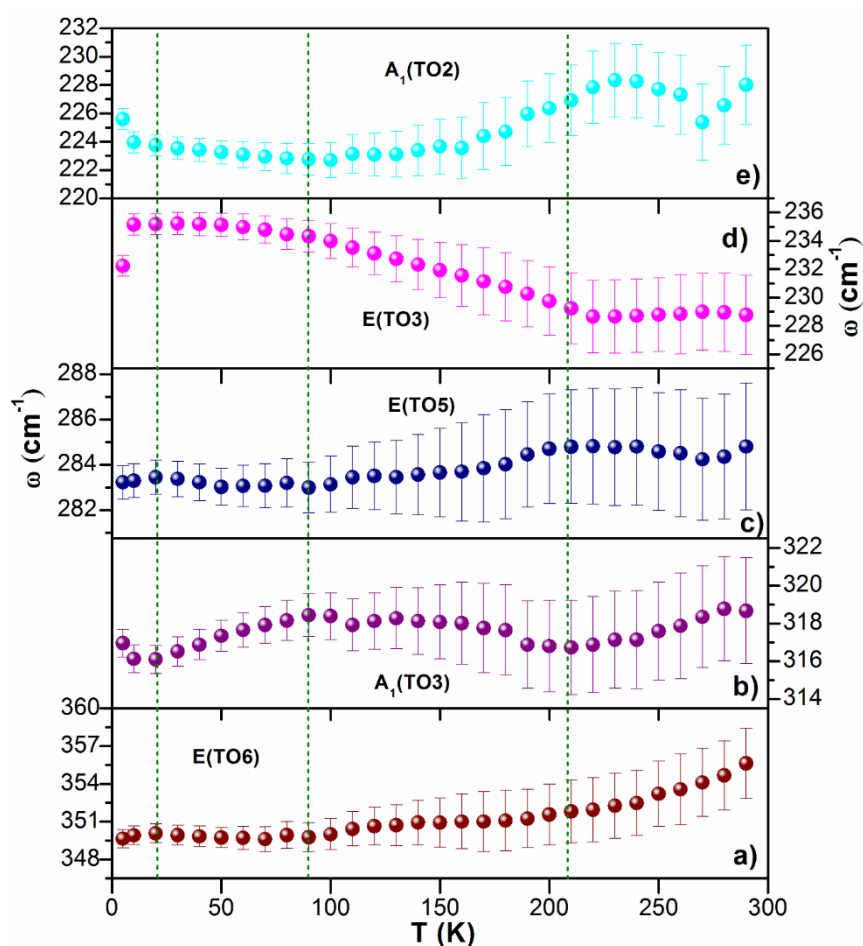


Figure 3.8 Temperature evolution of frequencies of (a) $A_1(TO2)$, (b) $E(TO3)$, (c) $E(TO5)$, (d) $A_1(TO2)$ and (e) $E(TO6)$ modes.

Overall, the temperature evolution of the phonon modes suggests that magnon-phonon and magnetoelectric couplings are prevalent in bismuth ferrite. It should be noted here that the magnon-phonon coupling effect results in the observation of magneto-dielectric resonances (seen in the susceptibility spectra) of BiFeO_3 [56, 62-64, 116].

Another interesting aspect of this low temperature study is the birth of a new absorption feature at $\sim 111 \text{ cm}^{-1}$ (shown by an arrow in Figure 3.9a) in the reflectance spectra of BiFeO_3 , below 160 K. This new feature is much more clearly evident in the extinction coefficient spectra, $k(\omega)$ (see the arrow in the Figure 3.9b) deduced from the corresponding reflectance spectra through a Kramers-Kronig Transformation (KKT). This is similar to the new magnetic excitation seen in the case of the YbFeO_3 compound across its spin-reorientation transition [86]. Moreover, this mode frequency of $\sim 111 \text{ cm}^{-1}$ is almost double the frequency of spin excitation observed at $\sim 56 \text{ cm}^{-1}$ and thus, this mode is assigned as a two-magnon mode of BiFeO_3 . In addition to this, one more two-magnon mode is observed at $\sim 106 \text{ cm}^{-1}$ (shown by a second arrow in Figure 3.9b), which is also an overtone of the spin-wave excitation observed at $\sim 53 \text{ cm}^{-1}$. These spin-excitations are reported as electromagnons (electric dipole active magnon mode) of BiFeO_3 [81, 117], which are basically the quasi-particles in multiferroic materials. Based on these considerations, we suggest that these two-magnon modes are also electromagnons.

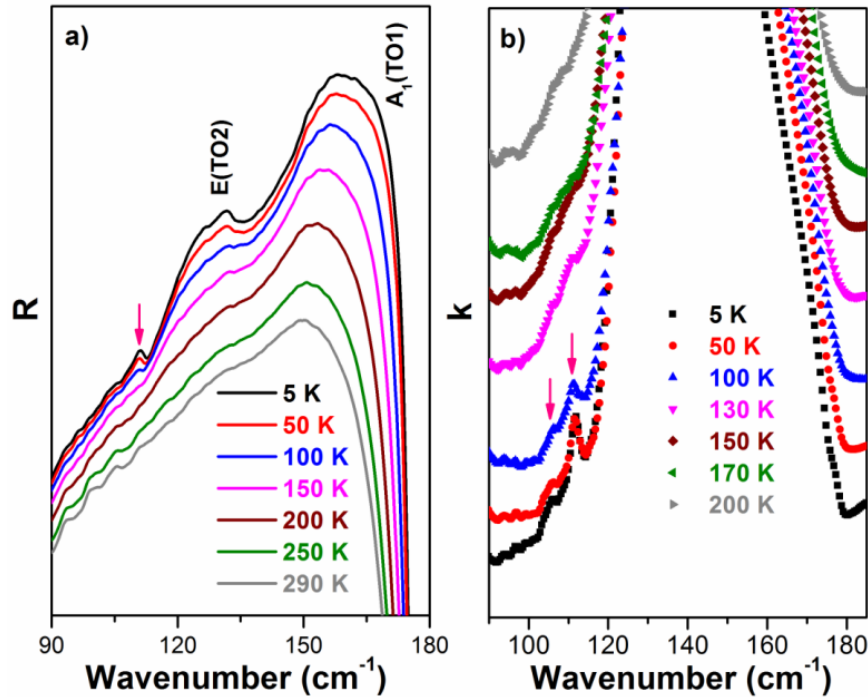


Figure 3.9 (a) Reflectance and (b) the corresponding extinction coefficient spectra of BiFeO_3 at a few selected temperatures.

We have further followed the behavior of the mode parameters of 111 cm^{-1} two-magnon mode with temperature (Figure 3.10). As the temperature is lowered from 300 K, this two-magnon mode starts manifesting below 160 K and gains in intensity with decreasing temperature followed by a turnaround behavior at a $\sim 20\text{ K}$. A blue shift in the mode frequency and a decrease in the linewidth are also observed while going down the temperature (see Figure 3.10 a). Here, the turnaround behavior in I/I_{max} at 20 K is due to a dielectric anomaly [61, 64], observed in this material. This implies that this two-magnon mode is sensitive to electric order, giving further credence to the fact that this mode is an electromagnon of BiFeO_3 . Additionally, the increase in I/I_{max} with decreasing temperature points to an increase in magnetoelectric coupling. The temperature at which this mode takes birth viz., 160 K is close to the SRT at 150 K. It has been earlier reported that multimagnon modes can emerge due to modification in spin structure [118]. This is experimentally seen in the present case. Thus, the emergence of two-magnon mode is a result of a modification in the noncollinear spin structure brought about by SRT at 150 K.

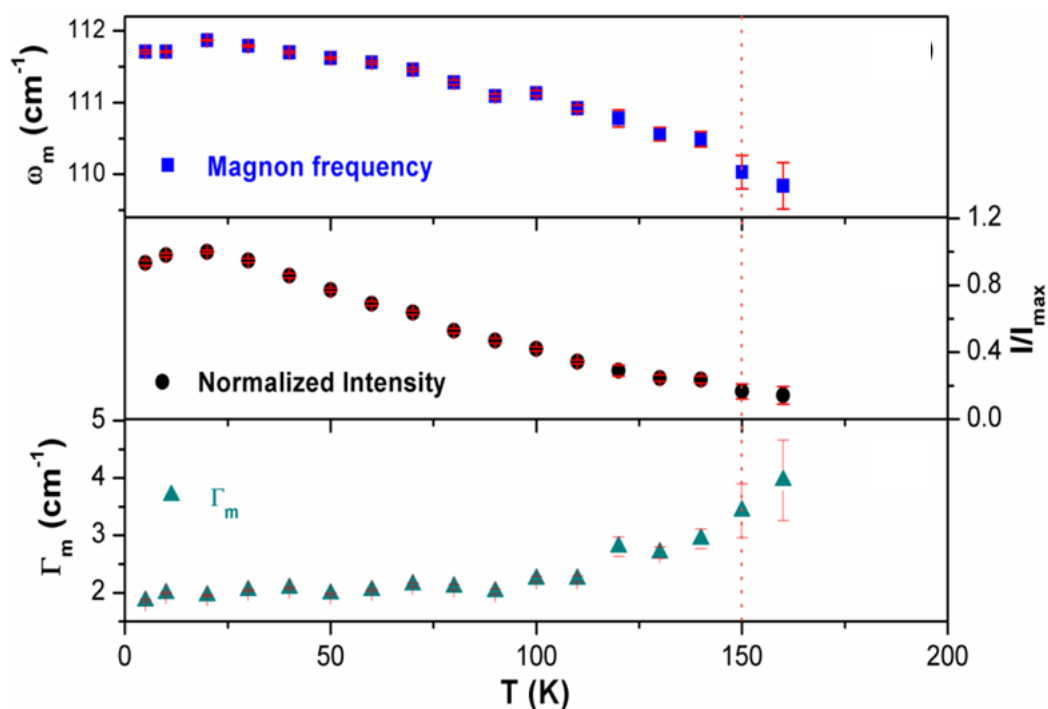


Figure 3.10 Temperature evolution of the lineshape parameters of the new 111 cm^{-1} two-magnon mode.

The overall summary of this study points to the presence of magnon-phonon coupling effect as well as the magnetoelectric coupling in BiFeO₃ ceramics. The magnetoelectric coupling is suggested to have an increased strength at low temperatures. It is observed that the phonon modes are largely influenced by changes in the local structure occurring at low temperature.

3.4. Conclusions

We have performed low-temperature magnetic measurements on BiFeO₃ ceramic sample, which show two magnetic transitions at 257 and 150 K corresponding to spin-reorientations. Further, an extensive infrared spectroscopic study of phonons of BiFeO₃ at low temperatures has been carried out. All the 13 modes allowed by the rhombohedral symmetry in the R3c space group are observed in the reflectivity spectra. The temperature evolution of all these 13 modes frequencies has been followed. It is noticed that the low-energy E(TO1) phonon mode, in particular, is sensitive to the spin reorientation transitions. The magnetoeleastic effect that is known to occur at 210 K is seen to effect an anomalous behavior in many of these phonon modes. Moreover, two new absorption features are observed at 111 and 106 cm⁻¹ below 160 K. These are assigned as two-magnon modes on account of their being overtones of spin excitations that occur at lower frequencies. The main reason behind the emergence of two-magnon mode is the modification in the noncollinear spin structure brought about by the spin-reorientation transitions. Based on the sensitivity of their mode parameters to the prevalent electric order in the sample, these modes have been suggested to be electromagnons.

Chapter 4

Investigation of spin-wave excitations in BiFeO₃ at low-temperature

In this chapter, investigations of spin-wave excitations in BiFeO₃ at low temperature are carried out through Far-infrared reflectivity measurements in order to explore the cause of the improved magnetic and magneto-electric behavior of BiFeO₃ observed in the previous chapter. The findings from the infrared data are complemented by a low temperature EPR study to get additional insight into the nature of spin dynamics in system.

4.1. Introduction

As already mentioned in Chapter 1, Section 1.2.3, the spin structure of BiFeO₃ gets stabilized into antiferromagnetic spin arrangement modulated with an incommensurate spiral array of spins over a wavelength of 62 nm [119], which is known as spin cycloid. This spin cycloid generates a series of two types of magnetic excitations [56] known cyclons (Φ) and extracyclons (Ψ), which are in-plane and out-of-plane modes to the cycloidal plane, respectively. These cyclons and extracyclons are collectively known as spin wave excitations (SWEs) and have been studied through terahertz [46, 54, 81], far infrared and millimeter [58], and Raman [55] spectroscopic experiments, although each of these techniques has different selection rules. Prior investigations of these SWEs have attempted to gain an understanding of the underlying mechanism of multiferroicity in bismuth ferrite both experimentally and theoretically.

de Sousa and Moore [56] theoretically predicted, via the Ginsburg-Landau model, by assuming spin cycloid as purely harmonic, that a long wavelength electromagnetic radiation couples with magnon mode at a multiple of cycloid wave vector leading to a series of SW resonances in the spectrum. From this calculation, the energy of Φ and Ψ -modes are

given by the equations $E_c = m\varepsilon_c$ and $E_{exc} = (m^2 + 1)^{1/2}\varepsilon_c$, respectively. Here m is an integer index and ε_c is the cyclon energy. On the other hand, Fishman et al [57] showed that the higher harmonics of the spin cycloid generated via single-ion anisotropy split each of these Φ and Ψ -modes, which are labeled as $\Phi_n^{(1,2)}$ and $\Psi_n^{(1,2)}$, respectively. Another important aspect is the anharmonicity of the spin cycloid, which strongly influences the intensities of SWEs and the selection rules [49, 56]. In fact, this anharmonicity is found to increase at low temperature [36-42].

In the previous chapter, the low temperature magnetic studies on BiFeO₃ revealed two spin reorientation transitions at 257 and 150 K, where Fe³⁺ spin starts reorienting out of the easy plane of magnetization $\langle 111 \rangle_{pc}$. A significant enhancement in magnetic behavior is observed below the spin reorientation transition at 150 K. Moreover, emergence of new two-magnon modes is observed below 150 K. Additionally, the phonon modes are found to have anomalous behavior across the several magnetic transitions of BiFeO₃. These results point to the presence of a complex magnetic structure in BiFeO₃, which has not been completely understood yet. This prompted us to examine the magnetic behavior of BiFeO₃ through a set of comprehensive low-temperature investigations of the SWEs via infrared and electron paramagnetic resonance (EPR) spectroscopic techniques, and these studies form the subject matter of this chapter. We notice from the infrared studies that the SWE modes split across the spin reorientation transition at 250 K. Moreover, these SWE modes are also found to get suppressed at low-temperature. On the other hand, EPR results give information about ‘degree of spin canting’ across the spin reorientation transitions.

4.2. Experimental

The same polished pellet used for our work in chapter 3 has been used for low-frequency far-infrared reflectance measurements. A water cooled Hg-source, 6 and 50 micron mylar beamsplitters and liquid-helium cooled silicon bolometer (operating

temperature is at 4.2 K) detector were used for the measurements. The reflectance spectra were recorded at near normal incidence with a resolution of 0.5 cm^{-1} . The low temperature $R(\omega)$ spectra were obtained in a continuous flow cryostat (Optistat-CFV cryostat, Oxford instruments, UK) in the temperature range from 290 K to 5 K. Here, the low temperature sample spectra were referenced with the gold mirror spectra at the corresponding temperatures.

The real and imaginary parts of complex reflectivity, $r^* = re^{i\varphi(\omega)}$, where r is the reflected amplitude ($R = |r|^2$) and $\varphi(\omega)$ is the phase change due reflection, are related via Kramers-Kronig Transformation (KKT) [120]. The imaginary part of complex reflected amplitude, $\varphi(\omega)$, is given by

$$\varphi(\omega) = -\frac{\omega}{\pi} \int \frac{\ln R(\omega') - \ln R(\omega)}{\omega'^2 - \omega^2} d\omega', \quad 4.1$$

where $\omega=2\pi\nu$ is the angular frequency. With the knowledge of $R(\omega)$ and $\varphi(\omega)$, we can calculate the real and imaginary part of complex refractive index, $N(\omega) = n(\omega) + ik(\omega)$, using Fresnel equations [121] as

$$n(\omega) = \frac{1 - R(\omega)}{1 + R(\omega) - 2\sqrt{R(\omega)\cos\varphi(\omega)}}, \quad 4.2$$

$$k(\omega) = \frac{2\sqrt{R(\omega)\sin\varphi(\omega)}}{1 + R(\omega) - 2\sqrt{R(\omega)\cos\varphi(\omega)}}, \quad 4.3$$

Here, $R(\omega)$ is related to optical constants $n(\omega)$ and $k(\omega)$ via the relation given below.

$$R(\omega) = |r|^2 = \frac{(n-1)^2 + k^2}{(n+1)^2 + k^2}, \quad 4.4$$

As the complex refractive index relates to the complex dielectric ($\varepsilon^* = \varepsilon' + i\varepsilon''$) and permeability ($\mu^* = \mu' + i\mu''$) function through the relation $N(\omega) = \sqrt{\mu^* \varepsilon^*}$, $k(\omega)$ -spectrum represents the losses corresponding to dielectric (phonon), susceptibility (magnon) or magnetodielectric (coupled electric and magnetic dipole) related transitions.

For the electron paramagnetic resonance measurements, powders sample was taken in a quartz tube and placed in a resonant cavity at the center of the electromagnet. The EPR spectra of the sample were recorded in a Bruker EMX X-band EPR spectrometer with the following set of parameters: the range of magnetic field from 0 to 6500 mT, while the frequency of magnetic field was kept at ~ 9.43 GHz. Optimization of microwave power, modulation amplitude and time constant was ensured. Low temperature EPR spectra (300-80 K) were recorded by using a liquid nitrogen cryostat.

4.3. Results and discussion

4.3.1. Infrared study

Figures 4.1a and 4.1b display the reflectance spectra, $R(\omega)$ and the corresponding extinction coefficient spectra, $k(\omega)$, respectively, at a few selected temperatures in the frequency range from 27-650 cm^{-1} . All the thirteen infrared active modes allowed by the rhombohedral symmetry of the R3c space group of BiFeO_3 are clearly observed in both the $R(\omega)$ and $k(\omega)$ spectra. The mode assignment of these phonon vibrations are shown in the Figure 4.1b. The behavior of this phonon spectrum at low temperature has already been discussed in the previous chapter. Apart from the phononic part, a series of absorption features are clearly seen in the low-frequency region of the $R(\omega)$ and $k(\omega)$ -spectra (shown by rectangular box in Figures 4.1a and 4.b). These low-frequency absorption features are

related to the magnetodielectric resonances (coupled electric and magnetic dipole related transitions), which are known as SWEs of BiFeO₃. These SW modes have been analyzed as a function of temperature to understand their behavior, in particular, across the SRTs. Since the $k(\omega)$ -spectrum represents the losses corresponding to coupled electric and magnetic dipole related transitions, it is considered for the analysis of SWEs in BiFeO₃.

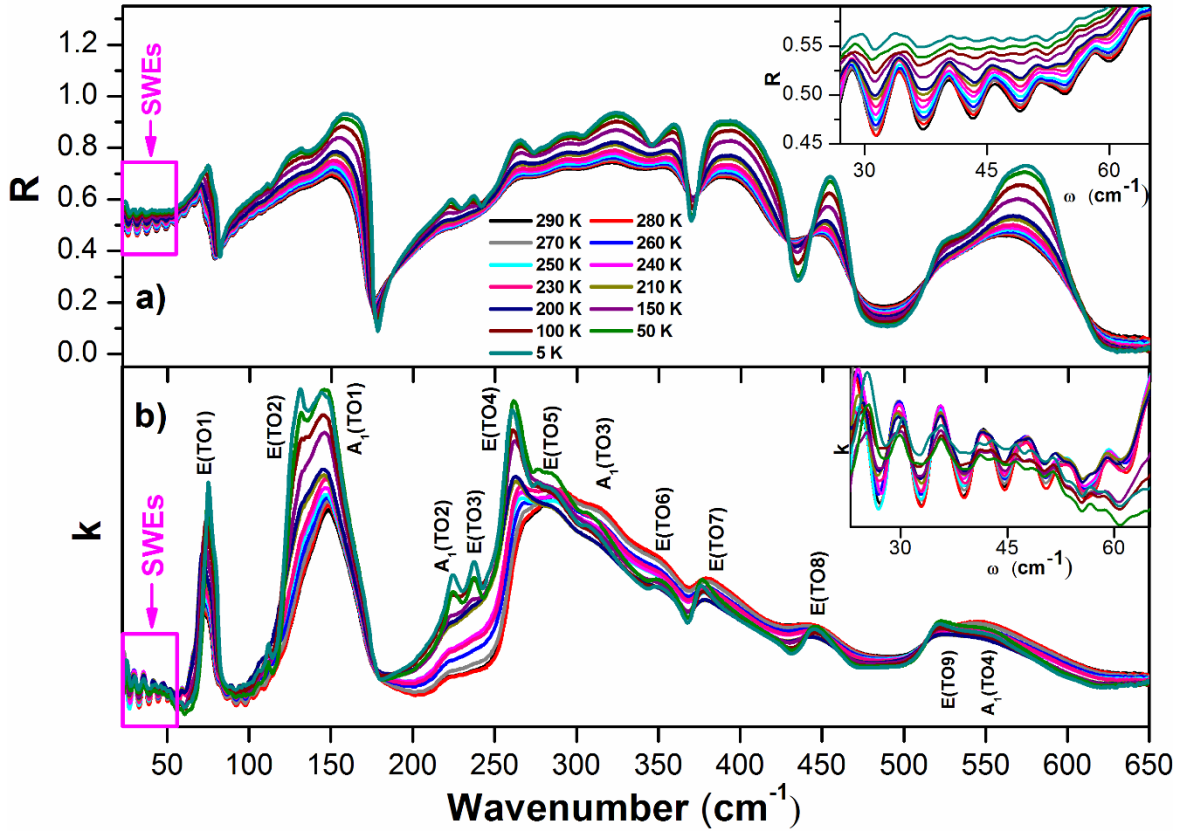


Figure 4.1 (a) Reflectance and (b) the corresponding extinction coefficient spectra of BiFeO₃ at a few selected temperatures. The insets show the SWEs on expanded scale.

4.3.1.1. Low temperature changes in SW mode frequency

Figure 4.2a displays the very low frequency part of the $k(\omega)$ -spectrum of the studied sample close to room temperature highlighting the features of six SWEs. We have analyzed these SWEs by a non-linear curve fitting procedure using Gaussian lineshapes to the $k(\omega)$ -spectrum. The SW mode frequencies so obtained are 29.9, 35.6, 41.7, 47.5, 53.2 and 59.2

cm^{-1} , which have been assigned to their corresponding cyclon (Φ) and extracyclon (Ψ) modes as $\Phi_3^{(1,2)}$, $\Psi_2^{(1,2)}$, $\Phi_3^{(1,2)}$, $\Psi_3^{(1,2)}$, $\Phi_4^{(1,2)}$ and $\Psi_4^{(1,2)}$, respectively (see assignment of the SWEs in Figure 4.2a) based on the reported literature [57]. The obtained mode frequencies of these SWEs are fitted to cyclon and extracyclon energy relations as given by the equations $E_c = m\varepsilon_c$ and $E_{exc} = (m^2 + 1)^{1/2}\varepsilon_c$, respectively (see Figure 4.2b), where m is the index and ε_c , the cyclon energy. From these fits, we obtain two distinct values of ε_c , which are found to be at a frequency of 14.8 ± 0.4 and $13.4 \pm 0.4 \text{ cm}^{-1}$ from the fits of cyclon and extracyclon energy relations, respectively. This means that the modes Ψ_0 and Φ_1 have distinct frequencies, possibly due to lifting of the degeneracy brought about by SIA and a tilt of the cycloid. Here, the deduced mode frequency of Ψ_0 is well matched with the reported value from the literature [57].

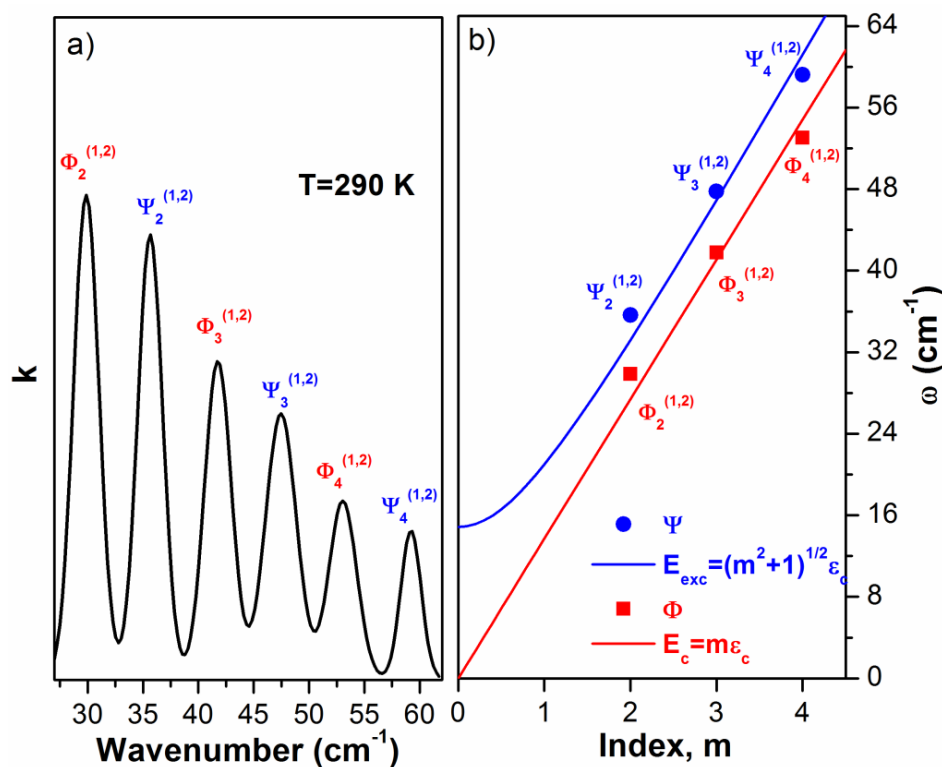


Figure 4.2 (a) Extinction coefficient spectra of BiFeO_3 at 290 K and (b) cyclon and extracyclon energy fits to the obtained mode frequencies of cyclons and extracyclons, respectively.

Figure 4.3 displays the multipoint background subtracted $k(\omega)$ -spectra at a few selected temperatures between 290 to 5 K in the frequency range of 27 to 62 cm^{-1} . The SWE modes are clearly observed in the magnonic part of the $k(\omega)$ -spectra at all temperatures. However, there are significant changes in the SWE modes with lowering of the temperature. For one, there is a substantial decrease in the intensity of SWE modes while going down the temperature. Additionally, all the resonance features show a splitting below 260 K.

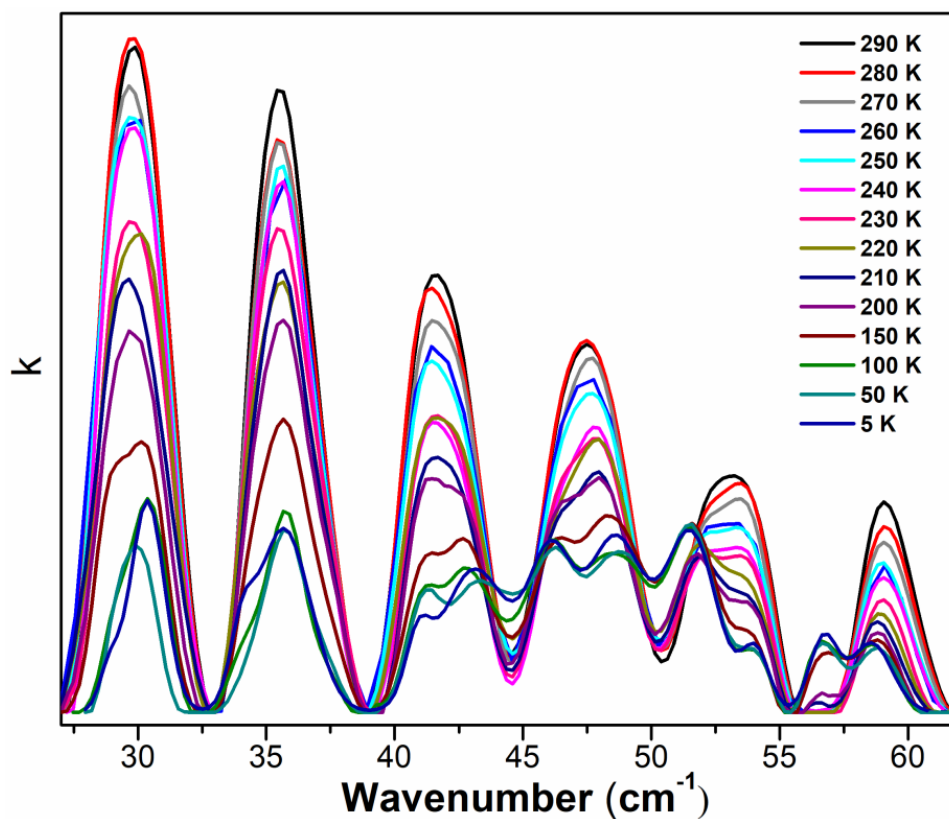


Figure 4.3 The extinction coefficient spectra of BiFeO_3 at a few selected temperatures.

Figure 4.4 shows the variations of mode frequencies of these SWEs with temperature. It is observed that these mode frequency of SWEs show slight change up to 260 K while going down the temperature (see Figure 4.4). Interestingly, it is noticed from Figure 4.4 that there is an increase in number of SWE modes across the SRT at 250 K. This type of increase in number of the SWE modes in BiFeO_3 across the SRTs has not been

reported so far. At first glance, one could probably be tempted to conjecture that the increase in number of SWEs is related to the presence of an additional spin cycloid along the $\langle 100 \rangle_{pc}$ direction as suggested from the theoretical studies by Xu et al. [122]. However, we discard this argument as the features related to this additional spin cycloid have not been observed at room temperature itself. Instead, we attribute this increase in the number of SWEs close to the spin reorientation transition at 250 K to the complete removal of degeneracy of the SW modes brought about by an increase in single ion anisotropy [57] possibly generated through reorientation of spins i.e. the canting of magnetic spins away from the c-axis towards the a-axis by a change in the Fe-O-Fe angle of BiFeO₃ [123]. Further support to this argument of ours comes from the sharing of intensity of the parent SWE modes among their daughter modes, which will be discussed later in this section.

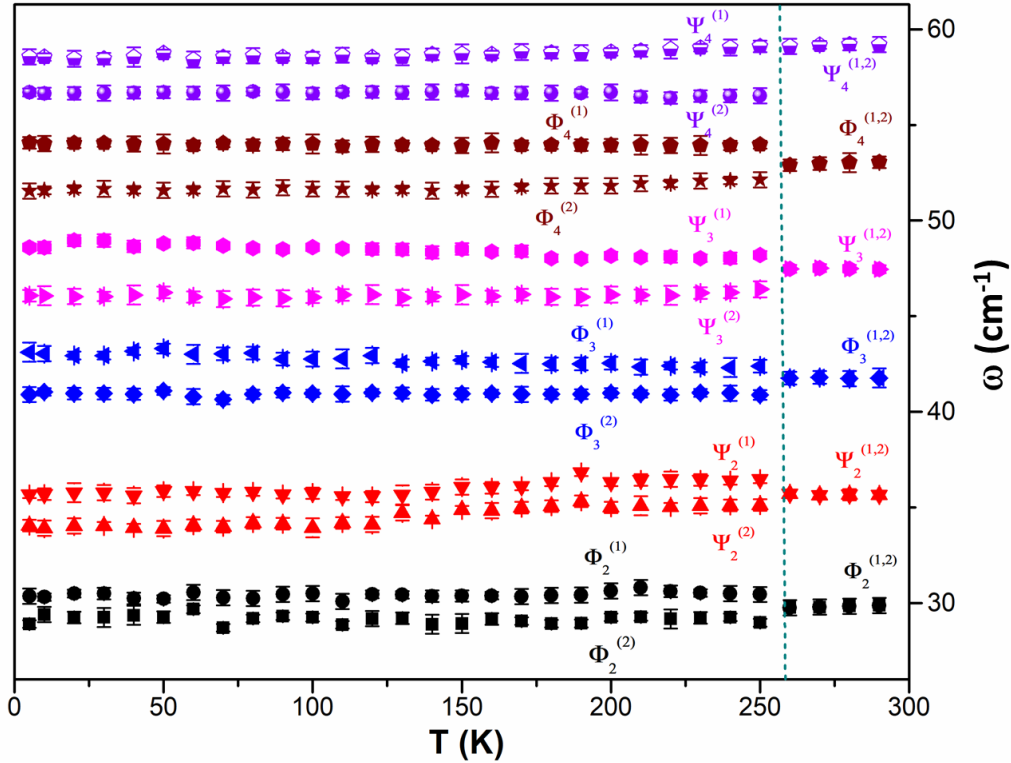


Figure 4.4 SW mode frequencies as a function of temperature.

At 250 K, the splitting energies of the SWEs $\Psi_4^{(1,2)}$, $\Phi_4^{(1,2)}$, $\Psi_3^{(1,2)}$, $\Phi_3^{(1,2)}$, $\Psi_2^{(1,2)}$ and $\Phi_2^{(1,2)}$ are estimated to be 2.6, 1.8, 1.8, 1.5, 1.3 and 1.5 cm^{-1} , respectively. Particularly, there is a gradual increase in the splitting energy of the SWE modes $\Phi_3^{(1,2)}$, $\Psi_3^{(1,2)}$, and $\Phi_4^{(1,2)}$, except for $\Psi_4^{(1,2)}$ which shows a slight decrease, with decreasing temperature. At 5 K, the values of splitting energy of $\Phi_3^{(1,2)}$, $\Psi_3^{(1,2)}$, and $\Phi_4^{(1,2)}$ are found to be 2.2, 2.5, and 2.5 cm^{-1} , respectively. Here, the increase in the values of splitting energy seem to be related to the increase in SIA at the corresponding temperature [45].

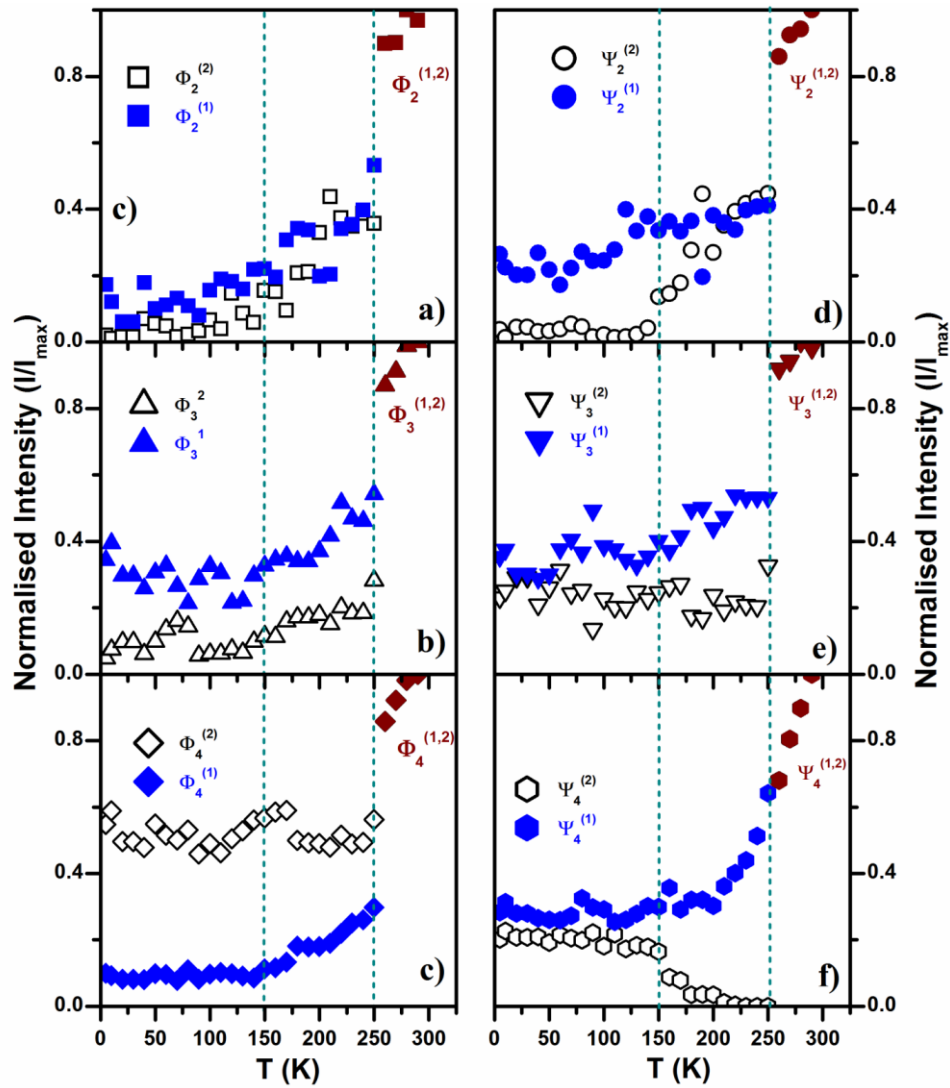


Figure 4.5 Normalized integrated intensity of (a) $\Phi_2^{(1,2)}$, (b) $\Phi_3^{(1,2)}$, (c) $\Phi_4^{(1,2)}$, (d) $\Psi_2^{(1,2)}$, (e) $\Psi_3^{(1,2)}$ and (f) $\Psi_4^{(1,2)}$ as a function of temperature.

4.3.1.2. Low temperature changes in SW Mode Intensity

The normalized integrated intensity (I/I_{\max}) of SWE modes are followed as a function of temperature and are as shown in Figures 4.5a-4.5f. These graphs are broadly divided into three regions: (i) Region I: $300 \text{ K} < T < 250 \text{ K}$; Region II: $250 \text{ K} < T < 150 \text{ K}$ and region III: $T < 150 \text{ K}$. All the SW mode intensities, apart from the intensity of $\Psi_4^{(2)}$ mode, are found to have an overall decreasing trend with decreasing temperature. Such type of anomalous behavior in SW mode intensities have also been reported by Rovillain et al. [72], although the trend in mode intensities reported by them is quite different from what we observe in the present study. In our case, there is a discontinuous change in the temperature evolution of SW mode intensities at 250 K, which is because of the sharing of spectral weight of parent SW modes between their daughter modes (Figures 4.5a-4.5f). This fact becomes evident from Table 4.1, where it can be seen that the intensities of nondegenerate daughter modes almost add up to the intensity of the parent degenerate mode. Fishman et al. [17] found based on their microscopic model that turning on the DM interaction along the pseudocubic $\langle 111 \rangle_{pc}$ direction causes a tilt in the spin cycloid, which, in turn, lifts the degeneracy of Ψ_0 and Φ_1 modes. Likewise, we believe that the reorientation of spins across the SRT at 250 K lifts the degeneracy of all the SW modes which is reflected as splitting of all these SWEs in our sample. We have also seen from the results presented in the previous chapter that the non-collinear magnetic structure of BiFeO_3 undergoes considerable changes at low temperature. It is due to the onset of rotation of the ordered spins out of the easy magnetization plane $(111)_{pc}$ below 250 K and culminating in an orientation orthogonal to the plane at 150 K [124]. Accordingly, a weak ferromagnetic ordering occurs as Fe 3d spins couple via DM interaction. Thus, the continuous increase in coercivity as we decrease temperature below 150 K (discussed in section 3.3.1 of chapter 3) is in accordance with the increase in SIA with decreasing temperature [45]. Further

theoretical treatment may be desirable to fully understand the exact nature of these interactions.

Table 4.1 Normalized Spectral weight distribution of SW modes across the magnetic transition at 250 K.

260 K	250 K		
$I/I_{\max}(\Phi_m^{(1,2)}/\Psi_m^{(1,2)})$ ($I_{1,2}$)	$I/I_{\max}(\Phi_m^{(1)}/\Psi_m^{(1)})$ (I_1)	$I/I_{\max}(\Phi_m^{(2)}/\Psi_m^{(2)})$ (I_2)	I_1+I_2
0.90 ($\Phi_2^{(1,2)}$)	0.53 ($\Phi_2^{(1)}$)	0.36 ($\Phi_2^{(2)}$)	0.89
0.86 ($\Psi_2^{(1,2)}$)	0.41 ($\Psi_2^{(1)}$)	0.45 ($\Psi_2^{(2)}$)	0.86
0.87 ($\Phi_3^{(1,2)}$)	0.54 ($\Phi_3^{(1)}$)	0.28 ($\Phi_3^{(2)}$)	0.82
0.92 ($\Psi_3^{(1,2)}$)	0.53 ($\Psi_3^{(1)}$)	0.33 ($\Psi_3^{(2)}$)	0.86
0.86 ($\Phi_4^{(1,2)}$)	0.30 ($\Phi_4^{(1)}$)	0.56 ($\Phi_4^{(2)}$)	0.86
0.68 ($\Psi_4^{(1,2)}$)	0.64 ($\Psi_4^{(1)}$)	0.0001 ($\Psi_4^{(2)}$)	0.64

4.3.1.3. Intensity changes below 250K

With the exception of the $\Psi_4^{(2)}$ mode, intensities of all the other SW modes show a gradual decrease in this temperature range. Below 150 K, these intensities remain nearly constant. In fact, the trend in intensity of these SWE modes exhibits a one-to-one correspondence with the temperature variation of anharmonicity of the cycloid modulation as observed by Rusakov et. al., (see Figure 2 of ref. [125]): corresponding to the gradual decrease in intensity between 250-150 K, an increase in cycloid anharmonicity is observed for the same temperature range. Below 150 K, there is a plateauing of both the magnon intensity (Figure 4.5) as well as the anharmonicity. This correlation is understandable, particularly since the intensity of high-energy magnons is directly related to the anharmonicity of the spin cycloid of BiFeO₃ [56]. Thus, the overall decrease in mode intensity with the lowering of temperature indicates that these SWE modes are getting partially suppressed with decreasing temperature. Hence, the observed near-complete suppression of SWEs is due to an increase in both the single-ion anisotropy as well as the anharmonicity of the spin cycloid at low-temperature. This observation is consistent with the improved magnetic and magnetoelectric properties of BiFeO₃ at low temperatures below

150 K [60, 61, 95]. Here, we notice two clear anomalies at 250 and 150 K in the temperature evolution of intensity. These two anomalies at 250 and 150 K are due to the magnetic transitions in BiFeO₃ [55, 70, 72] related to spin reorientation away from the easy plane of magnetization [95]. And the anomaly seen for $\Phi_2^{(2)}$ and $\Psi_2^{(2)}$ at 200 K corresponds to a transition related to the magnetoelastic effect [115].

The normalized integrated intensity of extra-cyclon $\Psi_4^{(2)}$ mode, shown in Figure 4.5f, increases gradually with decreasing temperature until 150 K and then remains more or less constant below 150 K. A previous study [81] has conclusively shown this mode to be an electromagnon. Further, we see that the intensity variation of this mode is similar to that of the newly emerging 111 cm⁻¹ mode, which we had previously reported [95] to be an electromagnon based on its anomalous variation close to a dielectric anomaly at 25 K. In the case of the 56 cm⁻¹ mode the anomaly could be subtle and hence not distinctly observed. Thus, the increase in the integrated intensity of this mode is due to an enhancement in the magnetoelectric coupling of BiFeO₃ at low temperatures, that was observed previously in a magnetodielectric study on the same samples [61]. It is known that the high-frequency magnons are also coupled, albeit weakly, with electric order via quadratic magnetoelectric effects in BiFeO₃ [56].

In essence, our infrared study shows that multiferroic BiFeO₃ undergoes two magnetic transitions below 260 K, which in turn influence the behavior of the SW modes. In addition, an increased anharmonicity in the modulation of the spin cycloid, together with an increase in single-ion anisotropy at low-temperature, tend to suppress the cycloidal spin structure in BiFeO₃, as seen in the gradual weakening of its SW modes with decreasing temperature. The observed complex magnetic behavior in BiFeO₃ at low temperature, particularly, the lifting of degeneracy of the SW modes and the appearance of new magnon modes, requires further theoretical investigation.

In order to obtain insight into the spin dynamics in BiFeO_3 , electron paramagnetic resonance (EPR) investigations have been carried out between 300-77 K and the obtained results are discussed in the next section.

4.3.2. EPR measurements

Figure 4.6 displays the EPR spectra of BiFeO_3 sample at a few selected temperatures. At room temperature, the spectrum shows one broad asymmetric peak which is found to undergo substantial modification at low temperature. It can be seen from the Figure 4.6 that the EPR signal intensity decreases significantly on lowering the temperature. Since the EPR signal is the derivative of the resonance absorption signal, double integration of this EPR signal gives the peak area, which is proportional to the number of excited spins or the spin susceptibility.

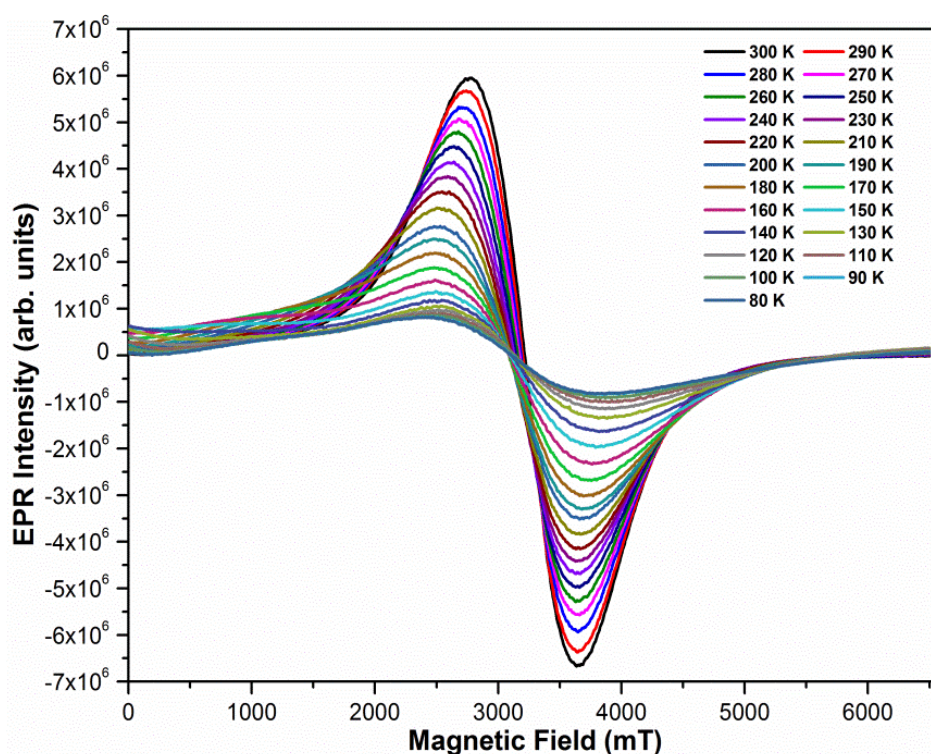


Figure 4.6 EPR spectra of BiFeO_3 at a few selected temperatures.

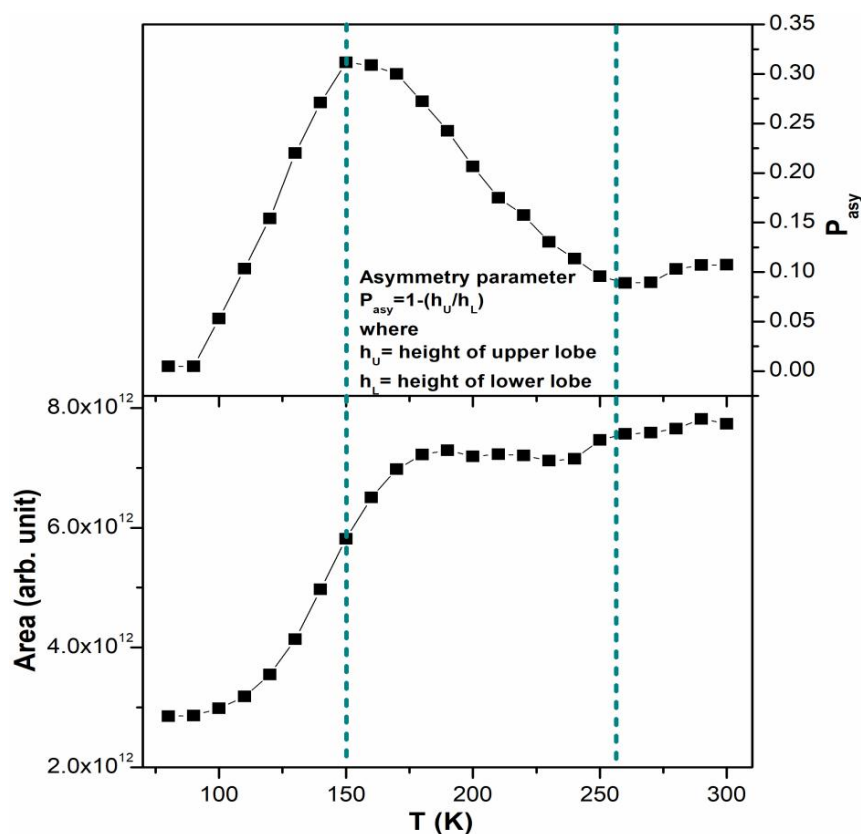


Figure 4.7 Asymmetry parameter and peak area under the EPR signal in BiFeO_3 .

Figure 4.7a displays the peak area of the EPR signal of BiFeO_3 as a function of temperature from 300 to 80 K. The area starts decreasing sluggishly with decreasing temperature up to 260 K and shows a step-like drop at around 250 K. After that the area remains almost constant in the temperature range from 240 to 180 K. Another anomalous behavior in the peak area variation is clearly observed at around 150 K. Below 120 K, however, the peak area decreases gradually. Here, the decrease in area with decreasing temperature is because of spin freezing process at low-temperatures. The observed anomalous behaviors at 150 and 250 K correspond to the SRTs observed at that temperatures. In addition to this, there is an asymmetry in the EPR signal of BiFeO_3 , which can be visualized from the height difference of upper and lower lobe of the EPR signals. Here we have calculated the asymmetry parameter (P_{asy}) by using the following equation.

$$P_{asy} = 1 - \frac{h_U}{h_L} \quad 4.3$$

This asymmetry parameter of magnetic resonance has been followed as a function of temperature. It is observed that the P_{asy} is almost remains constant from 300 to 250 K and then increases rapidly up to 150 K. After that there is a sudden drop in asymmetry parameter down to 90 K. Finally, the resonance signal becomes symmetric. In fact, the asymmetry in EPR line shape is because of two contribution i.e. one is for ferromagnetic component related to spin cycloid and other one is because of paramagnetic contribution related to low symmetry Fe^{3+} ions [126, 127].

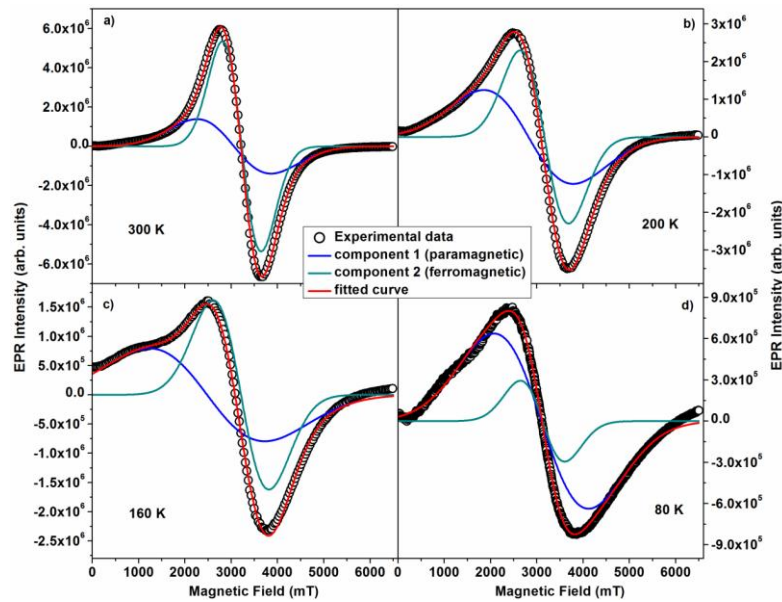


Figure 4.8 EPR spectra curve-fitted with two Gaussian components at (a) 300, (b) 200, (c) 160 and (d) 80 K.

Figure 4.8 displays the EPR spectra for a few selected temperatures. We were able to achieve reasonably good fit to the EPR signal using two Gaussian components where one of them is for the high field ferromagnetic contribution and other one is for the low field paramagnetic component. We have further followed the temperature evolution of the fitted lineshape parameters of the paramagnetic and ferromagnetic components. Figures 4.9 and

4.10 display the temperature evolution of area, g-factor and peak to peak linewidth (ΔB_{pp}) of the para and ferromagnetic components, respectively. It is observed that the peak areas corresponding to the ferromagnetic and the paramagnetic components show anomalous behavior at ~ 250 and 150 K, which correspond to the SRTs occurring at these temperatures.

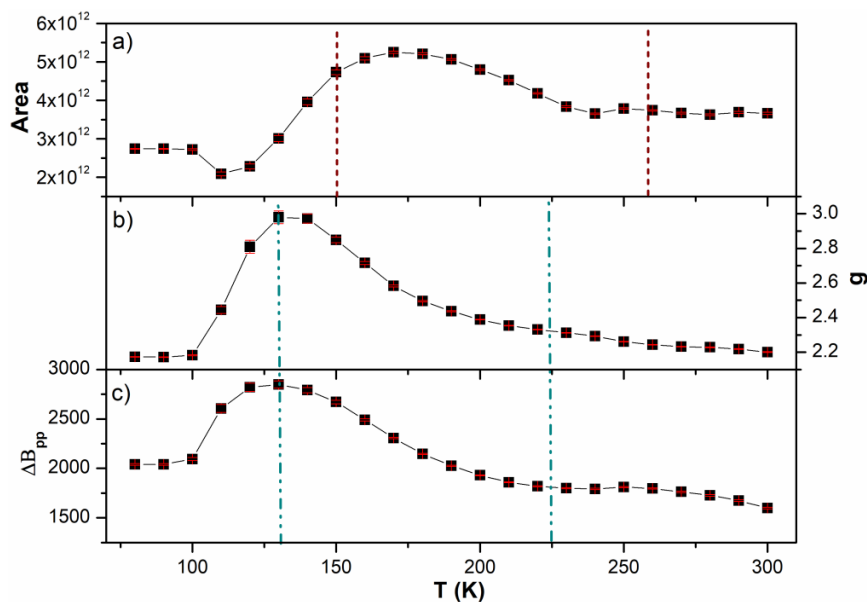


Figure 4.9. Low temperature plot of lineshape parameters of the paramagnetic component (The solid lines are guide-to-the-eye).

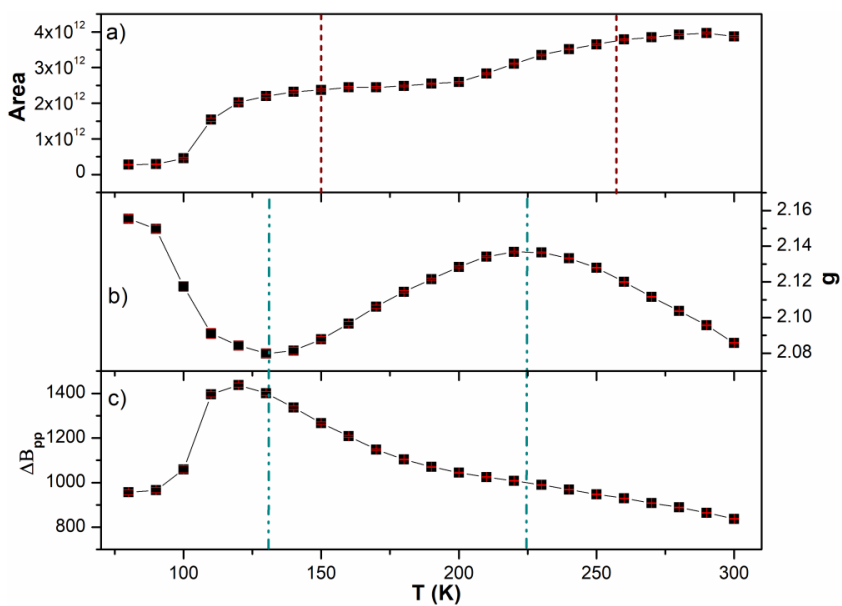


Figure 4.10. Low temperature plot of the lineshape parameters of the ferromagnetic component (The solid lines are guide-to-the-eye).

We know that the linewidth of EPR signal gives information about spin-spin and spin-phonon relaxation time. From Fig. 4.10c the linewidth of paramagnetic and ferromagnetic components are found to gradually increase with lowering of temperature up to 130 K. This shows the regular increase of relaxation time at low temperatures. Below 130 K, there is a sudden decrease in the linewidth in both the components as noticed from Figures 4.9c and 4.10c. This may be probably due to a decrease in spin-spin interaction as the destruction of spin cycloid takes place through increase in SIA below 150 K.

Further, the g-factors of paramagnetic and ferromagnetic components have been calculated by using their corresponding peak positions. The working formula to calculate g-factor is given by.

$$g = \frac{h\nu}{\mu_B B} \quad 4.4$$

Where h , ν , μ_B and B are the Planck's constant, microwave frequency, Bohr magneton and resonant magnetic field, respectively. At 300 K, the g-factor of paramagnetic component is found to be 2.2 (Figure 4.9b) [127] which shows that the magnetic spin due to oxygen defect is not completely isolated and is under the influence of the surrounding spins. Therefore paramagnetic and ferromagnetic components are sensitive to SRTs, which we have already noticed from their temperature evolution of corresponding areas. Moreover, the temperature evolution of g-factor shows that there are anomalies observed in their behavior at 225 and 130 K (see Figures 4.9b and 4.10b). Below 130 K, there is a sudden increase in g value. Further, the shift in g-factor, Δg , is directly proportional to the degree of spin canting as given by the relation [128, 129]:

$$\Delta g = \frac{-2}{\alpha S} \vec{n} \bullet \vec{M} \quad 4.5$$

where α is the spin-orbit structure factor, S is total spin, \vec{n} is the spin direction and \vec{M} is the total magnetization. Therefore, we have plotted the relative shift of g-factor,

$$\Delta g/g = \frac{g_T - g_{300K}}{g_{300K}} \quad (\text{also called the spin-canting order parameter}) \text{ of the ferromagnetic}$$

component as a function of temperature (Figure 4.11).

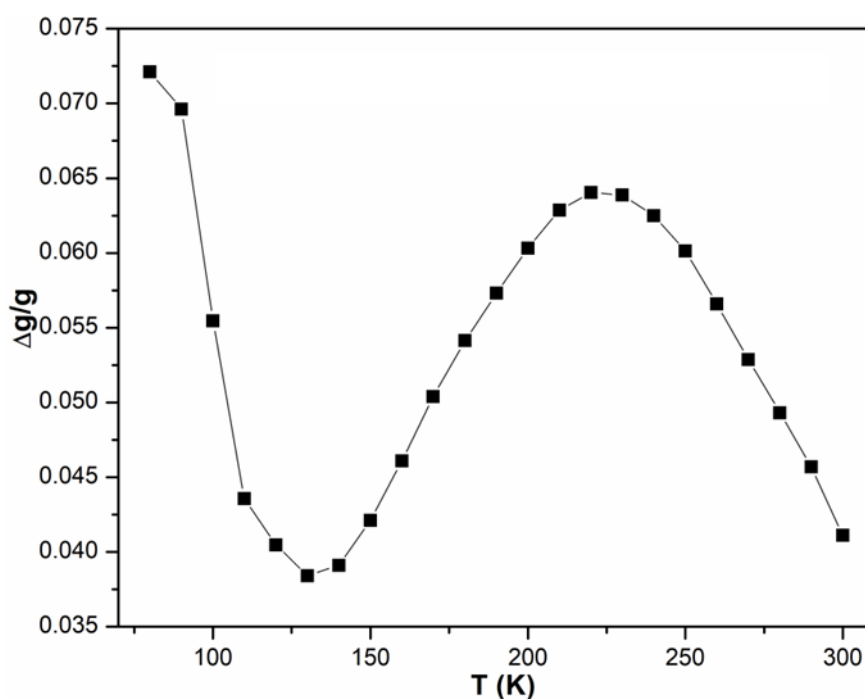


Figure 4.11. Temperature variation of $\Delta g/g$ corresponding to the ferromagnetic component.

It is noticed that with decreasing temperature, the value of $\Delta g/g$ is found to be increasing up to 225 K followed by a decreasing trend up to 130 K. Finally, $\Delta g/g$ value climbs up rapidly below 130 K. Here, upon lowering the temperature from 300K, the increasing trend in $\Delta g/g$ up to 225 K is due to an increase in magnetization, while the decreasing trend in $\Delta g/g$ from 225 to 130 K may be because of hampering of spin canting due to spin reorientation. Below 130 K, the shooting up of $\Delta g/g$ value indicates a sharp

enhancement of magnetic properties due to increase in DM interaction. This is in accordance with our temperature dependent coercivity and infrared results, where suppression of SWEs are seen at low temperature. Further, we can add here that the increase in the DM interaction accounts for the observed increase in the magnetoelectric property [61] of BiFeO₃ at low temperatures.

4.4. Conclusion

We have investigated the spin-wave excitation modes of bulk BiFeO₃ below room temperature using far-infrared spectroscopy and EPR. All the observed magnon modes in the infrared spectra were successfully assigned to the cyclons (Φ) and the extra-cyclons (Ψ). Furthermore, the two anomalies observed in the integrated intensity of the cyclon and extra-cyclon modes at 250 and 150 K are related to the magnetic transitions in BiFeO₃. The degeneracy of high-energy magnon modes gets lifted across the spin reorientation transition due to higher order spin harmonics generated through spin reorientation. In addition, a gradual suppression of the SW modes with a decrease in temperature is witnessed due to the continuous destruction of the spin cycloid of BiFeO₃ with temperature. This finding is ascribed to the enhanced anharmonicity in the spin cycloid and large single-ion anisotropy at low temperatures, which ultimately alter the spin cycloid structure leading to the improved magnetic and magnetoelectric properties below 150 K in pristine BiFeO₃. The EPR results provide information about spin dynamics in terms of degree of spin canting across the SRTs. They also correlate well with the improved magnetic and magnetocaloric properties at low temperatures.

Chapter 5

Suppression of spin wave excitations in BiFeO₃ through aliovalent substitution

The highlight of this chapter is the study of the influence of substituting aliovalent dopant ions at Bi-site in BiFeO₃ on the behavior of phonons as well as SWEs through infrared reflectivity measurements and to effect an improvement in magnetic and magnetoelectric properties. The infrared findings are also complemented by low frequency Raman measurements.

5.1. Introduction

BiFeO₃ adopts a G-type antiferromagnetic spin structure brought about by superexchange interaction. However, neighboring spins are not perfectly antiparallel, with a slight canting of spins, which is as a consequence of DM interaction. In fact, the magnetic structure of BiFeO₃ can be described through antiferromagnetic spin arrangement embodied with an incommensurate spiral array of canted spins called spin cycloid over a length of 62 nm propagating along the pseudo cubic direction of $\langle 10\bar{1} \rangle_{pc}$ [13, 119]. Besides, the local magnetic moment generated via canted spins gets averaged out over spin cycloid [88]. Thus the macroscopic magnetization gets hampered by the cycloidal spin arrangements.

Furthermore, BiFeO₃ is reported to be a weakly coupled magnetoelectric material. Even though the symmetry of BiFeO₃ crystal structure allows us to have a strong linear magnetoelectric (ME) effect, it gets effectively canceled out as a consequence of the cycloidal array of spins [88]. So the higher-order coupling effect plays a vital role in order to have a weak ME effect in BiFeO₃. From this, it can be said that the spin cycloid doesn't favor the strong linear ME coupling effect. Therefore, Uniyal et al. suggest that the incommensurate spin cycloid needs to be destroyed to achieve the linear ME effect [130]. This destruction of the spin cycloid can be achieved through applying high magnetic [88,

131-133] or electric field [134], hydrostatic pressure [89], induced strain generated in the thin-film form [92, 135] or through doping effect [90, 91]. Particularly, cationic substitution at the bismuth site increases magnetocrystalline anisotropy, which energetically inhibits the formation of a spin cycloid [136].

The spin cycloid in BFO is known to give rise to two types of spin wave excitations (SWEs) known as cyclon (in-plane) and extracyclon (out-of-plane) modes, which are found to be sensitive to electric [15] and magnetic field [16, 17] and hydrostatic pressure [9]. This shows the potential of this material for use in magnonic devices where magnons are used to transmit and process the information [18, 19]. Moreover, it has been understood from the previous chapter that the increase in SIA and anharmonicity of the spin cycloid at low temperatures significantly modify the behavior of SWEs of BiFeO₃. This prompted us to investigate the SWEs of BiFeO₃ through doping. However, there are hardly any studies with regard to the doping effect on SWEs in the doped BiFeO₃ sample. Besides, the effect of SIA or magnetocrystalline anisotropy and anharmonicity of spin cycloid brought about by doping on SWEs of BiFeO₃ has not been explored to date to the best of our knowledge. Further, this study can provide new opportunities to use doped BiFeO₃ samples in magnonic devices. Therefore we have, here, investigated the doping effect on phonons and SWEs in Ca and/or Ba-doped BiFeO₃ samples through infrared reflectivity measurements. This study shows that doping-induced chemical pressure plays a vital role in phonon behavior and there is complete lifting of the degeneracy followed by a near-complete suppression of the SWEs through an increase in SIA and anharmonicity in Ca-based samples.

5.2. Experimental

Ceramic samples of BiFeO₃ (BFO), Bi_{0.9}Ba_{0.1}FeO_{2.95} (BBFO), Bi_{0.9}Ba_{0.05}Ca_{0.05}FeO_{2.95} (BBCFO) and Bi_{0.9}Ca_{0.1}FeO_{2.95} (BCFO) were synthesized through modified sol-gel method already described in section 2.1.1. Phase purity of the samples was

confirmed through powder x-ray diffraction [97]. These samples were pelletized into disc form having a radius of 10 mm and thickness of 1 to 2 mm. These pellets were then sintered at 1123 K for 6 hours. The density of the sintered pellet was found to be greater than 90 % of the theoretical density. From Rietveld refinement of the x-ray diffraction patterns of these samples, a reduction of unit cell volume is observed in all the doped samples compared to the pristine sample [97]. To mention specifically in terms of changes in local structure, Fe-O1 and Fe-O2 bond lengths as well as Fe1-O-Fe2 bond angle are all found to decrease in the case of the doped samples (Table 5.1). In particular, the BCFO sample is found to have the least unit cell volume, Fe-O bond lengths and bond angle. Moreover, the magnetic properties are expected to get influenced by these local structural modifications. In fact, it has been observed that Ca-based samples have weak ferromagnetic behavior (please see the value of H_c and M_r in Table 1) whereas BBFO continues to retain antiferromagnetic behavior [97]. Interestingly, BCFO shows the largest values of H_c and M_r , which points to the enhanced magnetism compared to other samples (Table 1). Based on the improved magnetism and induced chemical pressure in the lattice, we may expect a destruction of the spin cycloid through an increase in SIA.

Table 5.1 The estimated values of reduced unit cell volume ($\Delta V/V$), bond length (\AA), bond angle ($^\circ$), remnant magnetization (M_r) and coercivity (H_c) [97].

Sample	$\Delta V/V$ (%)	Bond length (\AA)	Bond angle of Fe1-O-Fe2 ($^\circ$)	M_r ($\mu_B/\text{f.u.}$)	H_c (kOe)
BFO	0	Fe-O1 (1.903) Fe-O2 (2.141)	157.39	0.01	0.1
BBFO	-1.22	Fe-O1 (1.897) Fe-O2 (2.131)	157.37	0.01	0.4
BBCFO	-1.23	Fe-O1 (1.896) Fe-O2 (2.128)	157.35	0.06	5.8
BCFO	-2.08	Fe-O1 (1.893) Fe-O2 (2.124)	157.33	0.12	12.5

For infrared reflectivity measurements, samples in the form of pellets were polished to mirror finish using diamond paste and then cleaned with acetone. Post polishing, the pellets were heated at 673 K for 4 hours in order to remove any surface residual stress that may have been generated due to the mechanical polishing process. Far-infrared reflectivity measurements were carried out on the polished pellets at near-normal incidence using Bruker Vertex 80v FTIR spectrometer fitted with water-cooled mercury source, 6-micron mylar beam splitter and a liquid helium-cooled silicon bolometer operating at 4.2 K. The room temperature reflectivity spectra of these samples were recorded at a resolution of 0.5 cm^{-1} . The low-frequency Raman spectra of these samples were recorded using inVia micro Raman spectrometer, (Renishaw, UK). The main components used in these measurements were a 514.5 nm laser source, an Eclipse filter and a CCD detector. The Raman spectra were recorded with a resolution of 1.5 cm^{-1} .

5.3. Results and discussions

Figure 5.1 displays the reflectance spectra, $R(\omega)$, of doped and pristine BiFeO_3 samples in the spectral range from 30 to 650 cm^{-1} . They are comprised of SWEs in the very low frequency part of the spectrum and the phonon part towards the higher end of the far-infrared spectrum spanning the spectral range from 70 to 650 cm^{-1} . The observed features below 70 cm^{-1} (marked by the rectangular box as well as a right inset of Figure 5.1) in the reflectance spectra are related to characteristic resonances arising from the samples rather than to any interference pattern from the two parallel surfaces of the pellets. In favor of this statement, we put forward the following arguments:

1. The pellets are not transparent, which have been confirmed through Far-IR transmission measurements.
2. For these spectral features to be really considered as a result of interference, our sample thicknesses should be around 0.1-0.2 mm, but, as already

mentioned in the experimental section above, our samples are 10-20 times thicker.

- Moreover, the clear temperature evolution of these low-frequency features in the pristine sample laid out in detail in Chapter 4 gives further conclusive evidence toward this.

Therefore these characteristic features in the low-frequency range of the reflectance spectra are related to the magnetic or magnetodielectric resonances, also known as spin wave excitations (SWEs).

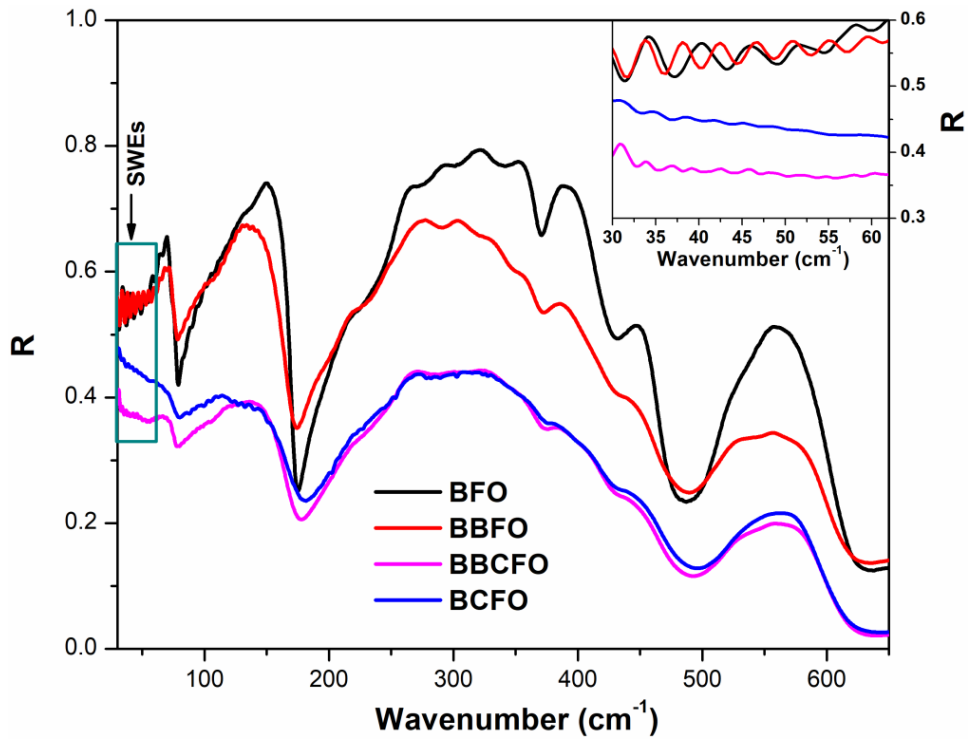


Figure 5.1 Infrared reflectance measurements of pristine and doped BiFeO_3 samples. The box in the low-frequency region shows SWEs which have been shown on an expanded scale in the inset.

5.3.1. Phonon Contribution

The phononic parts of the reflectance spectra were fitted with four-parameter model as described in equations 3.1 and 3.2, and the fitted spectra are displayed in Figures 5.2a-5.2d. Best fit for the Ca-based sample spectrum could be achieved only after the inclusion of a Drude component, $\left(-\varepsilon_\infty \frac{\omega_p^2}{\omega^2 + i\gamma_p \omega}\right)$, in the four-parameter model, unlike for the spectra

of other samples. Here ω_p is the plasma frequency and γ_p is related to Drude scattering rate. The increasing trend in reflectivity close to zero frequency in the reflectance spectra of Ca-based samples (see the reflectance spectra for BBCFO and BCFO in Figures 5.1 and 5.2) give an indication of Drude's contribution. Further justification to the incorporation of Drude's contribution comes from the reported hopping conductivity across Fe^{3+} and Fe^{4+} in Ca doped BiFeO_3 sample [137]. Occurrence of mixed valence viz., Fe^{3+} and Fe^{4+} - in Ca doped BFO is also predicted through DFT calculations [138]. However, this aspect needs to be examined further in more detail.

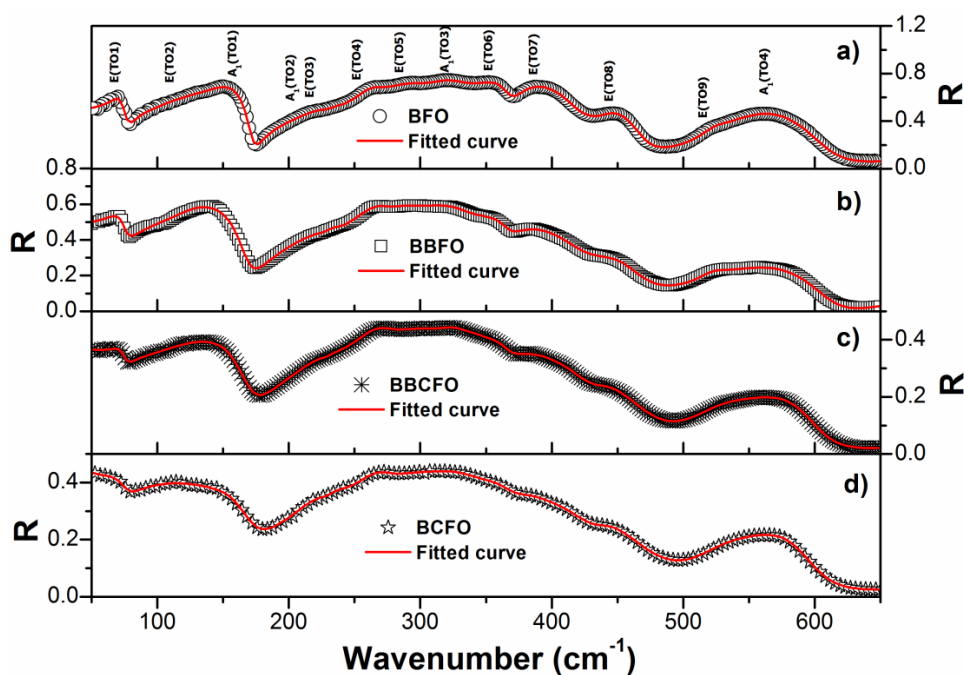


Figure 5.2 Reflectance spectra of (a) BFO, (b) BBFO, (c) BBCFO and (d) BCFO.

From the theoretical fits, all the 13 phonon modes allowed by the rhombohedral symmetry [52, 81] could be clearly observed in all the studied samples. These phonons are assigned with their appropriate symmetries, as shown in Figure 5.2a. Here the low-frequency E(TO1) and E(TO2) modes are Bi related vibrations, while E(TO4) and E(TO9) modes are related to FeO_6 octahedral bending and stretching vibrations, respectively. Substantial changes in the phonon behavior are clearly observed with Ba and Ca doping in

the bismuth ferrite lattice, as manifested from the significant changes found in the lineshape parameters of several phonon modes obtained from the fitting (see Table 5.2). Notably, Ca-based samples show a significant increase in phonon frequencies as well as damping factors, while BBFO shows only a moderate change. The extent of hardening of E(TO1) and E(TO2) modes is maximum in the BCFO sample. This is because of the substitution of the much lighter Ca atom at Bi site.

Table 5.2 The obtained values of reduced unit cell volume ($\Delta V/V$), phonon frequency (ω), and damping constant (γ) of the BiFeO₃-based samples.

Sample	$\Delta V/V$ (%)	ω of E(TO1) (cm ⁻¹)	γ of E(TO1) (cm ⁻¹)	ω of E(TO2) (cm ⁻¹)	γ of E(TO2) (cm ⁻¹)	ω of E(TO4) (cm ⁻¹)	γ of E(TO4) (cm ⁻¹)	ω of E(TO9) (cm ⁻¹)	γ of E(TO9) (cm ⁻¹)
BFO	0	71.0 (± 0.4)	9.6 (± 1.8)	126.3 (± 2.1)	49.7 (± 10)	262.4 (± 1.3)	19.5 (± 7.5)	521.2 (± 1.1)	23.6 (± 13)
BBFO	-1.22	69.7 (± 0.9)	15.3 (± 1.8)	123.7 (± 2.6)	69.1 (± 12)	264.6 (± 1.5)	37.0 (± 7.8)	521.8 (± 1.6)	48.7 (± 14)
BBCFO	-1.23	74.3 (± 1.2)	11.4 (± 2.5)	131.7 (± 2.9)	71.7 (± 15)	265.5 (± 1.6)	37.9 (± 16)	521.8 (± 1.8)	68.9 (± 18)
BCFO	-2.08	76.8 (± 1.5)	22.0 (± 3.8)	133.5 (± 3.1)	91.8 (± 20)	267.1 (± 1.9)	41.5 (± 18)	525.2 (± 2.0)	67.9 (± 20)

Interestingly, both E(TO1) and E(TO2) modes are found to soften in Ba doped BFO sample. These two modes don't show a blue shift in frequency expected from the atomic weight differences of Ba and Bi atoms. Here, the larger ionic radius of Ba²⁺ ion plays a fundamental role in weakening of the force constant in the Bi/Ba-O bonds, resulting in the observed anomalous softening behavior. This type of softening has been reported earlier in Ba doped bismuth ferrite and similar perovskite systems [139, 140]. However, such type of anomalous behavior of Bi related vibrations has not been observed in Ca-based samples as the ionic radius of Ca²⁺ (0.99 Å) is much smaller than that of Ba²⁺ (1.35 Å) and comparable to that of Bi³⁺ (1.03 Å).

The behavior of $E(TO1)$, $E(TO2)$, $E(TO4)$, and $E(TO9)$ modes in Ca-based samples have been further investigated with regard to reduced unit cell volume obtained from the Rietveld refinements (cf. section 2.1 in chapter 2). Figure 5.3a displays the relative shift $\left(\frac{\Delta\omega}{\omega_{BFO}} = \frac{\omega_{doped} - \omega_{BFO}}{\omega_{BFO}} \right)$ in the frequencies of these modes versus the reduced unit cell volume ($\Delta V/V$). All these modes show positive relative shifts, which shows the hardening behavior of these phonons with reduced unit cell volume. It has been observed that these modes show gradual hardening with decreasing unit cell volume. Mainly, the low-energy phonon modes $E(TO1)$ and $E(TO2)$ show a significant hardening ($\Delta\omega/\omega > 4\%$) with *increasing* Ca content. Maximum hardening of these two Bi-related modes is noticed in the BCFO sample, which is due to the combined effect of doping with lighter Ca atom at Bi site and the observed highest volume contraction in the sample. Compared to this, there is only a slight hardening ($\Delta\omega/\omega < 2\%$) in the $E(TO4)$ and $E(TO9)$ modes with increasing Ca-content. This is also in accordance with the decreasing Fe-O bond lengths for the Ca-based sample (see Table 2) [97]. From these observations, it can be concluded that doping at Bi site has an effect across the unit cell. In addition, the damping factors (γ) of these modes are also found to increase with decreasing $\Delta V/V$ (Figure 5.3b). The increase in the damping factor is due to doping-induced changes in the local structure as is evident from Table 5.1. Thus the correlated changes in frequency and damping factor of the modes with reduced unit cell volume points to the fundamental role of doping induced chemical pressure in the bismuth ferrite lattice.

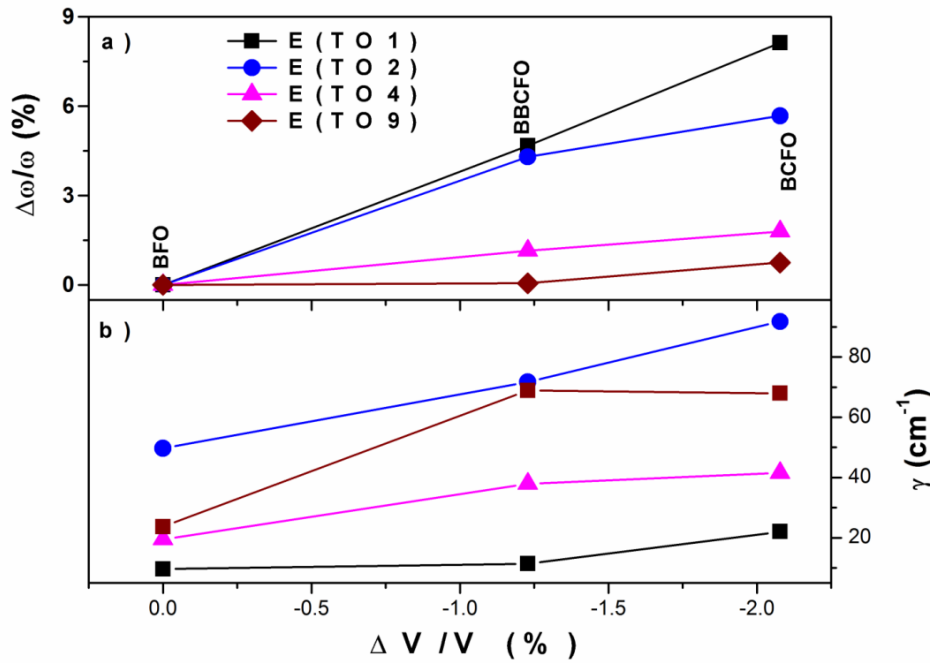


Figure 5.3 Plots of (a) percentage relative shift and (b) linewidth versus reduced unit cell volume.

Overall, the induced chemical pressure modifies the octahedral crystal field of FeO_6 in BiFeO_3 [82], which eventually affects the behavior of the phonon modes. This observation is analogous to the effects of hydrostatic pressure on the phonon modes of BiFeO_3 [141]. Moreover, the induced chemical pressure in BiFeO_3 through Ca doping is expected to alter its magnetic properties. This will be further investigated by probing the behavior of low-energy SW excitations of these BiFeO_3 -based samples.

5.3.2. Magnon contribution

5.3.2.1. Infrared measurements

Figure 5.4 illustrates the multipoint background subtracted extinction coefficient (k) spectra of BFO-based samples derived from the reflectance spectra through Kramers-Kronig transformation. The spin-wave modes are clearly seen in the k -spectra of all the studied samples. This low frequency part of the k spectra is fitted with a sum of Gaussians to extract the mode parameters of the SWEs. The obtained mode frequencies of SWEs of the pristine sample are 35.6, 41.7, 47.5, 53.2 and 59.2 cm^{-1} , which are assigned, based on the reported

literature [57], as $\Psi_2^{(1,2)}$, $\Phi_3^{(1,2)}$, $\Psi_3^{(1,2)}$, $\Phi_4^{(1,2)}$ and $\Psi_4^{(1,2)}$ respectively. Here, Φ 's are cyclon modes and Ψ 's are extra-cyclon modes.

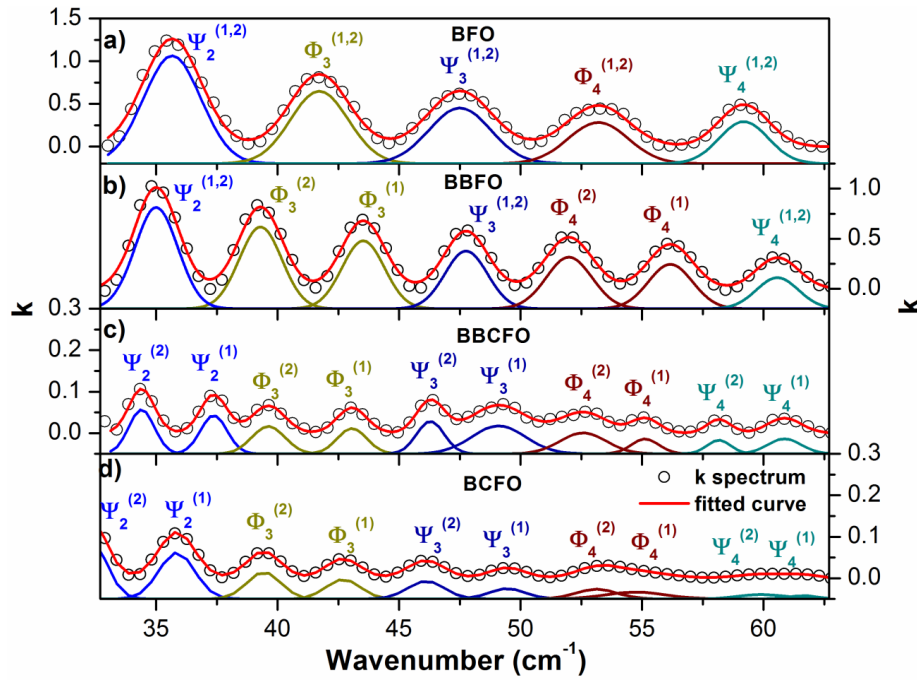


Figure 5.4 k -spectra of (a) BFO, (b) BBFO, (c) BBCFO and (d) BCFO fitted with Gaussian line shapes.

Table 5.3 The SWE mode frequencies for pristine and doped BFO sample.

SWE frequency of BFO (cm-1)	SWE frequency of BBFO (cm-1)	SWE frequency of BBCFO (cm-1)	SWE frequency of BCFO (cm-1)
35.6 ($\Psi_2^{(1,2)}$)	35.0 ($\Psi_2^{(1,2)}$)	34.4 ($\Psi_2^{(2)}$)	32.3 ($\Psi_2^{(2)}$)
		37.4 ($\Psi_2^{(1)}$)	36.0 ($\Psi_2^{(1)}$)
41.7 ($\Phi_3^{(1,2)}$)	39.3 ($\Phi_3^{(2)}$)	39.6 ($\Phi_3^{(2)}$)	39.4 ($\Phi_3^{(2)}$)
	43.5 ($\Phi_3^{(1)}$)	43.1 ($\Phi_3^{(1)}$)	42.7 ($\Phi_3^{(1)}$)
47.5 ($\Psi_3^{(1,2)}$)	47.8 ($\Psi_3^{(1,2)}$)	46.3 ($\Psi_3^{(2)}$)	46.1 ($\Psi_3^{(2)}$)
		49.1 ($\Psi_3^{(1)}$)	49.4 ($\Psi_3^{(1)}$)
53.2 ($\Phi_4^{(1,2)}$)	52.0 ($\Phi_4^{(2)}$)	52.6 ($\Phi_4^{(2)}$)	53.1 ($\Phi_4^{(2)}$)
	56.2 ($\Phi_4^{(1)}$)	55.1 ($\Phi_4^{(1)}$)	55.5 ($\Phi_4^{(1)}$)
59.2 ($\Psi_4^{(1,2)}$)	60.6 ($\Psi_4^{(1,2)}$)	58.1 ($\Psi_4^{(2)}$)	59.6 ($\Psi_4^{(2)}$)
		60.7 ($\Psi_4^{(1)}$)	61.9 ($\Psi_4^{(1)}$)

It can be seen that the SWE modes are modified significantly in the Ca-based samples, while only to a moderate extent in the case of the BBFO (see Figures 4b-4c). There

is an overall increase in the number of SWE modes on doping. The number of modes in the BBFO sample is found to be 7, while the number of SW modes in Ca-based samples is detected to be 10 (see Table 5.3). In fact, this increase in the number of SWEs is because of the lifting of the degeneracy of the five degenerate SWEs observed in the pristine sample. Thus, there is a partial lifting of degeneracy in BBFO, while a complete lifting of degeneracy is observed in the case of the Ca-based samples. Here, the lifting of SW mode degeneracy in doped samples is attributed to an increase in SIA [57], on account of changes in the crystal field brought about by chemical pressure. The complete lifting of degeneracy of the SW modes in BBCFO and BCFO samples point to the significant increase in SIA in these materials, which manifests from the induced chemical pressure and substantial local structural changes in Ca-based samples (see values of Fe-O bond length and Fe-O-Fe bond angle in Table 5.1).

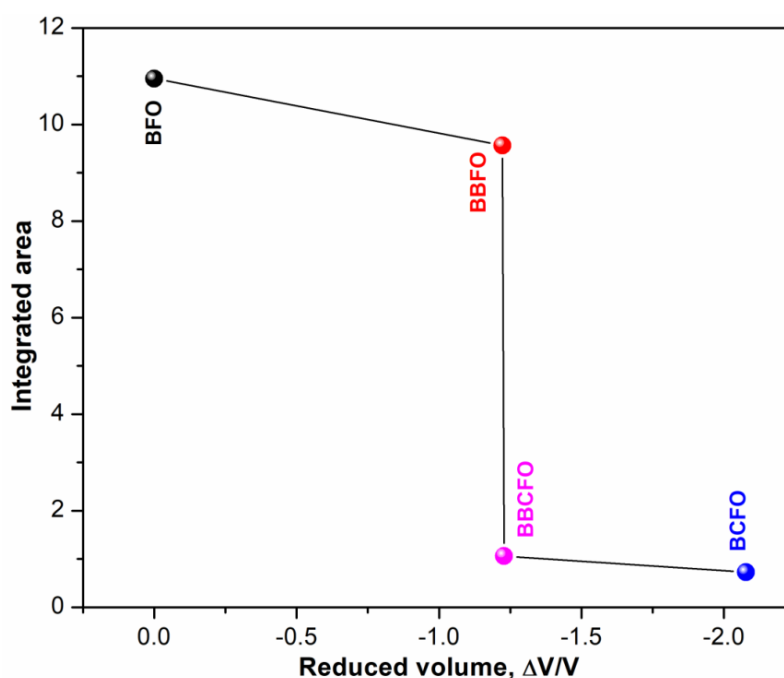


Figure 5.5 A plot of spectral weight of the samples with reduced unit cell volume

Further, the mode intensity of SWEs is investigated with respect to doping. For this, the spectral weight of the studied samples in the frequency range from 32-62 cm^{-1} is plotted

against reduced unit cell volume, as shown in Figure 5.5. It is observed that while the spectral weight of the BBFO sample is comparable to that of the pristine sample, there is a substantial decrease in the spectral weight to a bare minimum in BBCFO and BCFO. This suppression of SWEs in the Ca-based samples is attributed to the increased anharmonicity of the spin cycloid since the SWE mode intensity is related to anharmonicity of spin cycloid [11]. From this, it is understood that the Ca-based samples point to an increase in anharmonicity to a greater extent. This is understood from the doping induced increase in SIA, which incorporates anharmonicity in the spin cycloid. To reiterate, the spin cycloid in bismuth ferrite effectively gets destroyed at ambient conditions through Ca doping due to substantial increase in both the SIA and the anharmonicity of the magnetic cycloid in Ca-based samples. This is also in agreement with the improved magnetic and magnetoelectric properties observed for the studied Ca-based samples [12,13].

5.3.2.2. Raman measurements

The SWE modes that occur below 30 cm^{-1} and not covered by our infrared measurements of the studied samples have been instead explored through low-frequency Raman scattering experiments. Figure 5.6 illustrates the Raman scattering spectra of the pristine and doped BFO ceramics in the frequency range from 6 to 60 cm^{-1} . The absorption features are clearly noticed at very low-frequency in all the studied samples, which are due to the SWEs. The absorption features corresponding to the pristine bismuth ferrite match with the theoretical spectrum [Fishman, 2015]. It is noticed that there is a dramatic change in the mode behavior of SWEs with doping. Noticeably, the scattering intensity of SWEs gets substantially reduced in the doped samples and is minimum in the case of the Ca doped sample. These SWE modes have been further deconvoluted by fitting the spectra with Gaussian lineshapes. Figure 5.7 displays the curve-fitted Raman spectra of the pristine and doped ceramic samples. Here, we have considered an exponential background (see Figure

7) in order to take care of the Rayleigh line effect on the spectra, as the tail of the Rayleigh line gets convoluted with the low frequency SW modes.

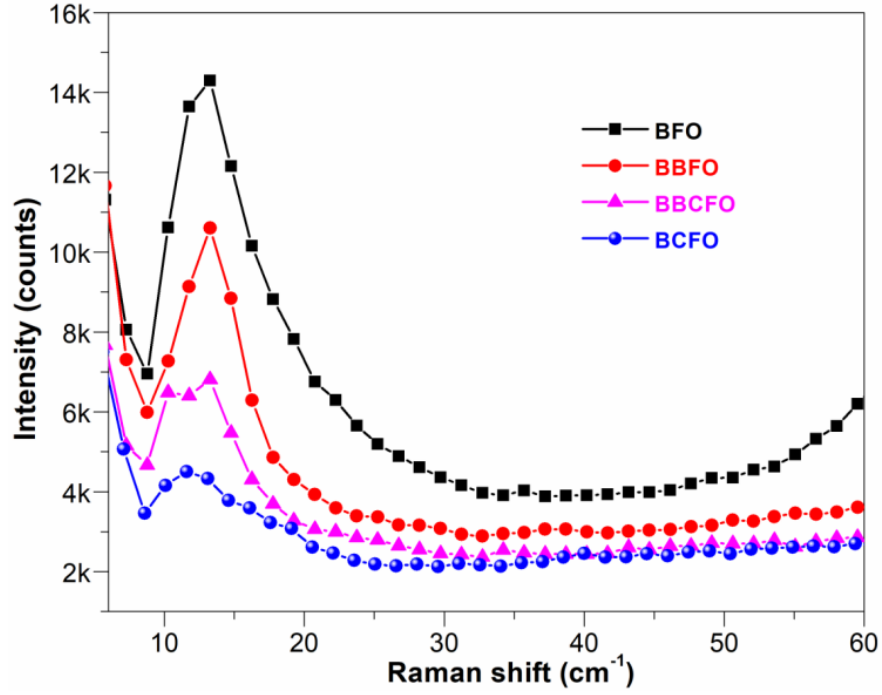


Figure 5.6 Low-frequency Raman measurements.

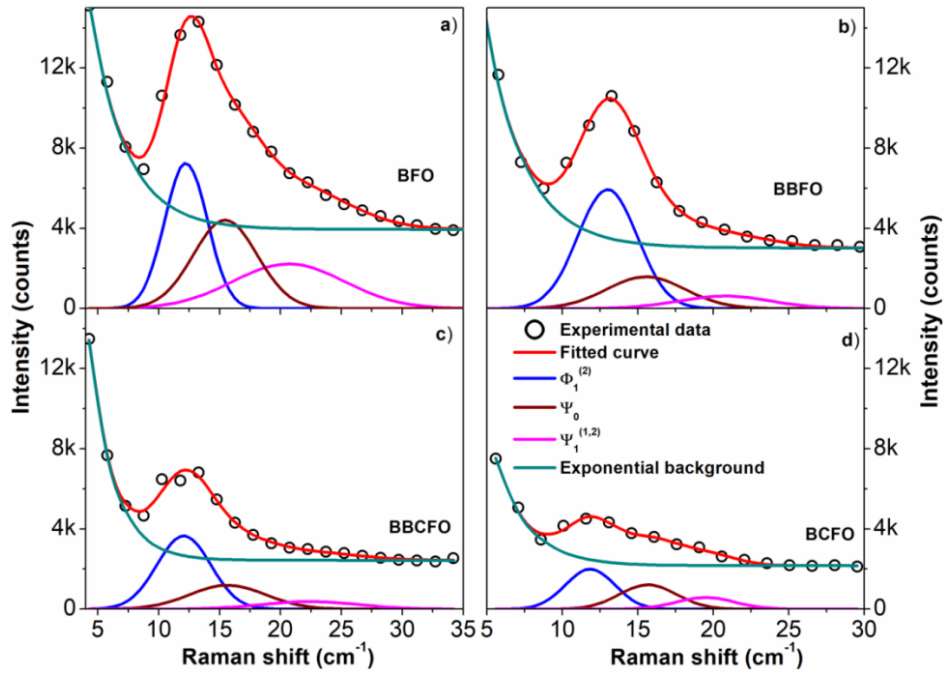


Figure 5.7 Fitted low-frequency Raman spectra of (a) BFO, (b) BBFO, (c) BBCFO and (d) BCFO with Gaussian line shapes.

The extracted mode frequencies of SWEs from the fitting are found to be 12.2, 15.4 and 20.6 cm^{-1} for the pristine sample. These frequencies are assigned with their cyclon and

extracyclon modes as $\Phi_1^{(2)}$, Ψ_0 and $\Psi_1^{(1,2)}$, respectively, based on the reported SWE mode frequency in the literature [57]. The SWE mode frequencies obtained from both the Raman and infrared measurements of the pristine sample are fitted to the cyclon and extracyclon energies as given by the equations $E_c = m\varepsilon_c$ and $E_{exc} = (m^2 + 1)^{1/2}\varepsilon_c$, respectively (see Figure 5.8a), where, ε_c is the cyclon energy. From the fits, ε_c values are found to be 13.7 and 14.8 cm^{-1} for cyclon and extracyclon modes, respectively. The reason for getting two values of cyclon energies is the lifting of degeneracy of $\Phi_1^{(2)}$ and Ψ_0 modes, brought about by SIA in the pristine sample [57]. Due to the limited resolution (1.5 cm^{-1}) of the Raman spectra, we have fitted the degenerate $\Psi_1^{(1,2)}$ mode with one component in the case of doped sample.

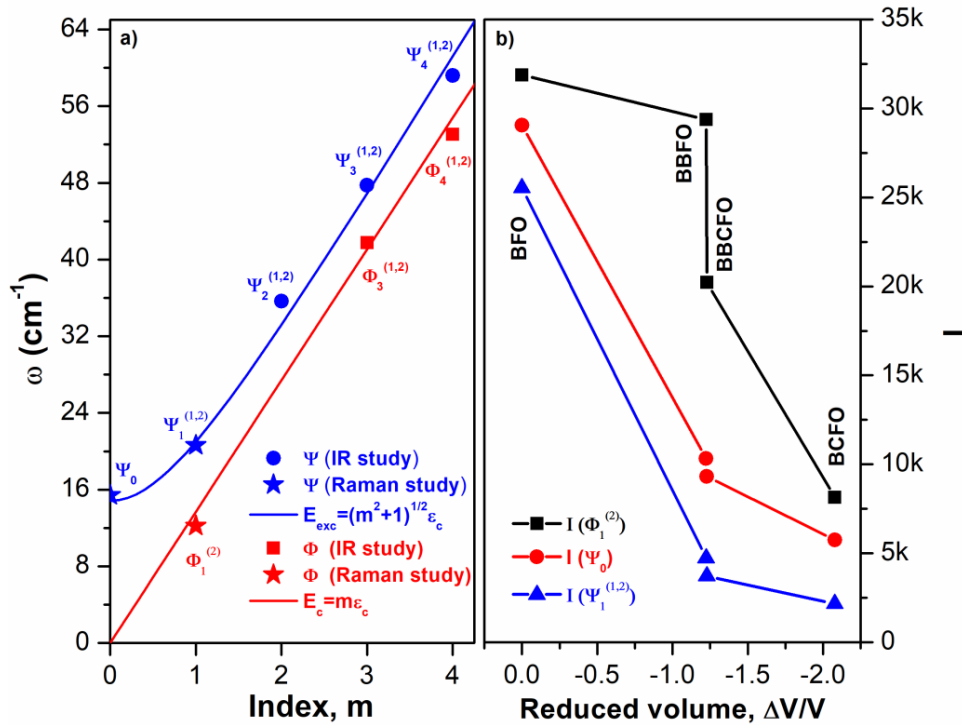


Figure 5.8 (a) Index plot of SWE mode frequencies obtained from infrared and Raman measurements for pristine sample, which are fitted with cyclon and extracyclon energies. (b) A plot of integrated intensity, I , of SWEs with reduced unit cell volume.

Next, we take a closer look at the variation of the SWE mode intensities in the studied samples. Figure 5.8b displays the integrated intensity (I) of SWEs versus reduced

unit cell volume. The intensity of the $\Phi_1^{(2)}$ mode is found to have a dramatic decrease in Ca-based samples while it only decreases to a lesser extent in BBFO sample. On the other hand, the intensity of the other two SWE modes show a gradual decrease with decreasing $\Delta V/V$. It is thus seen that these SWE modes undergo maximum suppression in Ca-based samples while only partially so in the Ba doped sample. Besides, the trend of the integrated intensity of the SWE modes seen from Raman data is almost similar to the observed trend in spectral weight variation from infrared measurements. Thus, Ca-doping in BFO lattice suppresses the SWE modes, which results from the increase SIA and anharmonicity of the cycloid in the Ca-based samples, as already argued. This results in the destruction of the spin cycloid leading to improvement in the magnetic and magnetoelectric properties [95]. Hence, we can infer from this study that the desirable low temperature effect on SWEs of pristine BiFeO₃ can be readily and more effectively achieved at room temperature itself through Ca-substitution at Bi site. Lastly, the Ca-based BFO samples can be proposed as suitable candidates in the field of multiferroics for device application purposes.

In summary, this study provides a direct evidence of near-complete suppression of SWEs by substitution of Ca at Bi-site in BiFeO₃. In other words, Ca doping induces both large single-ion anisotropy as well as increase in the anharmonicity of the spin cycloid, which eventually lead to lifting of degeneracy and suppression of SWEs.

5.4. Conclusion

Room temperature infrared and Raman investigations of pristine and doped BiFeO₃, Bi_{0.9}A_{0.1}FeO_{2.95} (A = Ba, Ca), ceramic samples are carried out to understand the doping effect on phonon and spin wave excitation modes. We observed that the doping induced chemical pressure plays a vital role in BiFeO₃ lattice, which is manifested through the correlated change in phonon behavior with reduced unit cell volume in the Ca-doped sample. On the other hand, the spin wave excitation modes are observed in all the studied

samples, which we could assign with cyclon and extracyclon modes. We noticed a near-complete suppression and complete removal degeneracy of SWEs in Ca-based samples, which is attributed to an increase in anharmonicity of the spin cycloid and single ion anisotropy in these systems. This is also in agreement with the improved magnetic and magnetoelectric property observed in the Ca-based samples. This study, in essence, reveals that the local structure and magnetic interactions can be effectively altered to our advantage through Ca-doping at the Bi site of BiFeO₃ lattice.

Chapter 6

Ferroelectric and magnetic properties of pristine and doped BiFeO₃ through PFM and MFM measurements

In this chapter, we have investigated the ferroelectric and magnetic properties of the studied samples through PFM and MFM measurements.

6.1. Introduction

BiFeO₃ undergoes a transition from paraelectric to ferroelectric phase at a Curie temperature of 1100 K [60], accompanied by the onset of the polarization along the $\langle 111 \rangle_{pc}$ pseudo cubic direction because of stereochemical activity of the lone-pair electrons over Bi³⁺ ion leading to polar atomic displacement along that direction and anti-phase tilting of the adjacent FeO₆ octahedra [29, 30]. Increase interest in the ferroelectric property in this material is due to high spontaneous polarization (P_s) value of 90 $\mu\text{C}/\text{cm}^2$ predicted through ab-initio calculations [8, 30]. Experimentally observed values are 40 $\mu\text{C}/\text{cm}^2$ in bulk ceramic form [142], and 90–150 $\mu\text{C}/\text{cm}^2$ in thin film form [143, 144]. Therefore BiFeO₃ acts as a potential candidate for applications as lead-free memory devices, high temperature piezoelectric sensor and so on.

From the recent magnetic studies, our ceramic BiFeO₃ sample was found to have weak ferromagnetic order at low-temperature [60, 95]. This improvement in the magnetic property was understood through the destruction of the cycloidal spin structure driven by an increase in SIA and anharmonicity of the spin cycloid [45], as was evidenced from the direct observation of a partial suppression of the spin wave excitations from our far-infrared reflectance measurements at low temperature [145]. In addition, the studies on Bi_{0.9}A_{0.1}FeO_{2.95} (A = Ba, Ca) revealed that Ca and the Ba/Ca co-doped sample show improved magnetic and magnetoelectric properties [62, 64]. This is also evident through the

near-complete suppression of spin wave excitations observed in our far-infrared data on Ca and co-doped samples brought about by the destruction of the spin cyloid via doping [146].

In this chapter, we present the results of extensive piezoelectric force microscopy (PFM) and magnetic force microscopy (MFM) studies that we carried out on $\text{Bi}_{0.9}\text{A}_{0.1}\text{FeO}_{2.95}$ ($\text{A} = \text{Ba}, \text{Ca}$). All the samples were found to have piezoelectric response. We have acquired mag and phase images for all the samples. The obtained symmetric loops (phase and mag) due to switching of electric polarization suggests the ferroelectric behavior of the sample. From MFM measurements, the Ca-doped BiFeO_3 sample among all is found to have improved magnetic properties as compared to its pristine counterpart.

6.2. Experimental

Piezoresponse force microscopy (PFM) images of pristine and doped BFO samples were acquired using a scanning probe microscope (SPM) (NT-MDT, NTEGRA, Russia). An electrically conductive tip (A diamond-like carbon coated stiff cantilever ($100 \times 35 \times 2 \mu\text{m}$) having a stiffness constant $k=12 \text{ N/m}$ with resonance frequency $=250 \text{ kHz}$) is subjected to an ac bias voltage ($V_{\text{ac}}\cos(\omega t)$), was used for measuring the piezoelectric response in the contact mode in PFM measurements. The piezoelectric domains get locally elongated or contracted on application of the tip voltage as an effect of inverse piezoelectricity and this results in the deflection of the cantilever. The amplitude (also called ‘mag’) of cantilever deflection is directly proportional to the strength of the piezoresponse. A lock-in amplifier is used to deconvolute the signal obtained from the position sensitive detector to measure the magnitude and phase difference with respect to the input AC voltage (0.3 V). The ‘phase’ part of the signal represents the orientation of the piezoelectric domains. Piezoresponse spectroscopy experiments were carried out in a voltage range of +20 to -20 V to see ferroelectric switching behavior of each sample. MFM studies were carried out by using a silicon probe, whose tip is coated with magnetic cobalt chromium (CoCr) for ideal magnetic

characterization of the samples. The tip having a radius of 25-35 nm and resonant frequency of 40 kHz has a nominal coercivity of 0.04 T , magnetic moment of 10^{-13} emu and stiffness constant of 2.8 N/m.

6.3. Results and discussion

6.3.1. PFM studies on pristine BiFeO₃ ceramic pellet

The ferroelectric properties of BiFeO₃ sample has been investigated through Piezo force microscopy (PFM) measurements. Figure 6.1 displays the topography, mag and phase images of pristine BFO ceramic sample (scan area~15×15 μm^2) obtained at a few selected dc voltages i.e. 0, 1, 5, 10, 0, -1, -5, -10 and 0 V (the voltages are selected to complete the hysteresis cyclic order). In the PFM phase image of the BiFeO₃, the Piezo-domains, which get polarized in perpendicularly upward and downward directions, are shown by bright and dark contrasts, respectively. Dark and bright regions seen in mag image represent the strength of piezoelectricity. Well defined piezoelectric domains are clearly observed in mag and phase images (See Figure 6.1) at $V_{dc}=0$ V. Similarly, different orientations of various domains are observed as contrast in phase images. The evolution of these domains have been followed as a function of dc voltage. While, we did not observe any significant changes in surface morphology, dramatic changes were seen in the mag and phase images. We were able to locate a number of piezoelectric domains ranging from micron to nanometer size (see the highlighted portion of the mag and phase images by the loops with respect to applied voltage in Figure 6.1), which showed significant changes with applied dc voltage. First, let us consider variation in V_{dc} from 1 to 10 V. For $V_{dc}=1$ V, all of these ferroelectric domains show no change, whereas there is a noticeable change seen in both phase and mag images for $V_{dc}=5$ V. Notice that, the two domains highlighted (Figure 6.1) by the yellow colored loops in phase and mag images at 5 V become brighter and darker, respectively, while they don't show further change at 10 V. The other two domains highlighted with white colored

loops are noticed to have significant changes at 10 V (the domains seen in phase and mag images become correspondingly brighter and darker, respectively).

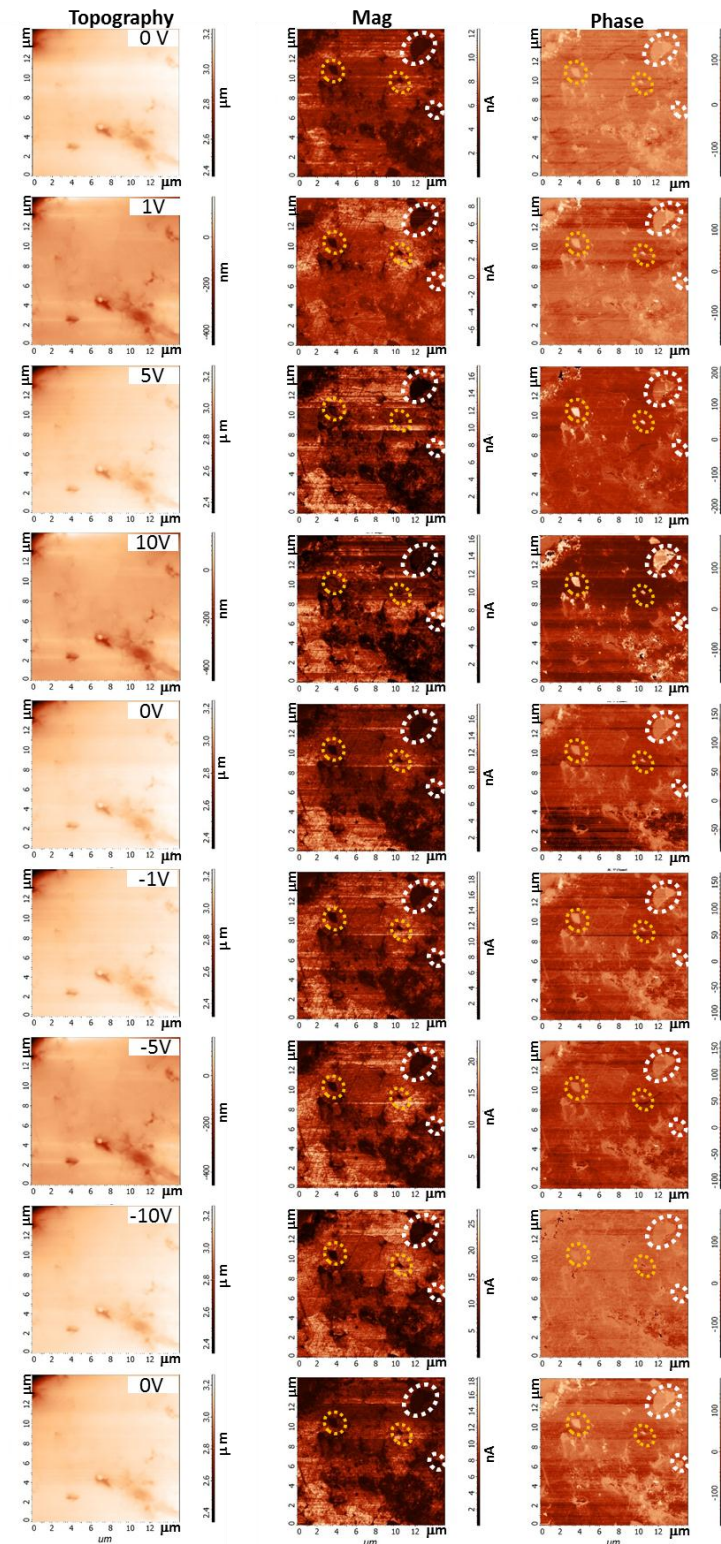


Figure 6.1 Topography, mag and phase images of BFO sample at a few selected dc voltages. The yellow and white dotted loops are the regions of magnetic domains which show noticeable changes with applied dc voltage.

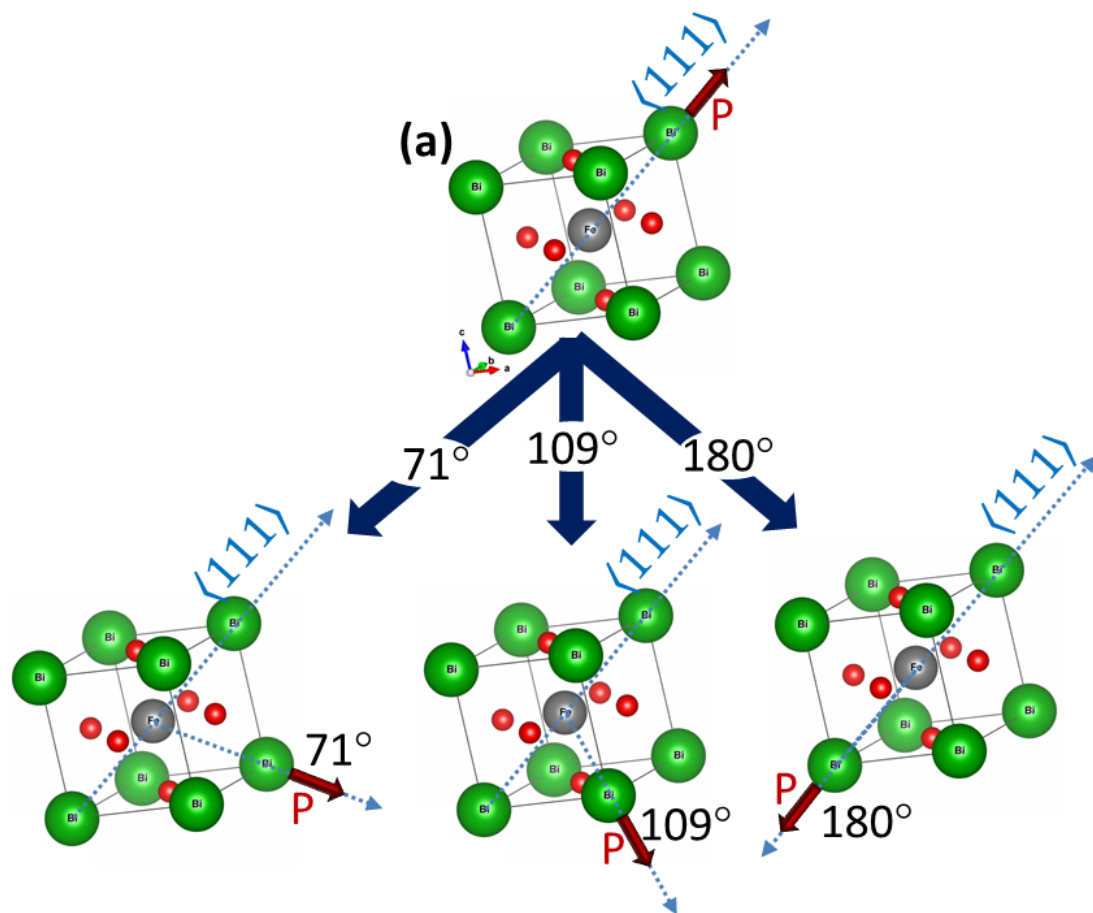


Figure 6.2 Schematic of 71° , 109° and 180° domain switching in rhombohedral BiFeO_3 .

Further, the evolution of the piezoelectric domains have been followed with respect to applied negative dc voltage, where we could find correlated changes. Thus, the domains highlighted by yellow loops undergo switching at an applied dc voltage of 5 V, whereas the domains highlighted by white loops undergo switching at an applied dc voltage of 10 V. Correlations observed in PFM images are described further in relation to different possible switching angles. In the rhombohedral BiFeO_3 , there are three possible switching of ferroelectric domains, which are at an angle 71° , 109° and 180° with the polarization direction along $\langle 111 \rangle_{pc}$ [147, 148] as shown in the Figure 6.2. As our sample is polycrystalline, the ferroelectric domains are randomly oriented. The underlying principle

and the phenomenon of switching a ferroelectric domain in BiFeO₃ through applying electrical energy are as follows [147].

1. The applied electrical energy needs to overcome the energy barrier associated with polarization and stress energy of the ferroelectric domain and its surrounding domains.
2. Larger the applied electric field, larger is the switching angle i.e. the domain with larger switching angle requires ample amount of electrical energy for switching as the polarization vector undergoes a larger rotation. Whereas the smaller switching angle domain needs lesser amount of electrical energy as the polarization vector rotates through a smaller angle. Therefore, as we go from 71°- 109°-180°-ferroelectric domains, the applied electrical energy needed for switching also increases accordingly.
3. The stress energy associated with a switched domain depends on switching angle for that domain. The 180°-switched domain is free from residual stress as the lattice distortion is same for initial and final state of 180° switching, while 109° and 180°-switched domains are associated with additional stress.

Therefore, the domains which showed switching at 5 V can be assigned to either 71° or 109°-type of ferroelectric domain as it requires lesser electrical energy to switch. Whereas those domains that undergo switching at 10 V are 180°-type of ferroelectric domains as they require relatively more electrical energy to switch.

6.3.1.1. Piezoresponse force spectroscopy

Having observed the switching of domains, we have carried out piezoresponse force spectroscopy to obtain phase and mag loops in the sample using a continuously varying dc voltage between -10 to +10 V in steps of 0.1 V. Figure 6.3 shows the phase and mag loop of pristine BFO ceramic sample in the applied voltage range from -6 to +10 V in forward

and backward sweep. In the case of both positive and negative sweep, the piezoresponse is found to increase with increasing applied voltage. We were able to acquire almost symmetrical ferroelectric mag loop (i.e. close to perfect butterfly loop) and corresponding symmetrical phase loop. In general, the piezoresponse in a material is due to the sum total of piezoresponses from the spontaneous polarization and the induced polarization through applied voltage. The clear hysteresis behavior observed in phase and mag loop signify that the obtained piezoresponse is because of the ferroelectric behavior. Therefore the symmetrical mag and phase loops demonstrate the ferroelectric behavior of the pristine BiFeO₃ sample.

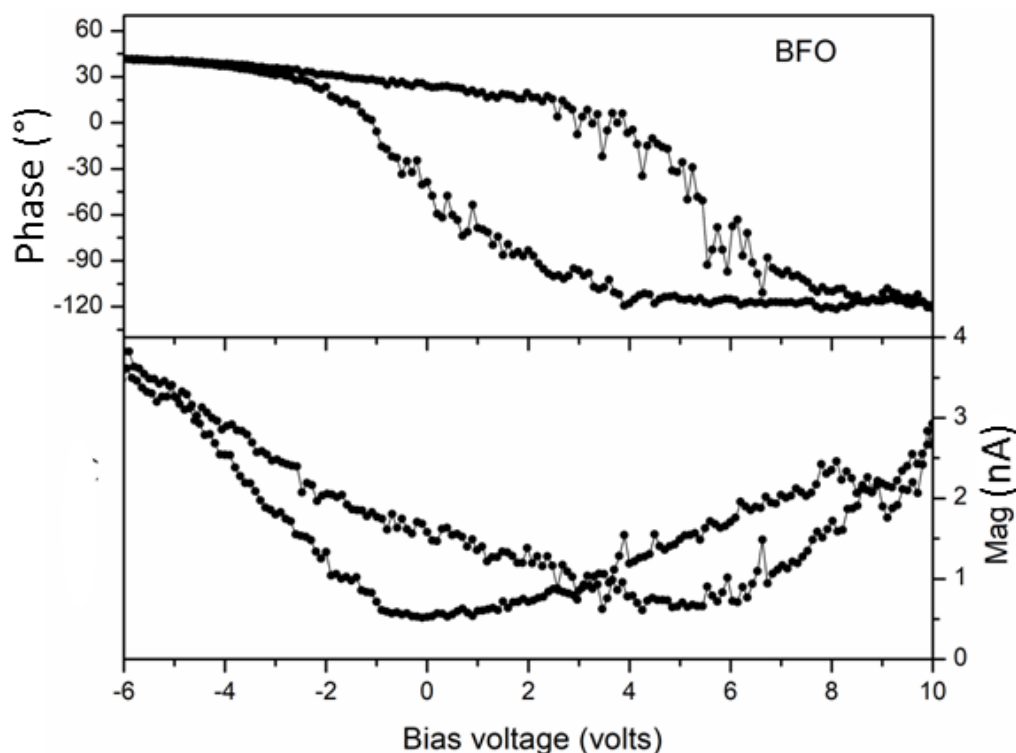


Figure 6.3 Phase and mag loops of pristine BFO sample.

6.3.1.2. Calculation of piezoelectric coefficient (d_{33})

The piezoelectric coefficient of a material is a measure of response to applied electric field. Here, the longitudinal piezoelectric response is denoted as ' d_{33} ', where both electric field and piezoelectric response are in z-direction. The d_{33} value has been calculated by using the piezoresponse force spectroscopy corresponding to $V_{dc} = 0$ V. In a typical PFM, the

modulation voltage V_{ac} , which is applied between the tip and the ferroelectric material, leads to a vertical displacement of the tip. Since the tip is in mechanical contact with the sample surface, it precisely follows the piezoforce from the sample surface. In the present study, the applied voltage on the microcrystals generates deformation i.e. elongation or contraction of the microcrystal. The piezoelectric coefficient d_{33} has been calculated by using the formula

$$d_{33} = \Delta S_z / E_z \quad (6.1)$$

where $E_z = V_{ac}/z$ and $\Delta S_z = \Delta z/z$ is the change of strain along the z-direction. Using the values of E_z and ΔS_z in equation (6.1), d_{33} can be written as

$$d_{33} = \Delta z / V_{ac} \quad (6.2)$$

In PFM measurements, the magnitude of the tip vibration measured by the lock-in amplifier technique gives information on the piezoelectric strain. Therefore, the piezoelectric coefficient, d_{33} , can be determined by using the formula as described in equation (6.2). The value of d_{33} determined over a number of polar domains was found to be 70-80 pm/V. Below, we have listed the reported d_{33} values of BiFeO₃ in various forms of sample and compared with the value obtained from the present study (Table 6.1). The obtained d_{33} value is close to the reported value for polycrystalline BiFeO₃ sample [142].

Table 6.1 Comparison of the reported d_{33} value of BiFeO₃ with the present work

Material	Piezoelectric Co-efficient
BFO nanowire	22.21 pm/V (max) [149]
BFO thin film	46 pm/V for 150 nm film to 8 pm/V for 6 nm film [150] 60 pm / V for ≥ 100 nm film [151] 17 pm/V [152]
BFO polycrystalline ceramics	50-60 pm/V [142]
BFO polycrystalline ceramics	70-80 pm/V (present work)

Further, we have analyzed the ferroelectric behavior of the doped samples through PFM measurements to understand the doping effect on ferroelectric behavior.

6.3.2. PFM studies on 10% Ba doped BiFeO₃ ceramic pellet

Figure 6.4 displays the topography, mag and phase images of Ba-doped BiFeO₃ sample at a few selected dc voltages in a cyclic order to understand the hysteresis behavior (i.e., at 0, 1, 5, 10, 0, -1, -5, -10 and 0 V). The piezoelectric domains are clearly observed in phase and mag images, which gives evidence of the piezoelectric behavior of the Ba-doped sample. PFM phase images clearly depicted the spatial distribution of piezo domains which are randomly oriented.

Next, we have followed their evolution with respect to applied positive and negative dc voltages to understand the switching behavior in this sample. It is clearly noticed that the observed piezoelectric domains show switching behavior through the reversing of the applied dc voltage. This gives evidence of the ferroelectric behavior in the sample. We have specifically followed a few selected ferroelectric domains (see the domains highlighted with loops) with respect to applied dc voltage. The domains highlighted by yellow colored loops show switching at 5 V and thus these are either 71° or 109°-ferroelectric domains, whereas the domains shown by white loops show switching at 10 V and hence, these domains are 180°-ferroelectric domains.

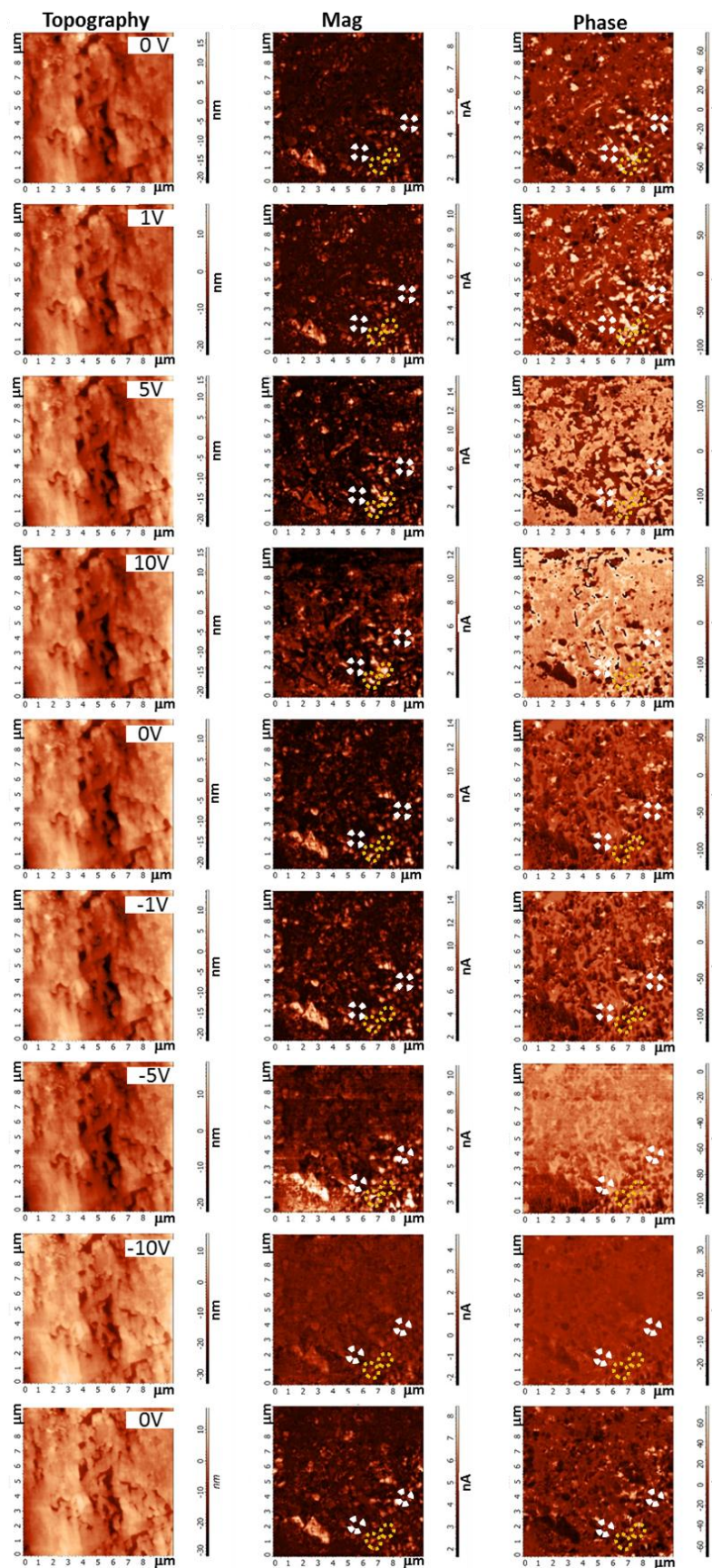


Figure 6.4 Topography, mag and phase images of BBFO at a few selected dc voltages. The yellow and white dotted loops are the regions of magnetic domains which show noticeable changes with applied dc voltage.

Ferroelectric nature of the Ba-doped sample is further confirmed through piezoresponse force spectroscopy, discussed below.

6.3.2.1. Piezoresponse force spectroscopy

Figure 6.5 displays the phase and mag loops of the Ba-doped sample obtained in the voltage range from -15 to +15 V. Here again, we were able to acquire nearly symmetric phase and mag loops. It is observed from the phase loop that the piezoelectric domain clearly shows the switching of the polarization by reversing the applied dc voltage and the hysteresis behavior of the domain. The mag loop illustrates the saturation and hysteresis behavior of the domains. Thus, the piezoresponse force spectroscopy clearly gives evidence of ferroelectric nature of the Ba-doped BiFeO₃ sample.

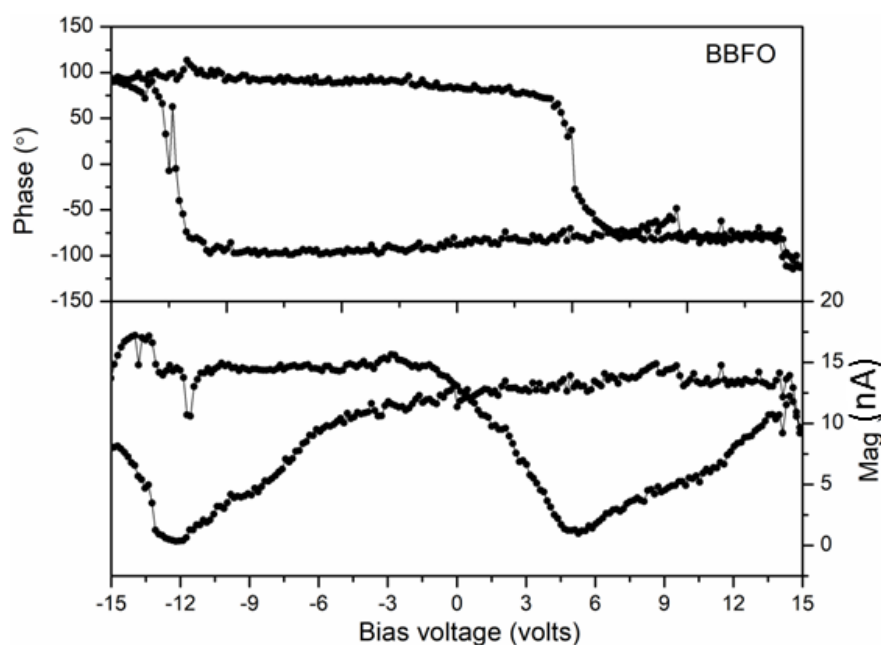


Figure 6.5 Phase and mag loops of Ba-doped BFO sample.

The piezoelectric coefficient, d_{33} , has been determined by using the formula as described in the equation (6.2). The d_{33} value determined over a number of polar domains was found to be 70-80 pm/V, which is similar to the d_{33} value observed in pristine sample. Although, the lone pair over Bi³⁺ ion is responsible for ferroelectric property, it is seen that 10% Ba doping at Bi site has not hampered the ferroelectric property of BiFeO₃. This may

be due to the larger ionic radius of Ba^{2+} ion compared to that of Bi^{3+} ion, which helps in preserving the ferroelectric property.

6.3.3. PFM studies on 5 % Ba and 5 % Ca co-doped BiFeO_3 ceramic pellet

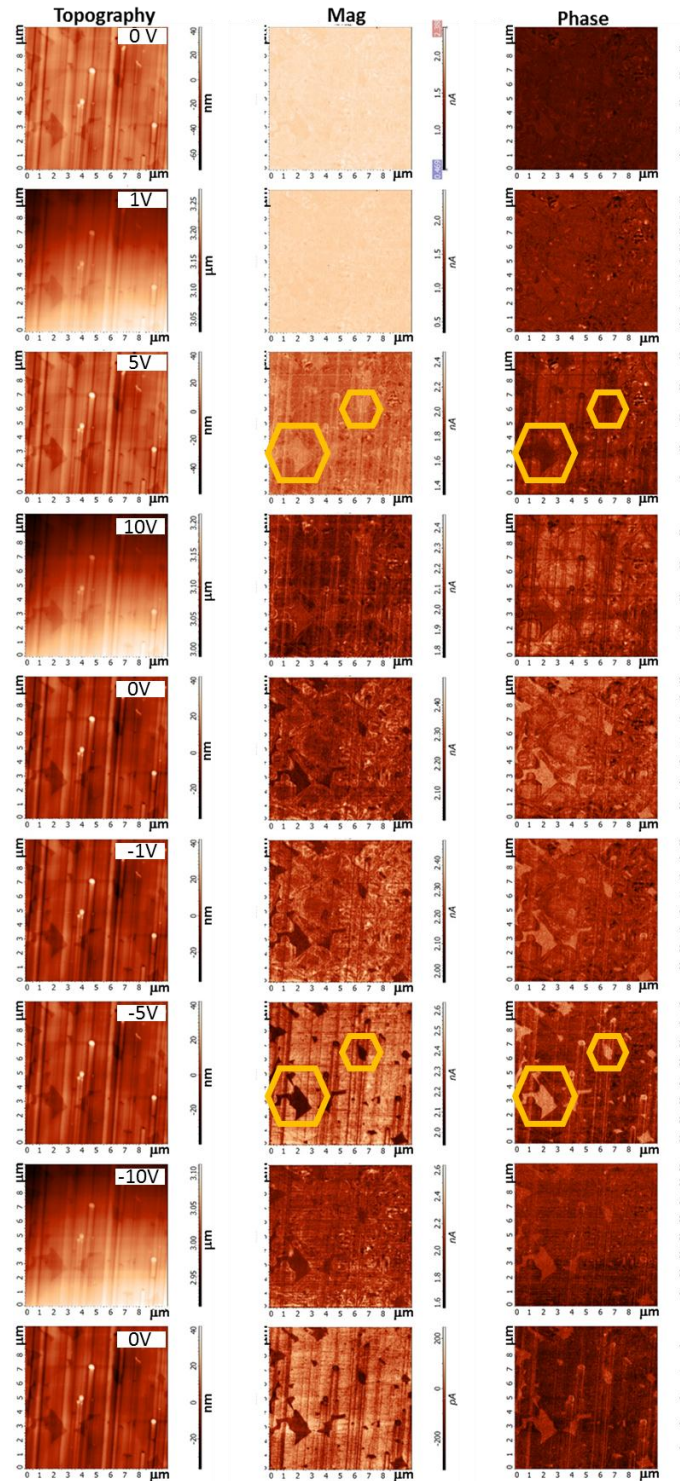


Figure 6.6 Topography, mag and phase images of BBCFO at few selected dc voltages. Yellow colored loops point to the region of piezo-domains showing polarization switching between +5 V and -5 V.

The topography, mag and phase images of co-doped BFO sample are shown in Figure 6.6 for various applied dc voltages (0, 1, 5, 10, 0, -1, -5, -10 and 0 V). The acquired PFM images clearly show piezoelectric domains. It is also observed that these domains show evolution with respect to applied dc voltages. If we compare the phase and mag image at a dc voltage of 5 and -5 V, the dark contrast of piezo domains shown by the hexagon yellow color in the phase image at 5 V got changed to bright contrast at -5 V. This shows the polarization switching of piezo domains, which gives evidence of the ferroelectric nature of the sample. The ferroelectric property of the co-doped sample is further investigated through piezoresponse spectroscopy measurements.

6.3.3.1. Piezoresponse force spectroscopy

Figure 6.7 displays the phase and mag loops of the Ba-Ca codoped sample from PFM measurements. We were able to get switching as well as characteristic hysteresis behavior of the polar domains (see phase loop of Figure 6.7). The mag loop shows saturation of the polarization as well as hysteresis behavior of the co-doped sample. Thus, the phase and mag loops give evidence for the existence of ferroelectricity in the co-doped sample.

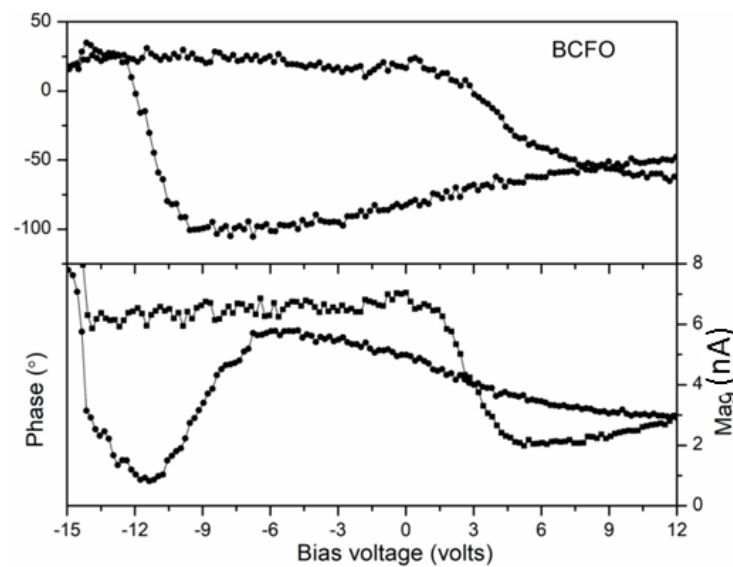


Figure 6.7 Phase and mag loops of Ba-Ca co-doped BFO sample.

The piezoelectric coefficient, d_{33} , of the co-doped sample determined by using equation (6.2), was found to be in the range of 15-20 pm/V. This shows that the ferroelectric

property is substantially weakened in the co-doped sample. Since we have already seen that Ba doping at Bi^{3+} site does not hamper ferroelectricity much, the main reason for the reduction of the ferroelectric property in the co-doped sample is mainly because of the substitution of 5 % Ca^{2+} ion at Bi^{3+} site.

6.3.4. PFM studies on 10 % Ca-doped BiFeO_3 ceramic pellet

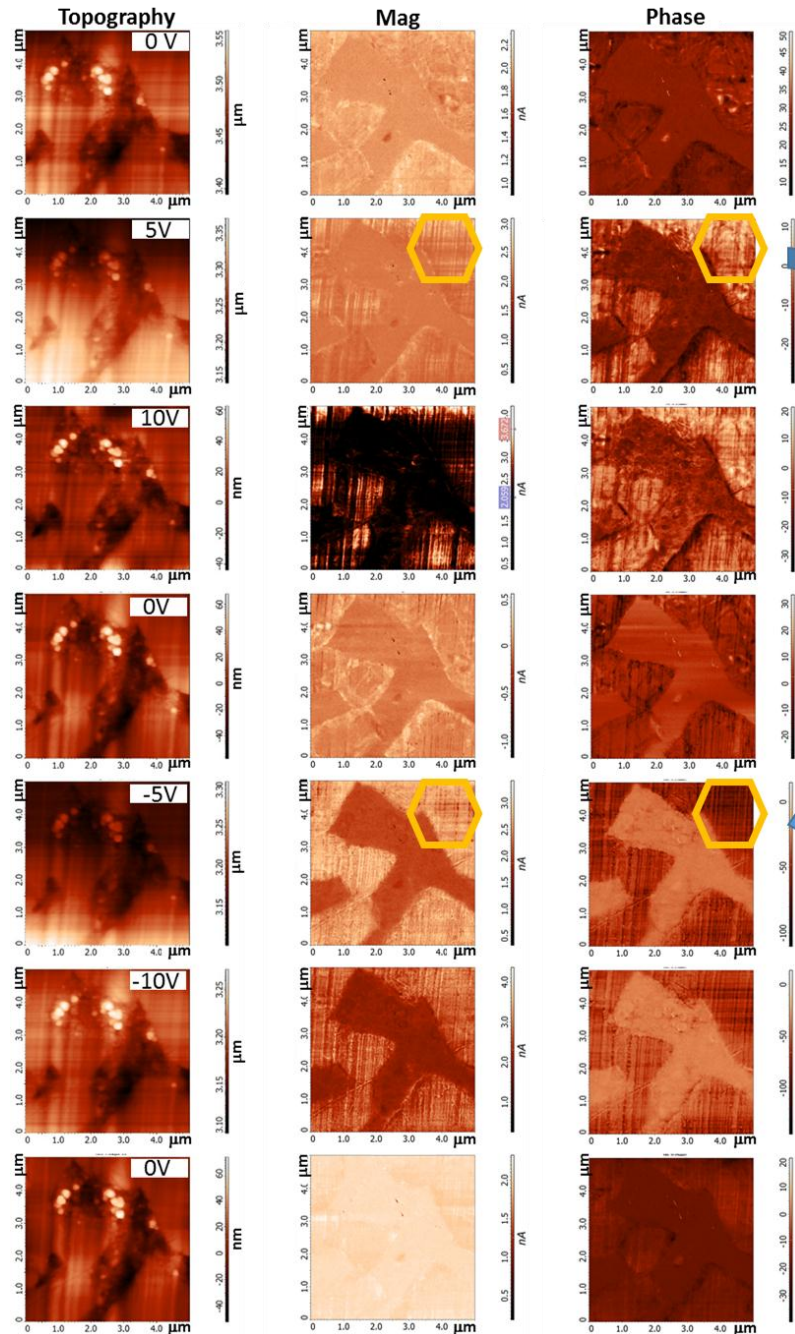


Figure 6.8 Topography, mag and phase images of BCFO at a few selected dc voltages. Yellow colored loops point to the region of piezo-domains showing polarization switching between +5 V and -5 V.

We have also acquired the PFM images of the Ca-doped sample at different applied voltages (0, 5, 10, 0, -5, -10 and 0 V), which are displayed in Figure 6.8. The piezoelectric domains are observed both in the phase and mag images. These domains are found to evolve with applied dc voltage. For switching behavior, we have compared phase and mag images of the sample at +5 and -5 V. The contrast of the region shown by the yellow color hexagon (Figure 6.8) gets changed from 5 to -5 V, i.e. from bright to dark. This shows the switching behavior of the polarization with voltage, which gives evidence of the ferroelectric property of the Ca-doped sample. Further, we have investigated the ferroelectric property of the Ca-doped sample through piezoresponse force spectroscopy.

6.3.4.1. Piezoresponse force spectroscopy

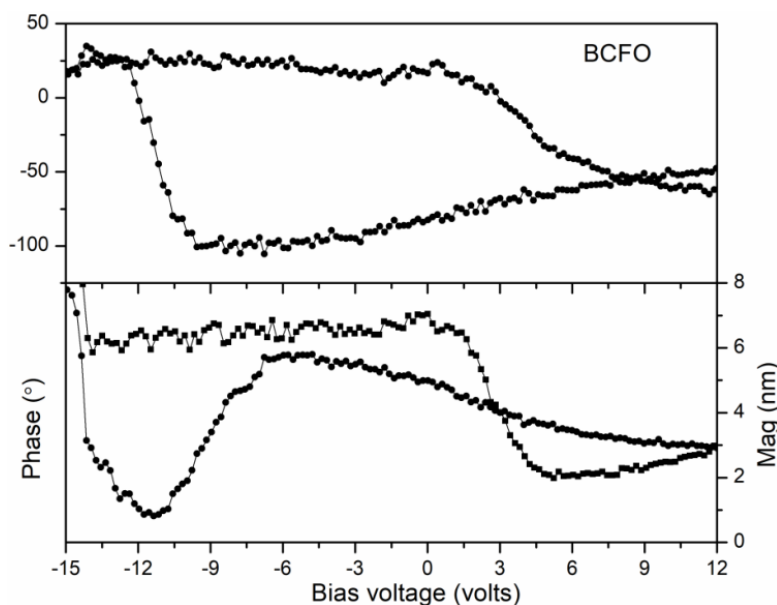


Figure 6.9 Phase and mag loops of Ca-doped BFO sample.

Figure 6.9 displays the phase and mag loops through PFM measurements. It is noticed that the piezoelectric domain shows switching behavior with bias voltage and characteristic hysteresis property (see phase loop of Figure 6.9). On the other hand, the mag loop is slightly distorted, which could be due to the different orientations of the ferroelectric domains. However, the mag loop shows hysteresis and saturation behavior of the electric polarization. Thus, the piezoresponse force spectroscopy clearly depicts the ferroelectric

property of the Ca-doped sample. The d_{33} value calculated for the Ca-doped sample using equation 6.2 is found to be 15-20 pm/V. Here, the ferroelectric property of the Ca-doped sample is similar to that of co-doped sample, which is significantly reduced on account of Ca doping.

From the PFM measurements, the studied samples are all found to be ferroelectric to different degrees. In particular, Ca^{2+} doping at Bi^{3+} site significantly reduces the ferroelectric property, as the lone pair of Bi^{3+} ion is responsible for ferroelectricity. However Ba^{2+} doping doesn't alter the ferroelectric property, which is due to the larger ionic radius of Ba^{2+} ion compared to that of Bi^{3+} .

6.3.5. MFM studies

The magnetic properties of both the pristine and the doped samples have been investigated through magnetic force microscopy (MFM) measurements. First we have investigated the magnetic behavior of a hard disk through MFM studies and then compared with the magnetic properties of the studied samples. Figure 6.10 displays MFM phase image of hard disk. In the MFM phase image of the hard disk, the magnetic domains, which get magnetized in perpendicularly upward and downward directions, are shown by red and blue colored fringes, respectively, while the magnetic domains which get magnetized along the plane of the hard disk, are shown in green color.

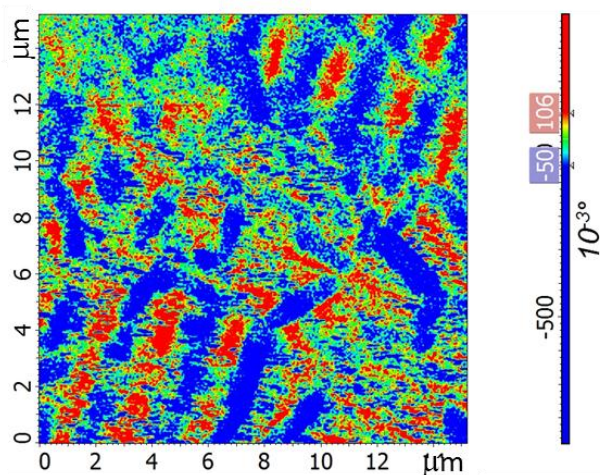


Figure 6.10 MFM image a commercial hard disk.

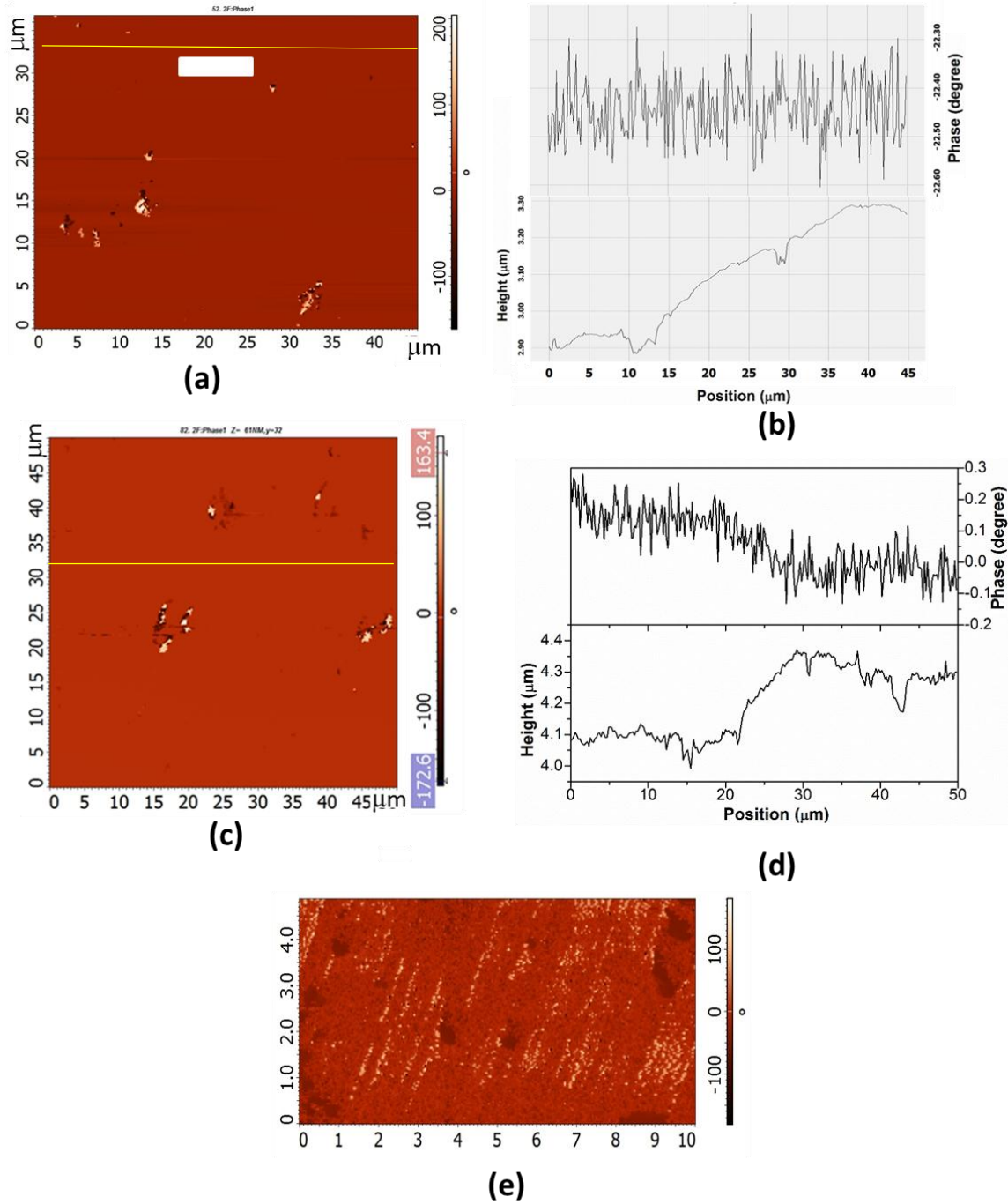


Figure 6.11 (a) MFM image and (b) the corresponding line profile of phase and height BFO sample at $y=35 \mu\text{m}$. (c) MFM image and (d) the corresponding line profile of phase and height BCFO sample at $y=32 \mu\text{m}$ (e) Expanded region of figure 6.11c showing bright and dark fringes.

We were able to acquire MFM images of the pristine BFO sample and the 10 % Ca-doped sample, which are displayed in Figures 6.11a and 6.11c, respectively. From the phase image of the pristine sample, we were able to get distinct magnetic domains. From the line profile of the corresponding phase image, the maximum magnitude of the phase deflection

is found to be $\sim 0.1^\circ$, which gives clear indication of the existence of magnetic domains in the pristine sample. Thus, these MFM data point towards a weak magnetic behavior of the sample. On the other hand, we have clearly noticed bright and dark fringes in the phase image of BCFO sample shown in Figure 6.11e. The dark and bright fringes are represented by the magnetic domains magnetized along upward and downward direction of the sample surface. Moreover, the line profile of the corresponding phase image also show clear evidence of the magnetic domains, as the magnitude of the phase deflection of BCFO is $\sim 0.2^\circ$. These observations point to an enhanced magnetism in BCFO sample. This also correlates well with the observed suppression of SWEs in BCFO sample from the infrared measurements indicating improvement in the magnetic property [146].

6.4. Conclusion

The Piezoelectric and magnetic force microscopy studies have been carried out on the pristine and doped BiFeO_3 samples. From the PFM measurements, the distributions of piezoelectric domains are observed in all the studied samples. Moreover, the phase and mag loops of the studied samples obtained from piezoresponse force spectroscopy show switching, saturation and hysteresis behavior. The d_{33} value is calculated from mag loop which is found to be 70-80 pm/V for pristine BiFeO_3 . We have found that the d_{33} values decrease noticeably from the pristine BiFeO_3 case to the Ca-doped case. Concomitantly, the MFM studies on these samples show improved magnetic property for the Ca-doped BiFeO_3 as compared to the pristine sample. These results are in complete agreement with our infrared results, where a suppression of the SWE modes leading to enhanced magnetism in Ca-doped BiFeO_3 was observed.

References

- [1] Schmid H 1994 Multi-ferroic magnetoelectrics *Ferroelectrics* **162** 317-38
- [2] Hill N A 2000 Why Are There so Few Magnetic Ferroelectrics? *The Journal of Physical Chemistry B* **104** 6694-709
- [3] Hur N, Park S, Sharma P A, Ahn J S, Guha S and Cheong S W 2004 Electric polarization reversal and memory in a multiferroic material induced by magnetic fields *Nature* **429** 392-5
- [4] Zheng H, Wang J, Lofland S E, Ma Z, Mohaddes-Ardabili L, Zhao T, Salamanca-Riba L, Shinde S R, Ogale S B, Bai F, Viehland D, Jia Y, Schlom D G, Wuttig M, Roytburd A and Ramesh R 2004 Multiferroic $\text{BaTiO}_3\text{-CoFe}_2\text{O}_4$ Nanostructures *Science* **303** 661-3
- [5] Yun K Y, Ricinschi D, Kanashima T, Noda M and Okuyama M 2004 Giant ferroelectric polarization beyond $150 \mu\text{C}/\text{cm}^2$ in BiFeO_3 thin film *Japanese Journal of Applied Physics, Part 2: Letters* **43** L647-L8
- [6] Fiebig M 2005 Revival of the magnetoelectric effect *Journal of physics D: applied physics* **38** R123
- [7] Ederer C and Spaldin N A 2005 Weak ferromagnetism and magnetoelectric coupling in bismuth ferrite *Physical Review B* **71** 060401
- [8] Neaton J, Ederer C, Waghmare U, Spaldin N and Rabe K 2005 First-principles study of spontaneous polarization in multiferroic Bi Fe O_3 *Physical Review B* **71** 014113
- [9] Zhao T, Scholl A, Zavaliche F, Lee K, Barry M, Doran A, Cruz M P, Chu Y H, Ederer C, Spaldin N A, Das R R, Kim D M, Baek S H, Eom C B and Ramesh R 2006 Electrical control of antiferromagnetic domains in multiferroic BiFeO_3 films at room temperature *Nature Materials* **5** 823-9
- [10] Eerenstein W, Mathur N D and Scott J F 2006 Multiferroic and magnetoelectric materials *Nature* **442** 759-65
- [11] Scott J F 2007 Multiferroic memories *Nature Materials* **6** 256-7
- [12] Cheong S-W and Mostovoy M 2007 Multiferroics: a magnetic twist for ferroelectricity *Nature materials* **6** 13-20
- [13] Catalan G and Scott J F 2009 Physics and applications of bismuth ferrite *Advanced materials* **21** 2463-85
- [14] Seki S, Yu X, Ishiwata S and Tokura Y 2012 Observation of skyrmions in a multiferroic material *Science* **336** 198-201
- [15] Wu J, Fan Z, Xiao D, Zhu J and Wang J 2016 Multiferroic bismuth ferrite-based materials for multifunctional applications: ceramic bulks, thin films and nanostructures *Progress in Materials Science* **84** 335-402
- [16] Sando D, Appert F, Xu B, Paull O, Burns S, Carrétéro C, Dupé B, Garcia V, Gallais Y and Sacuto A 2019 A magnetic phase diagram for nanoscale epitaxial BiFeO_3 films *Applied Physics Reviews* **6** 041404
- [17] Béa H, Gajek M, Bibes M and Barthélémy A 2008 Spintronics with multiferroics *Journal of Physics: Condensed Matter* **20** 434221
- [18] Zvezdin A, Logginov A, Meshkov G and Pyatakov A 2007 Multiferroics: promising materials for microelectronics, spintronics, and sensor technique *Bulletin of the Russian Academy of Sciences: Physics* **71** 1561-2
- [19] Shen J, Cong J, Shang D, Chai Y, Shen S, Zhai K and Sun Y 2016 A multilevel nonvolatile magnetoelectric memory *Scientific reports* **6** 34473
- [20] Gao F, Chen X, Yin K, Dong S, Ren Z, Yuan F, Yu T, Zou Z and Liu J M 2007 Visible-light photocatalytic properties of weak magnetic BiFeO_3 nanoparticles *Advanced materials* **19** 2889-92

-
- [21] Yang S, Martin L, Byrnes S, Conry T, Basu S, Paran D, Reichertz L, Ihlefeld J, Adamo C and Melville A 2009 Photovoltaic effects in BiFeO₃ *Applied Physics Letters* **95** 062909
- [22] Moreau J M, Michel C, Gerson R and James W J 1971 Ferroelectric BiFeO₃ X-ray and neutron diffraction study *Journal of Physics and Chemistry of Solids* **32** 1315-20
- [23] Kubel F and Schmid H 1990 Structure of a ferroelectric and ferroelastic monodomain crystal of the perovskite BiFeO₃ *Acta Crystallographica Section B: Structural Science* **46** 698-702
- [24] Goldschmidt V M 1926 Die Gesetze der Krystallochemie *Naturwissenschaften* **14** 477-85
- [25] Glazer A 1972 The classification of tilted octahedra in perovskites *Acta Crystallographica Section B: Structural Crystallography and Crystal Chemistry* **28** 3384-92
- [26] Glazer A 1975 Simple ways of determining perovskite structures *Acta Crystallographica Section A: Crystal Physics, Diffraction, Theoretical and General Crystallography* **31** 756-62
- [27] Lee S, Zhang J, Torii S, Choi S, Cho D-Y, Kamiyama T, Yu J, McEwen K and Park J-G 2013 Large in-plane deformation of RuO₆ octahedron and ferromagnetism of bulk SrRuO₃ *Journal of Physics: Condensed Matter* **25** 465601
- [28] Stokes H T, Kisi E H, Hatch D M and Howard C J 2002 Group-theoretical analysis of octahedral tilting in ferroelectric perovskites *Acta Crystallographica Section B: Structural Science* **58** 934-8
- [29] Park J-G, Le M D, Jeong J and Lee S 2014 Structure and spin dynamics of multiferroic BiFeO₃ *Journal of Physics: Condensed Matter* **26** 433202
- [30] Ravindran P, Vidya R, Kjekshus A, Fjellvåg H and Eriksson O 2006 Theoretical investigation of magnetoelectric behavior in BiFeO₃ *Physical Review B* **74** 224412
- [31] Diéguez O, González-Vázquez O E, Wojdeł J C and Íñiguez J 2011 First-principles predictions of low-energy phases of multiferroic BiFeO₃ *Physical Review B* **83** 094105
- [32] Moriya T 1960 Anisotropic Superexchange Interaction and Weak Ferromagnetism *Physical Review* **120** 91-8
- [33] Sosnowska I and Zvezdin A K 1995 Origin of the long period magnetic ordering in BiFeO₃ *Journal of Magnetism and Magnetic Materials* **140-144** 167-8
- [34] Ramazanoglu M, Laver M, Ratcliff W, Watson S M, Chen W C, Jackson A, Kothapalli K, Lee S, Cheong S W and Kiryukhin V 2011 Local Weak Ferromagnetism in Single-Crystalline Ferroelectric BiFeO₃ *Physical Review Letters* **107** 207206
- [35] Weingart C, Spaldin N and Bousquet E 2012 Noncollinear magnetism and single-ion anisotropy in multiferroic perovskites *Physical Review B* **86** 094413
- [36] Zalesskii A, Zvezdin A, Frolov A and Bush A 2000 ⁵⁷Fe NMR study of a spatially modulated magnetic structure in BiFeO₃ *Journal of Experimental and Theoretical Physics Letters* **71** 465-8
- [37] Khozev D, Zalessky A, Gippius A, Morozova E and Bush A 2003 Spin modulation of ⁵⁷Fe NMR frequency and relaxation in BiFeO₃ *Physica B: Condensed Matter* **329** 848-9
- [38] Zalesskii A, Frolov A, Zvezdin A, Gippius A, Morozova E, Khozevc D, Bush A and Pokatilov V 2002 Effect of spatial spin modulation on the relaxation and NMR frequencies of ⁵⁷Fe nuclei in a ferroelectric antiferromagnet BiFeO₃ *Journal of Experimental and Theoretical Physics* **95** 101-5
-

-
- [39] Ramazanoglu M, W Ratcliff I, Choi Y J, Lee S, Cheong S-W and Kiryukhin V 2011 Temperature-dependent properties of the magnetic order in single-crystal BiFeO₃ *Physical Review B* **83** 174434
- [40] Sosnowska I and Przeniosło R 2011 Low-temperature evolution of the modulated magnetic structure in the ferroelectric antiferromagnet BiFeO₃ *Physical Review B* **84** 144404
- [41] Palewicz A, Szumiata T, Przeniosło R, Sosnowska I and Margiolaki I 2006 Search for new modulations in the BiFeO₃ structure: SR diffraction and Mössbauer studies *Solid state communications* **140** 359-63
- [42] Landers J, Salamon S, Escobar Castillo M, Lupascu D and Wende H 2014 Mossbauer Study of Temperature-Dependent Cycloidal Ordering in BiFeO₃ Nanoparticles *Nano letters* **14** 6061-5
- [43] Przeniosło R, Regulski M and Sosnowska I 2006 Modulation in multiferroic BiFeO₃: Cycloidal, elliptical or SDW? *Journal of the Physical Society of Japan* **75** 084718-
- [44] Przeniosło R, Palewicz A, Regulski M, Sosnowska I, Ibberson R M and Knight K S 2011 Does the modulated magnetic structure of BiFeO₃ change at low temperatures? *Journal of Physics: Condensed Matter* **23** 279501
- [45] Jeong J, Le M D, Bourges P, Petit S, Furukawa S, Kim S-A, Lee S, Cheong S W and Park J-G 2014 Temperature-Dependent Interplay of Dzyaloshinskii-Moriya Interaction and Single-Ion Anisotropy in Multiferroic BiFeO₃ *Physical Review Letters* **113** 107202
- [46] Nagel U, Fishman R S, Katuwal T, Engelkamp H, Talbayev D, Yi H T, Cheong S W and Rößler T 2013 Terahertz Spectroscopy of Spin Waves in Multiferroic BiFeO₃ in High Magnetic Fields *Physical Review Letters* **110** 257201
- [47] Fishman R S 2013 Field dependence of the spin state and spectroscopic modes of multiferroic BiFeO₃ *Physical Review B* **87** 224419
- [48] Fishman R S, Furukawa N, Haraldsen J T, Matsuda M and Miyahara S 2012 Identifying the spectroscopic modes of multiferroic BiFeO₃ *Physical Review B* **86** 220402
- [49] Fishman R S, Haraldsen J T, Furukawa N and Miyahara S 2013 Spin state and spectroscopic modes of multiferroic BiFeO₃ *Physical Review B* **87** 134416
- [50] Palai R, Schmid H, Scott J and Katiyar R 2010 Raman spectroscopy of single-domain multiferroic BiFeO₃ *Physical Review B* **81** 064110
- [51] Beekman C, Reijnders A, Oh Y, Cheong S-W and Burch K 2012 Raman study of the phonon symmetries in BiFeO₃ single crystals *Physical Review B* **86** 020403
- [52] Hlinka J, Pokorný J, Karimi S and Reaney I 2011 Angular dispersion of oblique phonon modes in BiFeO₃ from micro-Raman scattering *Physical Review B* **83** 020101
- [53] Talkenberger A, Vrejoiu I, Johann F, Röder C, Irmer G, Rafaja D, Schreiber G, Kortus J and Himcinschi C 2015 Raman spectroscopic investigations of epitaxial BiFeO₃ thin films on rare earth scandate substrates *Journal of Raman Spectroscopy* **46** 1245-54
- [54] Talbayev D, Trugman S, Lee S, Yi H T, Cheong S-W and Taylor A 2011 Long-wavelength magnetic and magnetoelectric excitations in the ferroelectric antiferromagnet BiFeO₃ *Physical Review B* **83** 094403
- [55] Cazayous M, Gallais Y, Sacuto A, De Sousa R, Lebeugle D and Colson D 2008 Possible observation of cycloidal electromagnons in BiFeO₃ *Physical review letters* **101** 037601
-

-
- [56] de Sousa R and Moore J E 2008 Optical coupling to spin waves in the cycloidal multiferroic BiFeO₃ *Physical Review B* **77** 012406
- [57] Fishman R S, Lee J H, Bordács S, Kézsmárki I, Nagel U and Room T 2015 Spin-induced polarizations and nonreciprocal directional dichroism of the room-temperature multiferroic BiFeO₃ *Physical Review B* **92** 094422
- [58] Komandin G, Torgashev V, Volkov A, Porodinkov O, Spektor I and Bush A 2010 Optical properties of BiFeO₃ ceramics in the frequency range 0.3–30.0 THz *Physics of the Solid State* **52** 734–43
- [59] Toulouse C, Liu J, Gallais Y, Measson M-A, Sacuto A, Cazayous M, Chaix L, Simonet V, de Brion S and Pinsard-Godart L 2014 Lattice and spin excitations in multiferroic h-YMnO₃ *Physical Review B* **89** 094415
- [60] Ramachandran B and Rao M R 2009 Low temperature magnetocaloric effect in polycrystalline BiFeO₃ ceramics *Applied Physics Letters* **95** 142505
- [61] Ramachandran B, Dixit A, Naik R, Lawes G and Ramachandra Rao M 2011 Dielectric relaxation near 25 K in multiferroic BiFeO₃ ceramics *Journal of Applied Physics* **110** 104105
- [62] Ramachandran B, Dixit A, Naik R, Lawes G and Ramachandra Rao M 2012 Dielectric relaxation and magneto-dielectric effect in polycrystalline Bi_{0.9}Ca_{0.1}FeO_{2.95} *Applied Physics Letters* **100** 252902
- [63] Ramachandran B, Wu K, Kuo Y and Rao M R 2015 Phonon thermal transport and phonon–magnon coupling in polycrystalline BiFeO₃ systems *Journal of Physics D: Applied Physics* **48** 115301
- [64] Balakrishnan R, Dixit A, Naik R and Rao M S R 2018 Enhancement in electrical and magnetodielectric properties of Ca- and Ba-doped BiFeO₃ polycrystalline ceramics *Journal of the American Ceramic Society* **101** 782–8
- [65] Béa H, Bibes M, Petit S, Kreisel J and Barthélémy A 2007 Structural distortion and magnetism of BiFeO₃ epitaxial thin films: a Raman spectroscopy and neutron diffraction study *Philosophical Magazine Letters* **87** 165–74
- [66] Siwach P, Singh H, Singh J and Srivastava O 2007 Anomalous ferromagnetism in spray pyrolysis deposited multiferroic BiFeO₃ films *Applied Physics Letters* **91** 122503
- [67] Mazumder R, Ghosh S, Mondal P, Bhattacharya D, Dasgupta S, Das N, Sen A, Tyagi A, Sivakumar M and Takami T 2006 Particle size dependence of magnetization and phase transition near TN in multiferroic BiFeO₃ *Journal of applied physics* **100** 033908
- [68] Park T-J, Papaefthymiou G C, Viescas A J, Moodenbaugh A R and Wong S S 2007 Size-dependent magnetic properties of single-crystalline multiferroic BiFeO₃ nanoparticles *Nano letters* **7** 766–72
- [69] Xu X, Qian T, Zhang G, Zhang T, Li G, Wang W and Li X 2006 Fabrication and magnetic properties of multiferroic BiFeO₃ nanotube arrays *Chemistry letters* **36** 112–3
- [70] Singh M K, Katiyar R S and Scott J 2008 New magnetic phase transitions in BiFeO₃ *Journal of Physics: Condensed Matter* **20** 252203
- [71] Scott J, Singh M and Katiyar R 2008 Critical phenomena at the 140 and 200 K magnetic phase transitions in BiFeO₃ *Journal of Physics: Condensed Matter* **20** 322203
- [72] Rovillain P, Cazayous M, Gallais Y, Sacuto A, Lobo R, Lebeugle D and Colson D 2009 Polar phonons and spin excitations coupling in multiferroic BiFeO₃ crystals *Physical Review B* **79** 180411
-

-
- [73] Singh M K, Katiyar R S, Prellier W and Scott J 2008 The Almeida–Thouless line in BiFeO_3 : is bismuth ferrite a mean field spin glass? *Journal of Physics: Condensed Matter* **21** 042202
- [74] Iliev M, Abrashev M, Mazumdar D, Shelke V and Gupta A 2010 Polarized Raman spectroscopy of nearly tetragonal BiFeO_3 thin films *Physical Review B* **82** 014107
- [75] Ramirez M, Kumar A, Denev S, Chu Y, Seidel J, Martin L, Yang S-Y, Rai R, Xue X and Ihlefeld J 2009 Spin-charge-lattice coupling through resonant multimagnon excitations in multiferroic BiFeO_3 *Applied Physics Letters* **94** 161905
- [76] Khabiri G, Anokhin A, Razumnaya A, Yuzyuk Y I, Gueye I, Carcan B, Bouyanfif H, Wolfman J, Autret-Lambert C and El Marssi M 2014 Phonon and magnon excitations in Raman spectra of an epitaxial bismuth ferrite film *Physics of the Solid State* **56** 2507-13
- [77] Chen C-S, Tu C-S, Chen P-Y, Schmidt V, Xu Z-R and Ting Y 2016 Spin-lattice coupling phase transition and phonon anomalies in bismuth ferrite BiFeO_3 *Journal of Alloys and Compounds* **687** 442-50
- [78] Kamba S, Nuzhnyy D, Savinov M, Šebek J, Petzelt J, Prokleška J, Haumont R and Kreisel J 2007 Infrared and terahertz studies of polar phonons and magnetodielectric effect in multiferroic BiFeO_3 ceramics *Physical Review B* **75** 024403
- [79] Bujakiewicz-Korońska R, Hetmańczyk Ł, Garbarz-Glos B, Budziak A, Koroński J, Hetmańczyk J, Antonova M, Kalvane A and Nałęcz D 2011 Investigations of low temperature phase transitions in BiFeO_3 ceramic by infrared spectroscopy *Ferroelectrics* **417** 63-9
- [80] Chen P, Xu X, Koenigsmann C, Santulli A C, Wong S S and Musfeldt J L 2010 Size-dependent infrared phonon modes and ferroelectric phase transition in BiFeO_3 nanoparticles *Nano letters* **10** 4526-32
- [81] Skiadopoulou S, Goian V, Kadlec C, Kadlec F, Bai X, Infante I C, Dkhil B, Adamo C, Schlom D and Kamba S 2015 Spin and lattice excitations of a BiFeO_3 thin film and ceramics *Physical Review B* **91** 174108
- [82] Burkert F, Janowski M, Zhang X, Takeuchi I and Kuntscher C A 2017 Chemical pressure effect in Sm and La substituted ferroelectric BiFeO_3 thin films: Insights from infrared spectroscopy *Journal of Applied Physics* **121** 144103
- [83] Lobo R, Moreira R, Lebeugle D and Colson D 2007 Infrared phonon dynamics of a multiferroic BiFeO_3 single crystal *Physical Review B* **76** 172105
- [84] Fischer P, Polomska M, Sosnowska I and Szymanski M 1980 Temperature dependence of the crystal and magnetic structures of BiFeO_3 *Journal of Physics C: Solid State Physics* **13** 1931
- [85] Przeniosło R, Palewicz A, Regulski M, Sosnowska I, Ibberson R and Knight K 2006 Does the modulated magnetic structure of BiFeO_3 change at low temperatures? *Journal of Physics: Condensed Matter* **18** 2069
- [86] Kézsmárki I, Nagel U, Bordács S, Fishman R S, Lee J H, Yi H T, Cheong S-W and Rőöm T 2015 Optical diode effect at spin-wave excitations of the room-temperature multiferroic BiFeO_3 *Physical review letters* **115** 127203
- [87] Singh M K, Dussan S, Prellier W and Katiyar R S 2009 One-magnon light scattering and spin-reorientation transition in epitaxial BiFeO_3 thin films *Journal of Magnetism and Magnetic Materials* **321** 1706-9
- [88] Popov Y F, Zvezdin A, Vorbev G, Murashev V and Racov D 1993 Linear magnetoelectric effect and phase transitions in bismuth ferrite, BiFeO_3 *Jetp Lett* **57** 65-8
-

- [89] Buhot J, Toulouse C, Gallais Y, Sacuto A, De Sousa R, Wang D, Bellaiche L, Bibes M, Barthélemy A and Forget A 2015 Driving spin excitations by hydrostatic pressure in BiFeO₃ *Physical review letters* **115** 267204
- [90] Khomchenko V and Paixão J 2015 Structural defects as a factor controlling the magnetic properties of pure and Ti-doped Bi_{1-x}Ca_xFeO_{3-x/2} multiferroics *Journal of Physics: Condensed Matter* **27** 436002
- [91] Khomchenko V and Paixão J 2016 Ti doping-induced magnetic and morphological transformations in Sr- and Ca-substituted BiFeO₃ *Journal of Physics: Condensed Matter* **28** 166004
- [92] Bai F, Wang J, Wuttig M, Li J, Wang N, Pyatakov A P, Zvezdin A, Cross L and Viehland D 2005 Destruction of spin cycloid in (111) c-oriented BiFeO₃ thin films by epitaxial constraint: enhanced polarization and release of latent magnetization *Applied Physics Letters* **86** 032511
- [93] Mazumder R, Sujatha Devi P, Bhattacharya D, Choudhury P, Sen A and Raja M 2007 Ferromagnetism in nanoscale BiFeO₃ *Applied Physics Letters* **91** 062510
- [94] Goswami S, Bhattacharya D and Choudhury P 2011 Particle size dependence of magnetization and noncentrosymmetry in nanoscale BiFeO₃ *Journal of Applied Physics* **109** 07D737
- [95] Das B, Ramachandran B, Dixit A, Rao M R, Naik R, Sathyanarayana A, Sairam T and Amarendra G 2020 Emergence of two-magnon modes below spin-reorientation transition and phonon-magnon coupling in bulk BiFeO₃: An infrared spectroscopic study *Journal of Alloys and Compounds* 154754
- [96] Reddy B P, Sekhar M C, Prakash B P, Suh Y and Park S-H 2018 Photocatalytic, magnetic, and electrochemical properties of La doped BiFeO₃ nanoparticles *Ceramics International* **44** 19512-21
- [97] Ramachandran B, Dixit A, Naik R, Lawes G and Ramachandra Rao M 2012 Weak ferromagnetic ordering in Ca doped polycrystalline BiFeO₃ *Journal of Applied Physics* **111** 023910
- [98] Ramachandran B, Dixit A, Naik R, Lawes G and Rao M R 2010 Charge transfer and electronic transitions in polycrystalline BiFeO₃ *Physical Review B* **82** 012102
- [99] Perkins W 1986 Fourier transform-infrared spectroscopy: Part I. Instrumentation *Journal of Chemical Education* **63** A5
- [100] Vertex 80v user manual 2013 *Bruker Optik GmbH, Rudolf-Plank-Straße 27 D-76275 Ettlingen 2nd edition*
- [101] Shimizu T, Era T, Taniguchi H, Fu D, Taniyama T and Itoh M 2010 Phonon dynamics in BiFeO₃ studied by Raman scattering *Ferroelectrics* **403** 187-90
- [102] Rout D, Moon K S and Kang S J L 2009 Temperature-dependent Raman scattering studies of polycrystalline BiFeO₃ bulk ceramics *Journal of Raman Spectroscopy: An International Journal for Original Work in all Aspects of Raman Spectroscopy, Including Higher Order Processes, and also Brillouin and Rayleigh Scattering* **40** 618-26
- [103] Singh M K, Prellier W, Jang H M and Katiyar R S 2009 Anomalous magnetic ordering induced spin-phonon coupling in BiFeO₃ thin films *Solid State Communications* **149** 1971-3
- [104] Kumar A, Scott J and Katiyar R 2012 Magnon Raman spectroscopy and in-plane dielectric response in BiFeO₃: relation to the Polomska transition *Physical Review B* **85** 224410
- [105] Jaiswal A, Das R, Maity T, Vivekanand K, Adyanthaya S and Poddar P 2010 Temperature-dependent Raman and dielectric spectroscopy of BiFeO₃

- nanoparticles: signatures of spin-phonon and magnetoelectric coupling *The Journal of Physical Chemistry C* **114** 12432-9
- [106] Kuzmenko A 2005 Kramers–Kronig constrained variational analysis of optical spectra *Review of scientific instruments* **76** 083108
- [107] Nakamura S, Soeya S, Ikeda N and Tanaka M 1993 Spin-glass behavior in amorphous BiFeO₃ *Journal of applied physics* **74** 5652-7
- [108] Singh M K, Prellier W, Singh M, Katiyar R S and Scott J 2008 Spin-glass transition in single-crystal BiFeO₃ *Physical Review B* **77** 144403
- [109] Suresh P and Srinath S 2013 Observation of high coercivity in multiferroic lanthanum doped BiFeO₃ *Journal of Alloys and Compounds* **554** 271-6
- [110] Das S, Choudhary R, Bhattacharya P, Katiyar R, Dutta P, Manivannan A and Seehra M 2007 Structural and multiferroic properties of La-modified BiFeO₃ ceramics *Journal of applied physics* **101** 034104
- [111] Last J T 1957 Infrared-absorption studies on barium titanate and related materials *Physical Review* **105** 1740
- [112] Lunkenheimer P, Rudolf T, Hemberger J, Pimenov A, Tachos S, Lichtenberg F and Loidl A 2003 Dielectric properties and dynamical conductivity of LaTiO₃: From dc to optical frequencies *Physical Review B* **68** 245108
- [113] Thirunavukkuarasu K, Lichtenberg F and Kuntscher C A 2006 Doping dependence of the optical properties of low-dimensional perovskite-related La_{1-y}Ca_yTiO_{3.4±δ} *Journal of Physics: Condensed Matter* **18** 9173
- [114] Palewicz A, Sosnowska I, Przenioslo R and Hewat A 2010 BiFeO₃ crystal structure at low temperatures *Acta Physica Polonica-Series A General Physics* **117** 296
- [115] Redfern S, Wang C, Hong J, Catalan G and Scott J 2008 Elastic and electrical anomalies at low-temperature phase transitions in BiFeO₃ *Journal of Physics: Condensed Matter* **20** 452205
- [116] Tilley D and Scott J 1982 Frequency dependence of magnetoelectric phenomena in BaMnF₄ *Physical Review B* **25** 3251
- [117] Nikitin S E, Wu L, Sefat A S, Shaykhutdinov K A, Lu Z, Meng S, Pomjakushina E V, Conder K, Ehlers G and Lumsden M D 2018 Decoupled spin dynamics in the rare-earth orthoferrite YbFeO₃: Evolution of magnetic excitations through the spin-reorientation transition *Physical Review B* **98** 064424
- [118] Songvilay M, Rodriguez E, Lindsay R, Green M, Walker H, Rodriguez-Rivera J and Stock C 2018 Anharmonic Magnon Excitations in Noncollinear and Charge-Ordered RbFe²⁺Fe³⁺F₆ *Physical review letters* **121** 087201
- [119] Sosnowska I, Neumaier T P and Steichele E 1982 Spiral magnetic ordering in bismuth ferrite *Journal of Physics C: Solid State Physics* **15** 4835
- [120] Ng S, Hassan Z and Hassan H A 2006 Kramers–Kronig analysis of infrared reflectance spectra with a single resonance *Jurnal Teknologi* **44** 67-76
- [121] Skaar J 2006 Fresnel equations and the refractive index of active media *Physical Review E* **73** 026605
- [122] Xu C, Xu B, Dupé B and Bellaiche L 2019 Magnetic interactions in BiFeO₃: A first-principles study *Physical Review B* **99** 104420
- [123] Goswami S and Bhattacharya D 2018 Magnetic transition at ~ 150 K in nanoscale BiFeO₃ *Journal of Alloys and Compounds* **738** 277-82
- [124] Li W, Zhu J, Wu J, Gan J, Hu Z, Zhu M and Chu J 2010 Temperature dependence of electronic transitions and optical properties in multiferroic BiFeO₃ nanocrystalline film determined from transmittance spectra *Applied Physics Letters* **97** 121102

- [125] Rusakov V, Pokatilov V, Sigov A, Matsnev M and Gubaidulina T 2014 ^{57}Fe Mössbauer study of spatial spin-modulated structure in BiFeO_3 *J. Mat. Sci. Eng. B* **4** 302-9
- [126] Yan F, Xing G, Wang R and Li L 2015 Tailoring surface phase transition and magnetic behaviors in BiFeO_3 via doping engineering *Scientific Reports* **5** 9128
- [127] Čebela M, Janković B, Hercigonja R, Lukić M J, Dohčević-Mitrović Z, Milivojević D and Matović B 2016 Comprehensive characterization of BiFeO_3 powder synthesized by the hydrothermal procedure *Processing and Application of Ceramics* **10** 201-8
- [128] Sharma V, Ghosh R K and Kuanr B K 2019 Investigation of room temperature ferromagnetism in transition metal doped BiFeO_3 *Journal of Physics: Condensed Matter* **31** 395802
- [129] Ceresoli D, Gerstmann U, Seitsonen A P and Mauri F 2010 First-principles theory of orbital magnetization *Physical Review B* **81** 060409
- [130] Uniyal P and Yadav K 2012 Enhanced magnetoelectric properties in $\text{Bi}_{0.95}\text{Ho}_{0.05}\text{FeO}_3$ polycrystalline ceramics *Journal of alloys and compounds* **511** 149-53
- [131] Popov Y F, Kadomtseva A, Vorob'Ev G and Zvezdin A 1994 Discovery of the linear magnetoelectric effect in magnetic ferroelectric BiFeO_3 in a strong magnetic field *Ferroelectrics* **162** 135-40
- [132] Tokunaga M, Azuma M and Shimakawa Y 2010 High-field study of strong magnetoelectric coupling in single-domain crystals of BiFeO_3 *Journal of the Physical Society of Japan* **79** 064713
- [133] Agbelele A, Sando D, Toulouse C, Paillard C, Johnson R, Rüffer R, Popkov A, Carrétéro C, Rovillain P and Le Breton J M 2017 Strain and magnetic field induced spin-structure transitions in multiferroic BiFeO_3 *Advanced Materials* **29** 1602327
- [134] Popkov A, Kulagin N, Soloviov S, Sukmanova K, Gareeva Z and Zvezdin A 2015 Cycloid manipulation by electric field in BiFeO_3 films: Coupling between polarization, octahedral rotation, and antiferromagnetic order *Physical Review B* **92** 140414
- [135] Sando D, Agbelele A, Rahmedov D, Liu J, Rovillain P, Toulouse C, Infante I, Pyatakov A, Fusil S and Jacquet E 2013 Crafting the magnonic and spintronic response of BiFeO_3 films by epitaxial strain *Nature materials* **12** 641
- [136] Zhang X, Sui Y, Wang X, Wang Y and Wang Z 2010 Effect of Eu substitution on the crystal structure and multiferroic properties of BiFeO_3 *Journal of alloys and compounds* **507** 157-61
- [137] Masó N and West A R 2012 Electrical Properties of Ca-Doped BiFeO_3 Ceramics: From p-Type Semiconduction to Oxide-Ion Conduction *Chemistry of Materials* **24** 2127-32
- [138] Gebhardt J and Rappe A M 2018 Doping of BiFeO_3 : A comprehensive study on substitutional doping *Physical Review B* **98** 125202
- [139] Weber W H and Merlin R 2013 Raman scattering in materials science *Springer Science & Business Media* **43** 460-1
- [140] García-Zaldívar O, Díaz-Castañón S, Espinoza-Beltran F J, Hernández-Landaverde M A, López G, Faloh-Gandarilla J and Calderón-Piñar F 2015 BiFeO_3 codoping with Ba, La and Ti: Magnetic and structural studies *Journal of Advanced Dielectrics* **05** 1550034
- [141] Haumont R, Bouvier P, Pashkin A, Rabia K, Frank S, Dkhil B, Crichton W, Kuntscher C A and Kreisel J 2009 Effect of high pressure on multiferroic BiFeO_3 *Physical Review B* **79** 184110

-
- [142] Shvartsman V, Kleemann W, Haumont R and Kreisel J 2007 Large bulk polarization and regular domain structure in ceramic BiFeO_3 *Applied physics letters* **90** 172115
- [143] Zeches R, Rossell M, Zhang J, Hatt A, He Q, Yang C-H, Kumar A, Wang C, Melville A and Adamo C 2009 A strain-driven morphotropic phase boundary in BiFeO_3 *science* **326** 977-80
- [144] Hatt A J, Spaldin N A and Ederer C 2010 Strain-induced isosymmetric phase transition in BiFeO_3 *Physical Review B* **81** 054109
- [145] Das B K, Sairam T N, Balakrishnan R and Rao M S R 2020 Single-ion anisotropy driven splitting of spin wave resonances in BiFeO_3 at low temperature *Journal of Physics: Condensed Matter* **32** 405701
- [146] Das B K, Sairam T, Balakrishnan R and Rao M R 2020 Chemical pressure induced near-complete suppression of spin-wave excitations in $\text{Bi}_{0.9}\text{A}_{0.1}\text{FeO}_{2.95}$ (A= Ba, Ca) *Journal of Physics D: Applied Physics*
- [147] Jin Y, Lu X, Zhang J, Kan Y, Bo H, Huang F, Xu T, Du Y, Xiao S and Zhu J 2015 Studying the Polarization Switching in Polycrystalline BiFeO_3 Films by 2D Piezoresponse Force Microscopy *Scientific Reports* **5** 12237
- [148] Baek S and Eom C 2012 Reliable polarization switching of BiFeO_3 *Philosophical Transactions of the Royal Society A: Mathematical, Physical and Engineering Sciences* **370** 4872-89
- [149] Wu S, Zhang J, Liu X, Lv S, Gao R, Cai W, Wang F and Fu C 2019 Micro-area ferroelectric, piezoelectric and conductive properties of single BiFeO_3 nanowire by scanning probe microscopy *Nanomaterials* **9** 190
- [150] Zhao J, Lu H, Sun J and Shen B 2012 Thickness dependence of piezoelectric property of ultrathin BiFeO_3 films *Physica B: Condensed Matter* **407** 2258-61
- [151] Chu Y, Zhao T, Cruz M, Zhan Q, Yang P, Martin L, Huijben M, Yang C-H, Zavaliche F and Zheng H 2007 Ferroelectric size effects in multiferroic BiFeO_3 thin films *Applied Physics Letters* **90** 252906
- [152] Vila-Fungueiriño J M, Gómez A, Antoja-Lleonart J, Gázquez J, Magén C, Noheda B and Carretero-Genevrié A 2018 Direct and converse piezoelectric responses at the nanoscale from epitaxial BiFeO_3 thin films grown by polymer assisted deposition *Nanoscale* **10** 20155-61